

# arxiv一周文献泛读200727-200731

200727

---

## Optical spectroscopic classification of 35 hard X-ray sources from the Swift-BAT 70-month catalogue

<https://arxiv.org/abs/2007.12609>

type:observation-Xray\_source

comment:本文使用一批地面望远镜设备，尝试对Swift/BAT 70个月的目录中的35个未经良好证认的硬X射线源进行候选体证认，并从可见光光谱分析角度进行分类：31个候选体是活动星系核，1个LINER.

### ► abstract

Authors: E. J. Marchesini, N. Masetti, E. Palazzi, et al.

Comments: Last draft version before referee's approval. Closest to the final published article

The nature of a substantial percentage (about one fifth) of hard X-ray sources discovered with the BAT instrument onboard the Neil Gehrels Swift Observatory (hereafter Swift) is unknown because of the lack of an identified longer-wavelength counterpart. Without such follow-up, an X-ray catalogue is of limited astrophysical value: we therefore embarked, since 2009, on a long-term project to uncover the optical properties of sources identified by Swift by using a large suite of ground-based telescopes and instruments.

In this work, we continue our programme of characterization of unidentified or poorly studied hard X-ray sources by presenting the results of an optical spectroscopic campaign aimed at pinpointing and classifying the optical counterparts of 35 hard X-ray sources taken from the 70-month BAT catalogue. This sample was selected out of the available information about the chosen objects: either they are completely unidentified sources, or their association with a longer-wavelength counterpart is still ambiguous.

With the use of optical spectra taken at six different telescopes we were able to identify the main spectral characteristics (continuum type, redshift, and emission or absorption lines) of the observed objects, and determined their nature.

We identify and characterize a total of 41 optical candidate counterparts corresponding to 35 hard X-ray sources given that, because of positional uncertainties, multiple lower energy counterparts can sometimes be associated with higher energy detections. We discuss which ones are the actual (or at least most likely) counterparts based on our observational results.

In particular, 31 sources in our sample are active galactic nuclei: 16 are classified as Type 1 (with broad and narrow emission lines) and 13 are classified as Type 2 (with narrow emission lines only); two more are BL Lac-type objects. We also identify one LINER, one starburst, and 3 elliptical galaxies. The remaining 5 objects are galactic sources: we identify 4 of them as cataclysmic variables, whereas one is a low mass X-ray binary.

- 本文使用一批地面望远镜设备，尝试对Swift/BAT 70个月的目录中的35个未经良好证认的硬X射线源进行候选体证认，并从可见光光谱分析角度进行分类。
- 文章为这35个源找出了41个光学候选体，其中：
  - 31个候选体是活动星系核，其中16个为1型（兼有宽线和窄线），13个为2型（仅有窄线），另外2个为蝎虎座BL型天体（BL Lacertae objects）。
  - 1个LINER（Low ionization Nuclear Emission Region，低电离星系核发射区域），1个星暴星系，3个椭圆星系。
  - 剩下5个是系内目标，其中4个是激变变星（cataclysmic variables，一个白矮星加一个被吸积的伴星组成的双星系统），另1个是低质量X射线双星。

**Table 2** The selected sample of 41 optical candidate counterparts for our sample of 35 Swift70 sources. Unless stated otherwise, the coordinates in columns 2 and 3 are extracted from the 2MASS catalogue. Optical coordinates marked with † are taken from the USNO-A2.0 catalogue and coordinates marked with ‡ are taken from the USNO-B1.0 catalogue. Objects whose redshift was not available in the literature until our measurements are marked with ∗.

Object	RA (Cpt.) (J2000.0)	DEC (Cpt.) (J2000.0)	Tel.+Inst.	UT date [YYYY-MM-DD]	Exp. time N×[s]	λ range [Å]	Res. [Å]
Swift J0042.9+3016 A*	00:43:01.84	30:17:19.6	Cassini-BFOSC	2013-01-07	2×1800	3400-8550	13.5
Swift J0052.3-2730*	00:52:03.83	-27:23:48.9	TNG-DOLoReS	2013-09-19	2×1200	3700-3900	14.5
Swift J0107.7-1137 A*	01:07:37.83 <sup>†</sup>	-11:39:57.1 <sup>†</sup>	TNG-DOLoReS	2012-08-20	2×1800	3700-3900	14.5
Swift J0107.7-1137 B	01:07:39.64	-11:39:11.8	UKST-SuperCOSMOS I	2004-09-12	1200+600	3900-7600	21.5
Swift J0107.7-1137 C*	01:07:13.77	-11:36:02.8	SPM-B&C	2012-12-03	3×1800	3300-7900	11.2
Swift J0136.5+3906	01:36:32.61 <sup>†</sup>	39:05:59.2 <sup>†</sup>	Cassini-BFOSC	2013-01-07	2×1800	3400-8550	12.7
Swift J0138.8+2925	01:39:24.00	29:24:06.8	Cassini-BFOSC	2013-09-23	2×1800	3400-8550	13.5
Swift J0222.3+2509	02:22:35.23	25:08:14.3	Cassini-BFOSC	2013-01-07	2×1200	3400-8550	12.7
Swift J0428.2-6704 A	04:27:49.60 <sup>†</sup>	-67:04:34.9 <sup>†</sup>	NTT-EFOSC	2017-02-17	2×900	4000-8500	18.1
Swift J0449.6-5515*	04:50:01.94	-55:12:40.5	NTT-EFOSC	2017-02-17	3×10	4000-8500	15.5
Swift J0503.7-2819*	05:03:33.07	-28:16:52.6	SPM-B&C	2015-11-09	2×1800	3300-7900	10.1
Swift J0528.1-3933 NE	05:28:03.18	-39:34:25.7	SPM-B&C	2013-12-04	2×1800	3300-7900	11.2
Swift J0528.1-3933 SW	05:28:02.04	-39:34:44.7	SPM-B&C	2013-12-04	1800	3300-7900	11.2
Swift J0535.2+2830*	05:34:57.91	28:28:37.3	TNG-DOLoReS	2014-01-04	2×1200	3700-3900	16.0
Swift J0550.7-3215 B*	05:50:53.62 <sup>‡</sup>	-32:16:19.0 <sup>‡</sup>	NTT-EFOSC	2017-03-23	3×900	4000-8500	22.0
Swift J0609.5-6245 B*	06:08:38.69	-62:47:16.2	NTT-EFOSC	2017-02-17	3×60	4000-8500	23.5
Swift J0659.3+2406*	06:59:10.67	24:01:40.3	TNG-DOLoReS	2014-01-04	2×1200	3700-3900	15.2
Swift J0701.3-3235*	07:04:08.05	26:25:03.6	TNG-DOLoReS	2014-01-04	2×1200	3700-3900	12.5
Swift J0725.8+3000	07:25:37.24	29:57:14.8	Cassini-BFOSC	2013-04-03	2×1800	3400-8550	13.5
Swift J0733.9+5156*	07:33:26.79	51:53:56.0	SPM-B&C	2013-03-20	2×1800	3300-7900	11.5
Swift J0755.4+8402*	07:58:18.59	83:56:37.4	OAGH-B&C	2013-12-07	1200	3300-7900	11.5
Swift J1007.4+6534*	10:07:13.67	65:35:01.1	Cassini-BFOSC	2013-03-19	2×1800	3400-8550	13.5
Swift J1041.4-1740*	10:41:01.20	-17:34:29.6	Cassini-BFOSC	2013-04-03	2×1800	3400-8550	13.5
Swift J1051.2-1704 B	10:51:37.46	-17:07:29.1	SPM-B&C	2013-04-20	2×1800	3300-7900	9.2
Swift J1114.3+2020 SW	11:14:02.48	20:23:14.3	Cassini-BFOSC	2013-03-20	2×1800	3400-8550	13.1
Swift J1114.3+2020 NE	11:14:02.76	20:23:21.4	SPM-B&C	2015-02-26	3×1800	3300-7900	11.5
Swift J1306.4-4025 B	13:07:12.08	-40:24:27.3	SPM-B&C	2013-04-30	2×1800	3300-7900	11.5
Swift J1512.2-1053 B*	15:12:05.06	-10:46:35.6	SPM-B&C	2013-04-20	3×1800	3300-7900	14.2
Swift J1643.2+7036	16:43:20.25	70:37:57.0	Cassini-BFOSC	2014-03-25	1800	3400-8550	13.5
Swift J1731.3+1442	17:31:13.38	14:42:55.8	SPM-B&C	2013-04-22	2×1800	3300-7900	11.5
Swift J1825.7+7215 NE*	18:25:29.78	72:09:04.1	TNG-DOLoReS	2014-05-04	2×1200	3700-3900	14.0
Swift J1825.7+7215 SW*	18:25:28.59	72:08:59.3	TNG-DOLoReS	2014-05-04	2×1200	3700-3900	14.0
Swift J1852.8+3002*	18:52:49.43	30:04:27.9	SPM-B&C	2013-09-08	2×1800	3300-7900	9.6
Swift J1925.0+5041	19:25:02.18	50:43:13.9	SPM-B&C	2013-06-12	2×1800	3300-7900	12.5
Swift J2024.0-0246*	20:24:02.05	-02:45:32.6	SPM-B&C	2014-07-03	2×1800	3300-7900	9.8
Swift J2059.6+4301 A*	20:59:15.71 <sup>†</sup>	43:01:08.5 <sup>†</sup>	SPM-B&C	2014-10-01	3×1800	3300-7900	11.0
Swift J2059.6+4301 B*	21:00:01.00	43:02:10.9	SPM-B&C	2010-07-15	3×1800	3300-7900	13.0
Swift J2237.0+2543	22:36:32.87	25:45:47.4	Cassini-BFOSC	2009-11-17	1800	3400-8550	13.5
Swift J2242.4-3711	22:42:33.38	-37:11:07.4	SPM-B&C	2013-12-05	2×1200	3300-7900	11.5
Swift J2352.6-1707*	23:52:51.42	-17:04:37.2	SPM-B&C	2013-09-06	2×1200	3300-7900	11.0
2PBC J0819.2-2508*	08:19:16.21	-25:07:06.21	NTT-EFOSC	2017-03-23	4×900	3800-9200	22.0

# The Fate of the Merger Remnant in GW170817 and its Imprint on the Jet Structure

<https://arxiv.org/abs/2007.12245>

type:theory-GRB\_jet

comment:发现喷流的能量角分布主要决定于喷流的存在时间与并合残骸塌缩时间的比值。

## ► abstract

Authos: Ariadna Murgia-Berthier, Enrico Ramirez-Ruiz, Fabio De Colle, Agnieszka Janiuk, Stephan Rosswog, William H. Lee

Comments: 5 figures, 7 pages, submitted to ApJL

The first neutron star binary merger detected in gravitational waves, GW170817 and the subsequent detection of its emission across the electromagnetic spectrum showed that these systems are viable progenitors of short  $\gamma$ -ray bursts (sGRB). The afterglow signal of GW170817 has been found to be consistent with a structured GRB jet seen off-axis, requiring significant amounts of relativistic material at large angles. This trait can be attributed to the interaction of the relativistic jet with the external wind medium.

Here we perform numerical simulations of relativistic jets interacting with realistic wind environments in order to explore how the properties of the wind and central engine affect the structure of successful jets. We find that the angular energy distribution of the jet depends primarily on the ratio between the lifetime of the jet and the time it takes the merger remnant to collapse. We make use of these simulations to constrain the time it took for the merger remnant in GW170817 to collapse into a black hole based on the angular structure of the jet as inferred from afterglow observations. We conclude that the lifetime of the merger remnant in GW170817 was  $\approx 0.8\text{--}0.9\text{s}$ , which, after collapse, triggered the formation of the jet.

- GW170817成协的短暴的余辉反映了其喷流具有结构性，这可能是相对论喷流与外部星风介质相互作用的结果。
- 本文对这种相互作用进行了数值模拟，探究星风的性质和中心引擎对成功喷流的结构会产生怎样的影响。结果发现喷流的能量角分布主要决定于喷流的存在时间与并合残骸塌缩时间的比值。

- 利用以上结果，根据观测得到的喷流能量角分布，即可得出GW170817中的并合残骸的存活时间（塌缩至黑洞所经历的时间）为0.8–0.9秒。

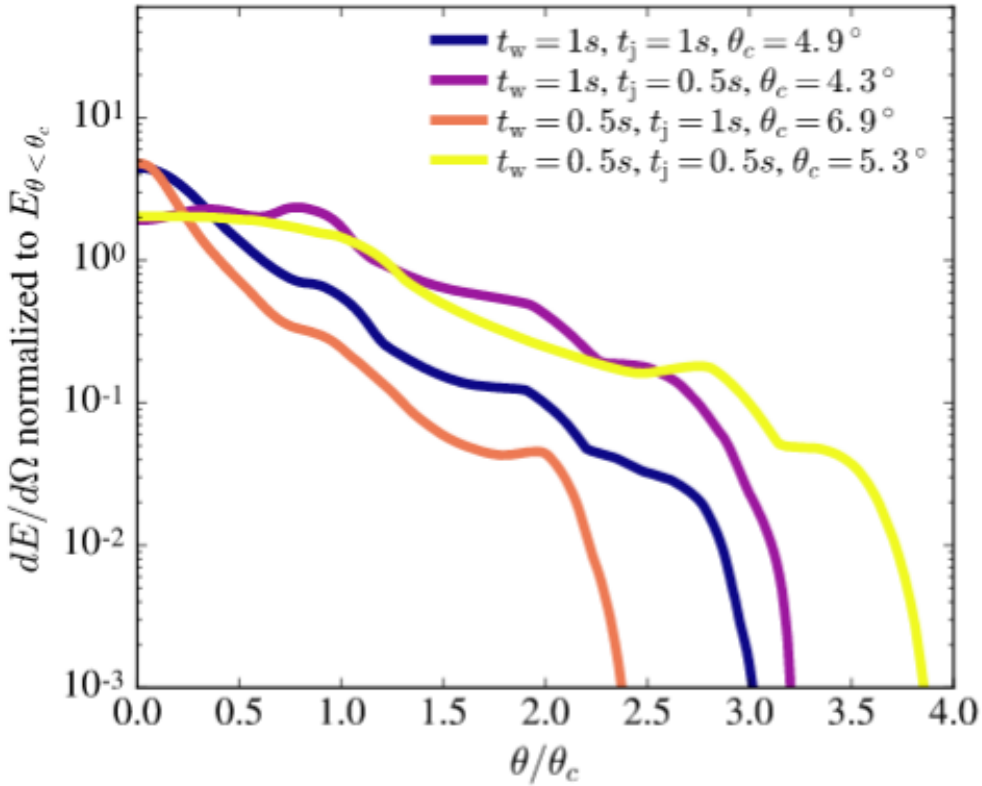


**Figure 1.** *Top Panels:* Density (*Left*) and Lorentz factor (*Right*) profiles of simulations of the interaction of a relativistic jet with a spherical wind. The bar corresponds to  $1.5 \times 10^{10}$  cm. Calculations were done in 2D spherical coordinates using an adaptive grid of size  $l_r = 6 \times 10^{10}$  cm,  $l_\theta = \pi/2$  with  $100 \times 40$  initial cells and five levels of refinement resulting in a maximum resolution of  $3.75 \times 10^7$  cm. The luminosity is  $L_j = 1 \times 10^{50}$  erg/s, the initial Lorentz factor  $\Gamma = 10$ , and the initial half-opening angle  $\theta_0 = 10^\circ$ . The wind has an  $\dot{M} = 10^{-3} M_\odot/\text{s}$  and  $v_w = 0.3c$ . Different simulations assume different collapse times and jet lifetimes. The simulations were run up to 4s. The *Top* and *Middle* snapshots were taken after 2.75s while the *Bottom* one was taken after 3.25s. *Bottom Panel:* Energy per unit angle of the resulting jet. The time is the same as the above panel. The energy is normalized to the total energy in the core of the jet.

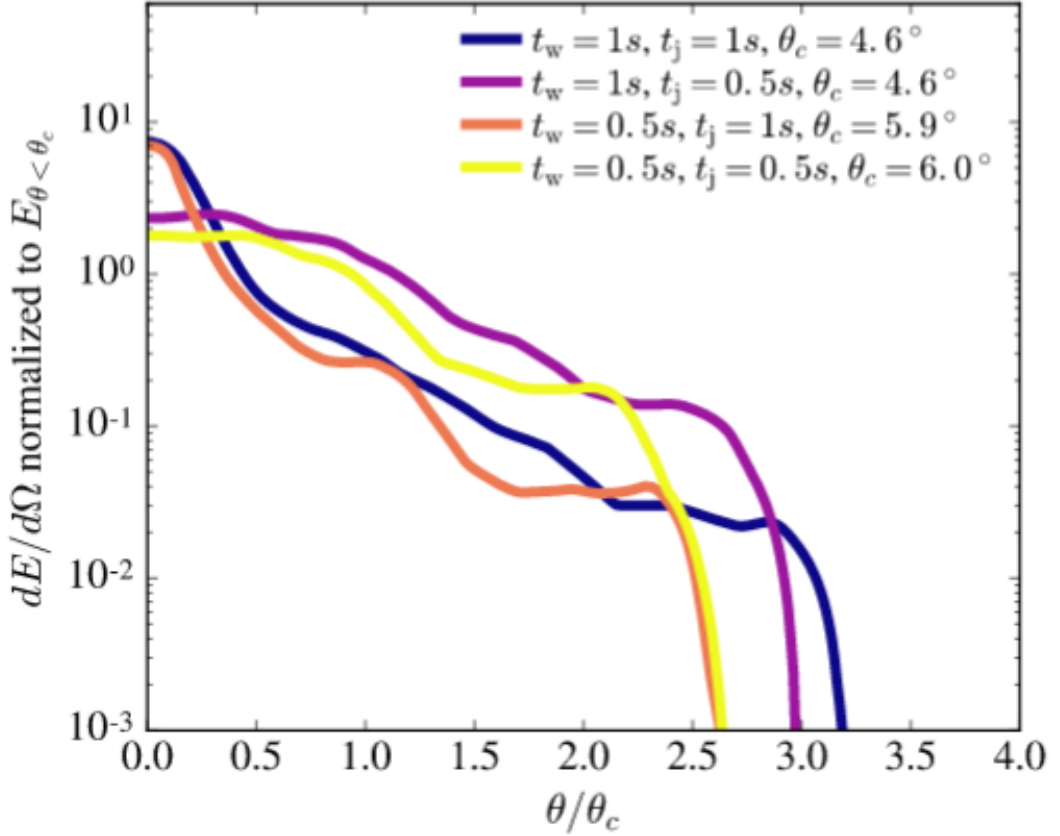


**Figure 2.** *Top Panel:* Density (*Left*) and Lorentz factor (*Right*) profiles of simulations of the interaction of the relativistic jet with a neutrino-driven wind. Shown is a  $1.5 \times 10^{10}$  cm scale bar. The resolution, as well as the properties of the jet are the same as in Fig 1. The *Top* and *Middle* Panels show snapshots after 2.5s while 3s for the *Bottom* Panel. The wind has a mass loss rate of  $\dot{M} = 10^{-3} M_{\odot}/s$  in the polar region and a velocity of  $v_w = 0.3c$ . *Bottom Panel:* Energy per unit angle of the jet after its propagation. The time is the same as the above panel. The energy is normalized to the energy in the core.

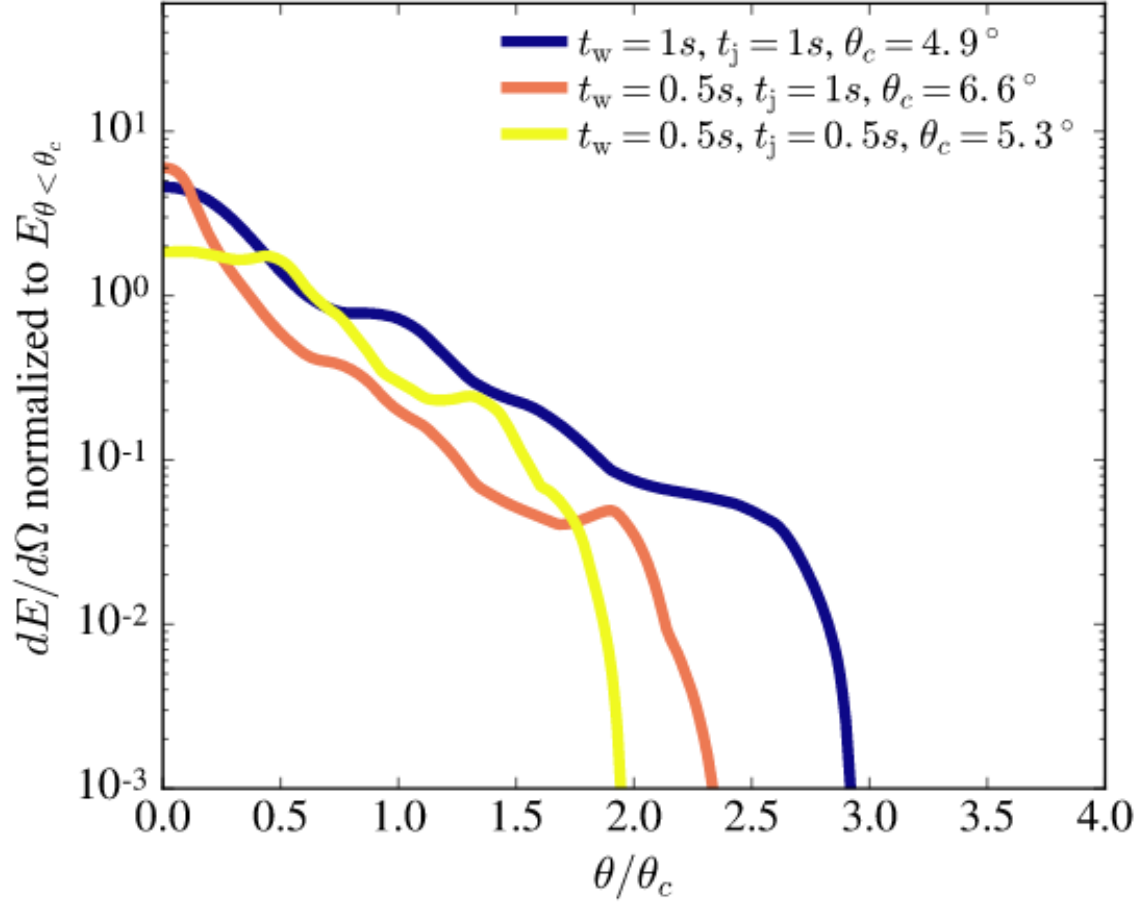


**Figure 3.** *Top Panel:* Density (*Left*) and Lorentz factor (*Right*) profiles of simulations of the interaction of a relativistic jet with a magnetized wind based on Janiuk (2019). Shown is a  $1.5 \times 10^{10}$  cm scale bar. The resolution, as well as the properties of the jet are the same as in Fig 1. The wind has a mass loss rate of  $\dot{M} = 10^{-3} M_{\odot}/\text{s}$  in the polar region and  $v_w = 0.3c$ . The *Top* and *Middle* Panels correspond to a simulation time of 2.5s. The simulation corresponding to  $t_w = 1\text{s}$ ,  $t_j = 0.5\text{s}$  is not shown as the wind in that case is dense enough to choke the jet, rendering the sGRB unsuccessful. *Bottom Panel* Energy per unit angle of the jet resulting from the simulations. The time is the same as the above panel. The energy is normalized to the energy in the core.

# An Energy Inventory of Tidal Disruption Events

<https://arxiv.org/abs/2007.12198>

type:statistic-TDE

comment:本文使用MOSFiT来计算TDE事件的总能量 (integrated energy) , 辐射时标和平均辐射效率。

## ► abstract

Authors: Brenna Mockler, Enrico Ramirez-Ruiz

Comments: submitted to ApJL. 13 pages, 4 figures, 1 table

Tidal disruption events (TDEs) offer a unique opportunity to study a single super-massive black hole (SMBH) under feeding conditions that change over timescales of days or months. However, the primary mechanism for generating luminosity during the flares remains debated. Despite the increasing number of observed TDEs, it is unclear whether most of the energy in the initial flare comes from accretion near the gravitational radius or from circularizing debris at larger distances from the SMBH. The energy dissipation efficiency increases with decreasing radii, therefore by measuring the total energy emitted and estimating the efficiency we can derive clues about the nature of the emission mechanism. **Here we calculate the integrated energy, emission timescales, and average efficiencies for the TDEs using the Modular Open Source Fitter for Transients (MOSFiT).** Our calculations of the total energy generally yield higher values than previous estimates. This is predominantly because, if the luminosity follows the mass fallback rate, TDEs release a significant fraction of their energy long after their light curve peaks. We use MOSFiT to calculate the conversion efficiency from mass to radiated energy, and find that for many of the events it is similar to efficiencies inferred for active galactic nuclei. There are, however, large systematic uncertainties in the measured efficiency due to model degeneracies between the efficiency and the mass of the disrupted star, and these must be reduced before we can definitively resolve the emission mechanism of individual TDEs.

- 目前我们还不清楚TDE的耀发中的主要辐射机制，不清楚在最初耀发中的能量的主要来源（来自引力半径附近的吸积区域或远一些的环绕碎片circularizing debris）。在

TDE吸积区域中，半径越小，能量耗散效率（energy dissipation efficiency）越高，所以测量TDE辐射的总能量并估算其（辐射）效率可以给我们提供有关辐射机制的线索。

- 本文使用MOSFiT来计算TDE事件的总能量（integrated energy），辐射时标和平均辐射效率。
- 本文计算给出的能量要普遍高于以往的估计，主要原因在于，如果TDE光度是随质量回落率（mass fallback rate）变化，则在光变曲线的峰值过后，TDE仍会继续辐射大量能量。
- 计算给出的多数TDE事件的能量转换效率与活动星系核的效率类似。不过文章指出效率的测量存在较大的系统误差（由于模型存在辐射效率和被瓦解的星体质量间的简并），有必要减少这样的简并才能够更准确地解决单个事件的能量机制问题。

TDE	E <sub>bol, lit</sub>	E <sub>bol</sub>	E <sub>bol</sub>	$\frac{E_{bol} (obs.)}{E_{bol} (full)}$	$\frac{L_p \times t_{p,ff}}{E_{bol} (full)}$	t <sub>p,ff</sub>	$\frac{t_{50}}{t_{p,ff}}$	$\frac{t_{90}}{t_{p,ff}}$	avg. $\epsilon$	$\epsilon$ at L <sub>p</sub>	$\frac{L_p}{L_{Edd}}$	$\Delta M_{min}$
	(obs. times) (full curve)				(days)				(log <sub>10</sub> )	(log <sub>10</sub> )	(log <sub>10</sub> M <sub>⊙</sub> )	
	(log <sub>10</sub> ergs)	(log <sub>10</sub> ergs)	(log <sub>10</sub> ergs)						(0.09 dex)	(0.11 dex)	(15 days)	(0.24 dex)
<b>10jh</b>	$\geq 51.3$	$51.4^{+0.1}_{-0.1}$	$51.6^{+0.1}_{-0.1}$	$0.68^{+0.02}_{-0.03}$	$0.32^{+0.01}_{-0.02}$	$55^{+1}_{-1}$	$3.3^{+0.4}_{-0.2}$	$37.4^{+27.9}_{-7.3}$	$-3.3^{+0.1}_{-0.0}$	$-3.3^{+0.1}_{-0.0}$	$0.15^{+0.02}_{-0.02}$	$-2.7^{+0.1}_{-0.1}$
D1-9	$\geq 50.9$	$52.3^{+0.2}_{-0.4}$	$53.0^{+0.2}_{-0.4}$	$0.21^{+0.03}_{-0.03}$	$0.36^{+0.08}_{-0.06}$	$127^{+17}_{-12}$	$2.6^{+0.5}_{-0.3}$	$8.5^{+6.1}_{-1.8}$	$-1.8^{+0.5}_{-0.6}$	$-1.9^{+0.4}_{-0.5}$	$0.33^{+0.22}_{-0.23}$	$-1.3^{+0.2}_{-0.4}$
D3-13	$\geq 52.3$	$52.3^{+0.1}_{-0.2}$	$52.9^{+0.2}_{-0.2}$	$0.20^{+0.01}_{-0.02}$	$0.43^{+0.04}_{-0.06}$	$123^{+6}_{-7}$	$2.4^{+0.2}_{-0.1}$	$6.6^{+1.9}_{-0.9}$	$-1.7^{+0.2}_{-0.3}$	$-1.8^{+0.2}_{-0.2}$	$0.31^{+0.16}_{-0.12}$	$-1.3^{+0.2}_{-0.2}$
<b>14ae</b>	$\approx 50.2$	$50.2^{+0.0}_{-0.0}$	$50.5^{+0.0}_{-0.0}$	$0.51^{+0.03}_{-0.03}$	$0.40^{+0.03}_{-0.03}$	$18^{+2}_{-1}$	$2.6^{+0.2}_{-0.1}$	$6.0^{+0.4}_{-0.5}$	$-3.3^{+0.2}_{-0.2}$	$-3.4^{+0.2}_{-0.1}$	$0.48^{+0.07}_{-0.09}$	$-3.7^{+0.0}_{-0.0}$
14li <sup>a</sup>	$\approx 50.8$	$51.1^{+0.2}_{-0.2}$	$51.6^{+0.3}_{-0.3}$	$0.35^{+0.07}_{-0.05}$	$0.24^{+0.07}_{-0.06}$	$40^{+9}_{-8}$	$4.4^{+2.0}_{-1.3}$	$23.6^{+27.2}_{-11.8}$	$-1.7^{+0.6}_{-0.8}$	$-1.9^{+0.6}_{-0.7}$	$0.46^{+0.12}_{-0.15}$	$-2.7^{+0.3}_{-0.3}$
<b>16fnl</b>	$49.3^{+0.1}_{-0.1}$	$50.1^{+0.0}_{-0.0}$	$50.4^{+0.1}_{-0.1}$	$0.51^{+0.03}_{-0.04}$	$0.35^{+0.02}_{-0.04}$	$20^{+1}_{-1}$	$2.7^{+0.3}_{-0.1}$	$12.9^{+5.0}_{-2.9}$	$-3.3^{+0.1}_{-0.0}$	$-3.4^{+0.1}_{-0.0}$	$0.30^{+0.04}_{-0.04}$	$-3.8^{+0.1}_{-0.1}$
		$(49.5^{+0.0}_{-0.0})^b$	$(49.7^{+0.0}_{-0.0})^b$									
<b>15oi</b>	$\approx 50.8$	$50.4^{+0.2}_{-0.2}$	$50.9^{+0.2}_{-0.3}$	$0.37^{+0.09}_{-0.05}$	$0.29^{+0.09}_{-0.06}$	$31^{+5}_{-4}$	$3.8^{+1.9}_{-1.2}$	$34.4^{+23.2}_{-22.5}$	$-3.0^{+0.8}_{-0.3}$	$-3.0^{+0.8}_{-0.3}$	$0.19^{+0.07}_{-0.06}$	$-3.4^{+0.2}_{-0.3}$
16axa	$\approx 50.7$	$50.3^{+0.2}_{-0.1}$	$50.4^{+0.2}_{-0.1}$	$0.78^{+0.05}_{-0.06}$	$0.27^{+0.04}_{-0.03}$	$29^{+6}_{-4}$	$3.9^{+1.1}_{-0.7}$	$31.1^{+18.6}_{-7.0}$	$-2.8^{+0.3}_{-0.4}$	$-2.8^{+0.3}_{-0.4}$	$0.10^{+0.05}_{-0.03}$	$-3.9^{+0.2}_{-0.1}$
<b>11af</b>	$50.6^{+0.0}_{-0.0}$	$50.7^{+0.0}_{-0.0}$	$50.9^{+0.1}_{-0.1}$	$0.62^{+0.05}_{-0.15}$	$0.35^{+0.04}_{-0.12}$	$29^{+2}_{-2}$	$2.8^{+2.3}_{-0.3}$	$14.1^{+25.7}_{-4.5}$	$-2.9^{+1.0}_{-0.4}$	$-3.0^{+1.0}_{-0.4}$	$0.26^{+0.05}_{-0.05}$	$-3.4^{+0.1}_{-0.1}$
09ge	$52.0^{+0.1}_{-0.6}$	$50.5^{+0.0}_{-0.0}$	$50.6^{+0.0}_{-0.0}$	$0.64^{+0.02}_{-0.02}$	$0.27^{+0.02}_{-0.01}$	$36^{+1}_{-1}$	$3.9^{+0.3}_{-0.4}$	$30.8^{+2.3}_{-3.2}$	$-2.6^{+0.2}_{-0.3}$	$-2.6^{+0.2}_{-0.3}$	$0.09^{+0.02}_{-0.01}$	$-3.6^{+0.0}_{-0.0}$
09djl	—	$51.0^{+0.3}_{-0.2}$	$51.2^{+0.4}_{-0.3}$	$0.58^{+0.13}_{-0.12}$	$0.21^{+0.07}_{-0.06}$	$26^{+4}_{-3}$	$5.1^{+2.3}_{-1.2}$	$23.5^{+38.3}_{-11.2}$	$-1.6^{+0.4}_{-0.4}$	$-1.7^{+0.4}_{-0.4}$	$0.43^{+0.21}_{-0.18}$	$-3.1^{+0.4}_{-0.3}$
TDE2	—	$51.5^{+0.1}_{-0.1}$	$52.1^{+0.1}_{-0.1}$	$0.25^{+0.03}_{-0.03}$	$0.09^{+0.08}_{-0.05}$	$40^{+36}_{-13}$	$11.0^{+12.1}_{-5.2}$	$93.1^{+107.6}_{-43.1}$	$-1.1^{+0.4}_{-0.5}$	$-1.7^{+0.7}_{-0.5}$	$0.86^{+0.09}_{-0.33}$	$-2.1^{+0.1}_{-0.1}$
TDE1	—	$51.0^{+0.2}_{-0.2}$	$51.3^{+0.3}_{-0.2}$	$0.45^{+0.10}_{-0.11}$	$0.24^{+0.05}_{-0.04}$	$52^{+23}_{-17}$	$4.6^{+1.4}_{-1.2}$	$38.5^{+22.2}_{-15.1}$	$-1.9^{+0.7}_{-0.5}$	$-1.9^{+0.6}_{-0.5}$	$0.19^{+0.22}_{-0.11}$	$-2.9^{+0.3}_{-0.2}$
16aaa	$\approx 52.7$	$51.2^{+0.6}_{-0.4}$	$51.3^{+0.6}_{-0.4}$	$0.88^{+0.06}_{-0.09}$	$0.23^{+0.09}_{-0.09}$	$33^{+10}_{-5}$	$4.6^{+2.9}_{-1.7}$	$21.4^{+40.5}_{-11.0}$	$-1.6^{+0.7}_{-0.6}$	$-1.7^{+0.5}_{-0.6}$	$0.37^{+0.30}_{-0.26}$	$-3.0^{+0.6}_{-0.4}$

**Table 1.** The transients in the table are organized as follows: The first 9 events have UV detections during the same time period as the optical detections. The events in bold have observations at or before the light curve peak. Systematic errors for parameters are listed at the top of their respective columns, throughout the text we include the systematic errors in the errors quoted for the parameters. Systematic errors for  $t_{\text{peak}}$  and efficiency ( $\epsilon$ ) are taken from Mockler et al. (2019), additional errors were calculated using the method described in the same paper and are based on the uncertainty in the stellar mass-radius relation. **Column descriptions:** (1) transient names; (2) Bolometric energy estimates from the literature. The methods used to calculate these estimates are described below in this caption; (3) Bolometric energy estimates from the MOSFiT fits, integrated over the same time period used for the literature energy estimates in column 2. The literature energy estimate for PTF09ge is from late-time dust emission and therefore the MOSFiT energy estimate for column 3 for this event was integrated over the time period of the initial optical observations presented in Arcavi et al. (2014); (4) Column 2 divided by column 3; (5) The peak bolometric luminosity multiplied by the timescale from first fallback to peak luminosity, divided by column 3; (6) The  $\Delta t$  between when the first stellar debris falls back to pericenter ('first fallback') and the time of peak luminosity. This is necessarily less than the time from disruption to peak; (7) & (8)  $t_{50}$  and  $t_{90}$  are the respective times when 5% and 90% of the total energy is radiated. The first 5% and last 5% are excluded from the integral. In columns 7 & 8 they are scaled by the peak timescale calculated from first fallback; (9) The average observed efficiency, defined as  $E_{\text{bol}}/\Delta M c^2$ , where  $\Delta M$  is the total amount of mass that is bound to the black hole; (10) The peak observed efficiency, defined as  $L_{\text{peak}}/\dot{M}_{\text{peak}}c^2$ ; (11) Eddington ratio at peak luminosity; (12) The minimum amount of mass required to generate the integrated energy if the conversion from mass to energy were 100% efficient ( $E_{\text{bol}} = \Delta M_{\min} c^2$ ). **Notes on literature energy estimates:** The value for PS1-10jh was calculated by integrating the light-curve model using a lower limit for the temperature and luminosity (Gzary et al. 2012). The values for both D1-9 and D3-13 were calculated by integrating a  $t^{-5/3}$  power law starting at  $t_{\text{discovery}}$  (after  $t_{\text{peak}}$ ) using the lower limits to the blackbody temperature and luminosity (Gzary et al. 2008). The value for PTF09ge was calculated from IR dust emission, motivating that there is additional radiated energy not observed in the initial optical and UV light curve (van Velzen et al. 2016). The values for ASASSN-14ae, ASASSN-14li, ASASSN-15oi, iPTF16fnl, iPTF16axa, and OGLE16aaa were calculated by integrating the blackbody fits to the observed optical and UV light curves (Holoien et al. 2014, 2016b,a; Blagorodnova et al. 2017; Hung et al. 2017; Wyrzykowski et al. 2017). According to Holoien et al. (2016b), the blackbody fit for ASASSN-14li was 'dominated by systematic errors'. For PS1-11af, Chornock et al. (2014) calculated the radiated energy by using a constant bolometric correction to the light curve from a blackbody fit 10 rest-frame days after peak.

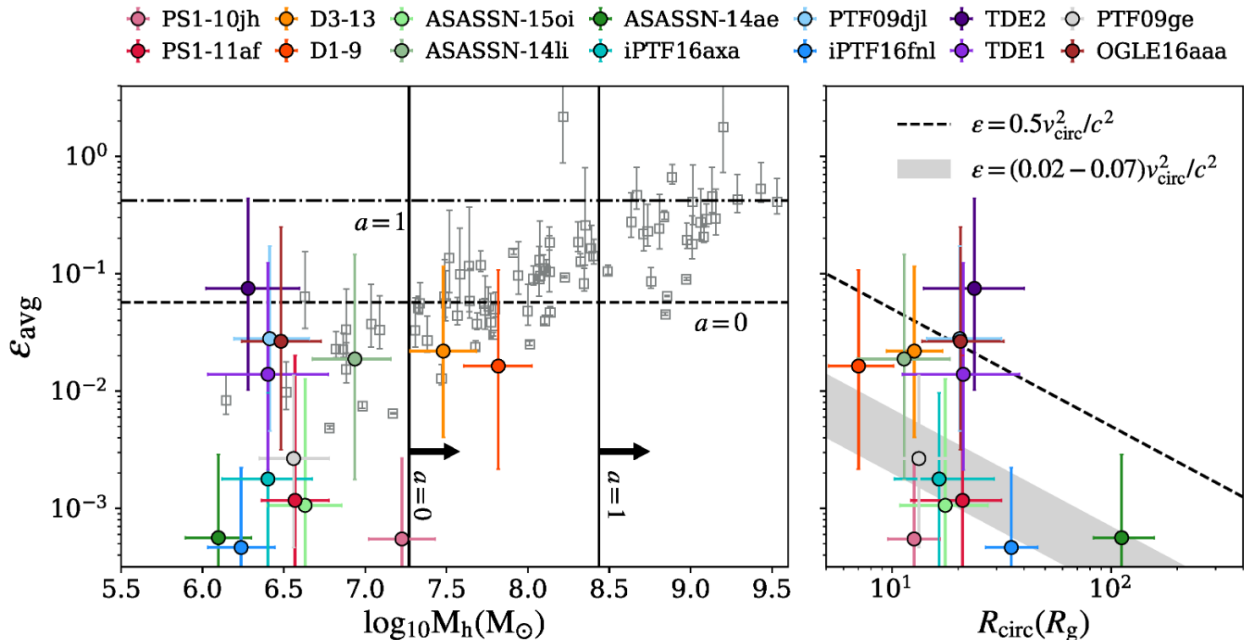


**Figure 4.** *Left Panel:* We compare the average efficiencies (integrated over the full light curve) of our sample of TDEs with AGN efficiencies from Davis & Laor (2011) as a function of black hole mass. Our data is plotted as colored circles, while the AGN data from Davis & Laor (2011) is plotted as gray squares. The trend of increasing efficiency with increasing black hole mass in the AGN data has been argued to be due at least in part to selection effects (Raimundo et al. 2012; Laor & Davis 2011). We plot two vertical lines denoting where  $R_t < R_{\text{isco}}$  for a  $1M_\odot$  ZAMS star disrupted by black holes with spins of  $a = 0$  and  $a = 1$  respectively ( $R_{\text{isco}} = 3R_s$  if  $a = 0$ ,  $R_{\text{isco}} = 0.5R_s$  if  $a = 1$ ). *Right Panel:* We plot the average efficiencies of our sample versus the circularization radius in units of gravitational radii, with a dashed line denoting the maximum efficiency of conversion between kinetic energy (KE) and radiated energy at a given radius (assuming the gas is virialized post-collision). While the dashed line is the maximum theoretical efficiency of stream collisions at a given radius, simulations by Jiang et al. (2016) found the stream collision efficiency to be much lower – the radiated energy was  $\approx 2 - 7\%$  of the total KE. If these collisions occur at the circularization radius, we might expect the efficiencies to fall within the gray shaded region in the plot. However, the collision radius of the most bound debris will be much larger than the circularization radius unless the disruption is very deep and the black hole is very large, therefore the efficiency of the stream collisions will likely be much lower ( $R_{\text{coll}} \approx 6 \times R_{\text{circ}}$  for the most bound debris in a full disruption of a solar mass star by a  $5 \times 10^6 M_\odot$  Schwarzschild black hole) (Jiang et al. 2016; Dai et al. 2015; Guillochon & Ramirez-Ruiz 2015).

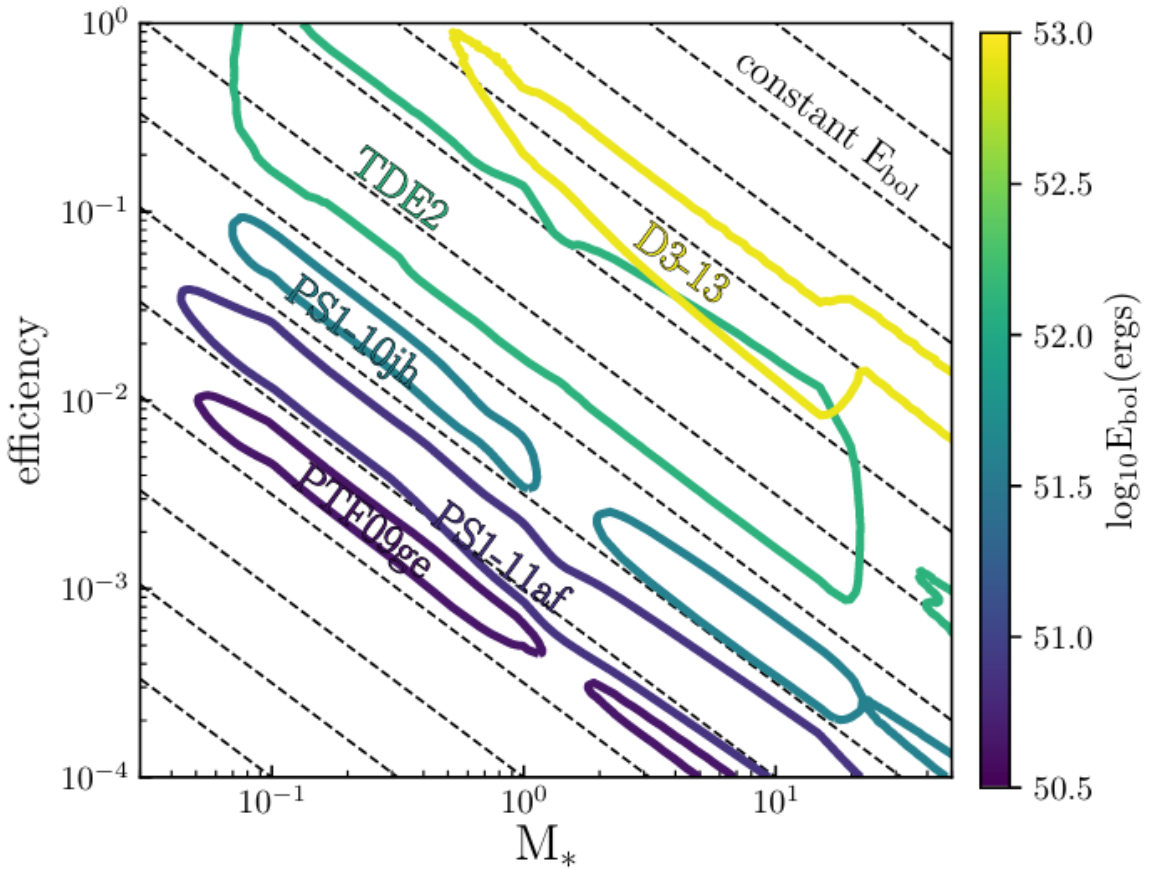


**Figure 1.** The role of stellar mass in TDEs. *Bottom Panel:* The likelihood contours for stellar mass and efficiency parameters derived for five TDEs with a spread of bolometric energy values. The contours have been calculated by taking the parameter values from the converged walker distributions from the MOSFiT fits, varying the efficiency parameter between  $0.0001 - 1$  and the stellar mass between  $0.01 - 100$ , and recalculating the likelihood of each parameter combination. We kept the values from the converged walker distributions constant for all parameters except for  $M_*$  and efficiency. The

200728

# A targeted search for repeating fast radio bursts associated with gamma-ray bursts

<https://arxiv.org/abs/2007.13246>

type:observation-FRB&GRB

comment:尝试使用Arecibo Observatory (A0,300m)和Green Bank Telescope (GBT,100m)在11个疑似产生了磁星的过往GRB的发生地, 以及GW170817的区域进行潜在射电爆的搜寻

## ► abstract

Authors: Nipuni T. Palliyaguru, Devansh Agarwal, Golnoosh Golpayegani et al.

Comments: 7 pages, 4 figures, submitted to MNRAS

The origin of fast radio bursts (FRBs) still remains a mystery, even with the increased number of discoveries in the last three years. Growing evidence suggests that some FRBs may originate from magnetars. Large, single-dish telescopes such as Arecibo Observatory (A0) and Green Bank Telescope (GBT) have the sensitivity to detect FRB~121102-like bursts at gigaparsec distances. Here we present searches using A0 and GBT that aimed to find potential radio bursts at 11 sites of past  $\gamma$ -ray bursts that show evidence for the birth of a magnetar. We also performed a search towards GW170817, which has a merger remnant whose nature remains uncertain. We place  $10\sigma$  fluence upper limits of  $\approx 0.036$  Jy ms at 1.4 GHz and  $\approx 0.063$  Jy ms at 4.5 GHz for A0 data and fluence upper limits of  $\approx 0.085$  Jy ms at 1.4 GHz and  $\approx 0.098$  Jy ms at 1.9 GHz for GBT data, for a maximum pulse width of  $\approx 42$  ms. The A0 observations had sufficient sensitivity to detect any FRB of similar luminosity to the one recently detected from the Galactic magnetar SGR 1935+2154. Assuming a Schechter function for the luminosity function of FRBs, we find that our non-detections favor a steep power-law index ( $\alpha \lesssim -1.0$ ) and a large cut-off luminosity ( $L_0 \gtrsim 10^{42} \text{ erg/s}$ ).

- 作者尝试使用两个大的单盘 (single-dish) 射电望远镜Arecibo Observatory (A0,300m)和Green Bank Telescope (GBT,100m)在11个疑似产生了磁星的过往GRB的发生地, 以及GW170817的区域进行潜在射电爆的搜寻（如何搜寻？？）。这两个望远镜足可在Gpc的距离探测到类FRB121102的爆。

**Table 1.** The list of targets. Name, redshift, distance, RA, DEC, galactic coordinates, expected DM, GRB duration ( $T_{90}$ ), and the minimum detectable luminosity ( $L_{\min}$ ) corresponding to S/N= 10 at 1.4 GHz.

Name	Redshift	Distance Mpc	RA (deg)	DEC (deg)	gl (deg)	gb (deg)	Expected DM ( $\text{cm}^{-3}$ pc)	Duration (sec)	$L_{\min}$ erg/s
GRB 030329/SN2003dh	0.169	812	10:44:50.03	21:31:18.15	216.98	60.69	264.32	25	$4.0 \times 10^{40}$
GRB 060218/SN2006aj	0.033	145	03:21:39.69	16:52:01.6	166.92	-32.88	173.08	2100	$1.28 \times 10^{39}$
GRB 120422A/SN2012bz	0.280	1434	09:07:38.42	14:01:06.0	215.22	36.437	413.64	5.35	$1.25 \times 10^{41}$
GRB 130427A/SN2013cq	0.340	1795	11:32:32.63	27:41:51.7	206.51	72.50	472.37	162.83	$1.97 \times 10^{41}$
GRB 130702A/SN2013dx	0.145	687	14:29:14.78	15:46:26.1	11.35	64.63	241.17	59	$2.88 \times 10^{40}$
GRB 130215A/SN2013ez	0.597	3508	02:53:56.6	13:23:13.2	163.07	-39.76	991.80	65.7	$7.52 \times 10^{41}$
GRB 130603B	0.356	1894	11:28:48.15	17:04:16.9	236.42	68.42	498.47	0.18	$2.19 \times 10^{41}$
GRB 140903A	0.351	1863	15:52:03.27	27:36:09.4	44.39	50.12	496.38	0.30	$2.12 \times 10^{41}$
GRB 051221	0.547	2868	21:54:48.71	16:53:28.2	73.54	-28.58	786.02	1.4	$5.03 \times 10^{41}$
GRB 100816A	0.803	4529	23:26:57.62	26:34:43.9	100.44	32.57	1396.40	2.9	$1.25 \times 10^{42}$
GRB 130831A	0.479	2459	23:54:29.91	29:25:47.6	08.33	-31.82	663.84	32.5	$3.69 \times 10^{41}$
GW170817	0.0098	42	13:09:48.089	-23:22:53.35	308.37	39.29 7	77.27	2.0	$2.49 \times 10^{38}$

**Table 2.** Summary of observational setup. Telescope name, center frequency ( $f_c$ ), System temperature ( $T_{\text{sys}}$ ), Telescope gain, Bandwidth, number of channels ( $N_{\text{chan}}$ ), sampling time ( $t_{\text{samp}}$ ) and the FoV.

Name Telescope	$f_c$ (MHz)	$T_{\text{sys}}$ K	Gain (K/Jy)	BW (MHz)	$N_{\text{chan}}$	$t_{\text{samp}}$ $\mu\text{s}$	FoV $\text{deg}^2$
AO	1.4	$\approx 30$	8	600	512	40.96	$9.5 \times 10^{-3}$
AO	5.0	$\approx 30$	4	800	512	40.96	$7.8 \times 10^{-4}$
GBT	1.4	$\approx 20$	2.0	800	512	10.24	$1.8 \times 10^{-2}$
GBT	1.9	$\approx 22$	1.9	800	512	10.24	$8.7 \times 10^{-3}$

$T_{\text{sys}}$ , Gain and FoV values for AO and GBT are obtained from <http://www.naic.edu/~astro/RXstatus/rvratabz.shtml> and <https://science.nrao.edu/facilities/gbt/proposing/GBTpg.pdf> respectively.

- 观测

- AO的观测在2017 December 12:50 UTC 和 2018 December 19:55 UTC之间进行, 每次(epoch) 对一个目标观测0.6个小时, 所有11个目标一共耗时114个小时, 每个目标在每个频率上耗时1小时到21小时不等。观测数据由PUPPI (AO的一个后端, backend) 记录, 中心频率分别为1380MHz和4.5GHz, 频宽约为600MHz。
- GBT的观测在2017 November 02:41 UTC 和 2018, July 31:02 UTC之间的10个时间段(epoch) 上进行。每次在每个频率上对GW 170817观测1个小时。在开始的两个时间段, 观测频率为1.4和1.9GHz (因为在早期, 低频滤的射电辐射可能会被GRB后的ejecta吸收掉), 之后只有1.4GHz的观测。观测数据由GUPPI记录。
- 每次观测前都会先观测一个已知的脉冲星来检查仪器状态。

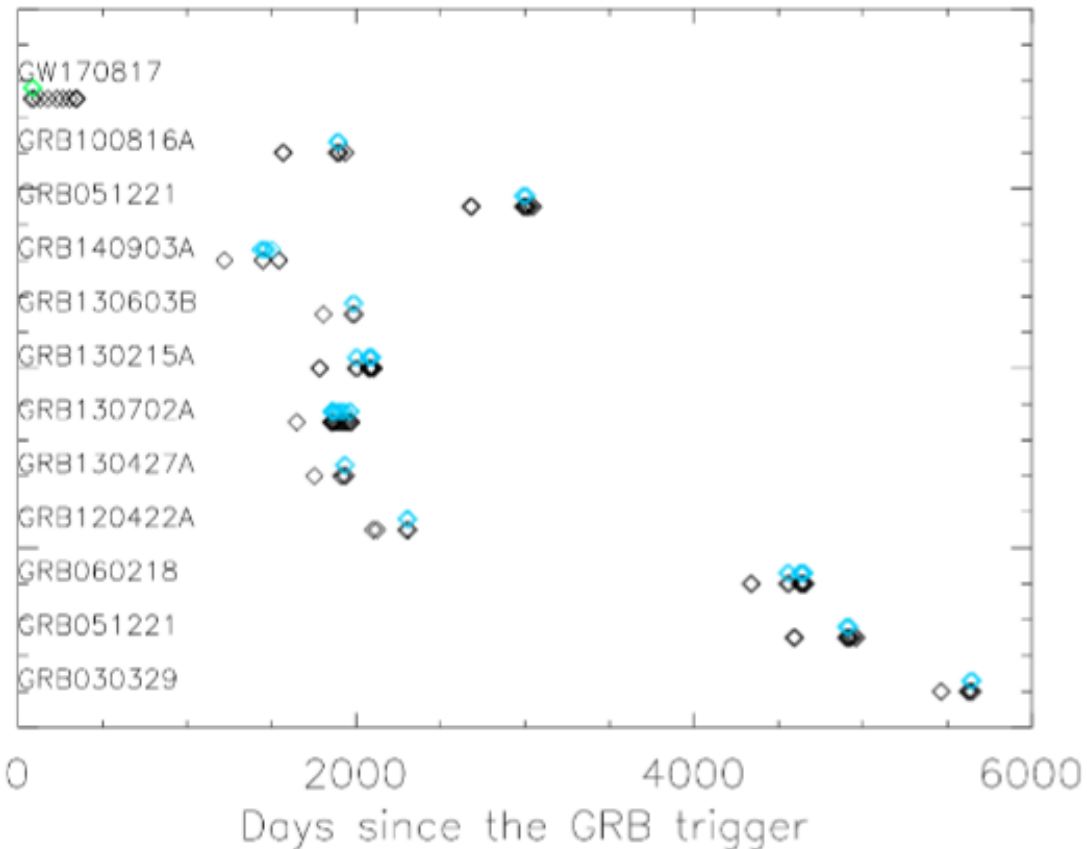


**Figure 1.** The timescale of our radio observations for the sources that are listed in Table 1 since the GRB trigger. All observations were made within a time span of 412 days, between the dates of November 2, 2017 and December 19, 2018. Our targets are arbitrarily offset along the y-axis for clarity. Black, blue and green diamonds represent 1.4 GHz, 4.5 GHz and 2 GHz observations, respectively. GRB 130702A was monitored  $\sim$  once a month in order to verify the origin of an excess dispersion measure seen on the first observation.

**Table 3.** GRB name, frequency, total time on the source, the number of epochs observed and the average time duration of each observation.

Name	Frequency (MHz)	Total Time (hours)	Number	Average Time (hours)
GRB 030329	1380	4.5	7	0.65
	4500	1.7	4	0.42
GRB 051221	1380	14.7	15	0.98
	4500	2.5	5	0.51
GRB 060218	1380	8.7	16	0.55
	4500	6.9	13	0.53
GRB 120422A	1380	3.5	4	0.88
	4500	1.2	2	0.60
GRB 130427A	1380	2.7	4	0.67
	4500	1.0	2	0.51
GRB 130702A	1380	13.7	21	0.65
	4500	6.9	15	0.46
GRB 130215A	1380	12.1	19	0.64
	4500	7.5	12	0.63
GRB 130603B	1380	2.3	3	0.76
	4500	1.0	2	0.50
GRB 140903A	1380	4.1	6	0.68
	4500	3.1	6	0.51
GRB 051221	1380	14.7	15	0.98
	4500	2.5	5	0.51
GRB 100816A	1380	5.4	8	0.67
	4500	1.3	3	0.44
GW 170817	1399	8.7	10	0.86
	1999	1.8	2	0.91

- 数据分析

- 使用 pipeline HEIMDALL 处理数据，并从中搜寻宽度为  $40.96 \mu s - 41.93 ms$  的脉冲，在  $S/N > 6$  的水平上一共找出 17672 个候选体。

- 使用卷积神经网络 FETCH 对这些候选体进行判断，分出 radio frequency interference (RFI) 和 潜在FRB候选体。设定判断阈值后，FETCH给出425个可能的FRB候选体，再经人工检查，最终找出68个单峰的候选体，不过这些信号都来自上面所说用来测试仪器状态的已知脉冲星，而其他的则是由附近的机场雷达发出的假脉冲。
- Detectability of a repeating FRB
  - 通过信噪比公式计算，分别对每个仪器在不同频段与S/N=10对应的通量上限（最低可观测流量）：
    - AO: 1.4GHz upper limit  $\approx 0.036 \text{ Jy ms}$  ; 4.5 GHz upper limit  $\approx 0.063 \text{ Jy ms}$
    - GBT: 1.4GHz upper limit  $\approx 0.085 \text{ Jy ms}$  ; 1.9 GHz upper limit  $\approx 0.098 \text{ Jy ms}$

Measured fluxes of bursts from the repeating FRB 121102 were scaled to the distance of each GRB to estimate the expected flux if a repeater-like source resided in the GRB site. Assuming radiometer noise limitations for each burst, the signal-to-noise ratio

$$S/N = \frac{FG\sqrt{N_p\Delta\nu}}{\beta T_{\text{sys}}\sqrt{w}}, \quad (3)$$

where  $F$  is the expected fluence given by  $F_{\min} = Sw$  where  $S$  is the flux,  $w = 1.0 \text{ ms}$  is the pulse width,  $T_{\text{sys}}$  is the system temperature,  $G$  is the telescope gain (the numbers given in Section 2),  $\Delta\nu$  is the bandwidth,  $\beta = 1.07$  accounts for digitization loss factors, and  $N_p = 2$  is the number of polarizations (Rane et al. 2016). From the radiometer equation, the minimum flux corresponding to  $S/N = 10$  for the AO setup is  $S_{\min} \approx 36 \text{ mJy}$  at 1.4 GHz and  $S_{\min} \approx 63 \text{ mJy}$  at 4.5 GHz. The minimum flux for GBT is  $S_{\min} \approx 84 \text{ mJy}$  at 1.4 GHz and  $S_{\min} \approx 98 \text{ mJy}$  at 1.9 GHz. Figure 3 shows

- 把FRB 121102的一系列爆发放到各个GRB的位置上，可以算出每次爆对应的预期观测流量，这些预期流量就可以与上面给出的上限进行比较，如

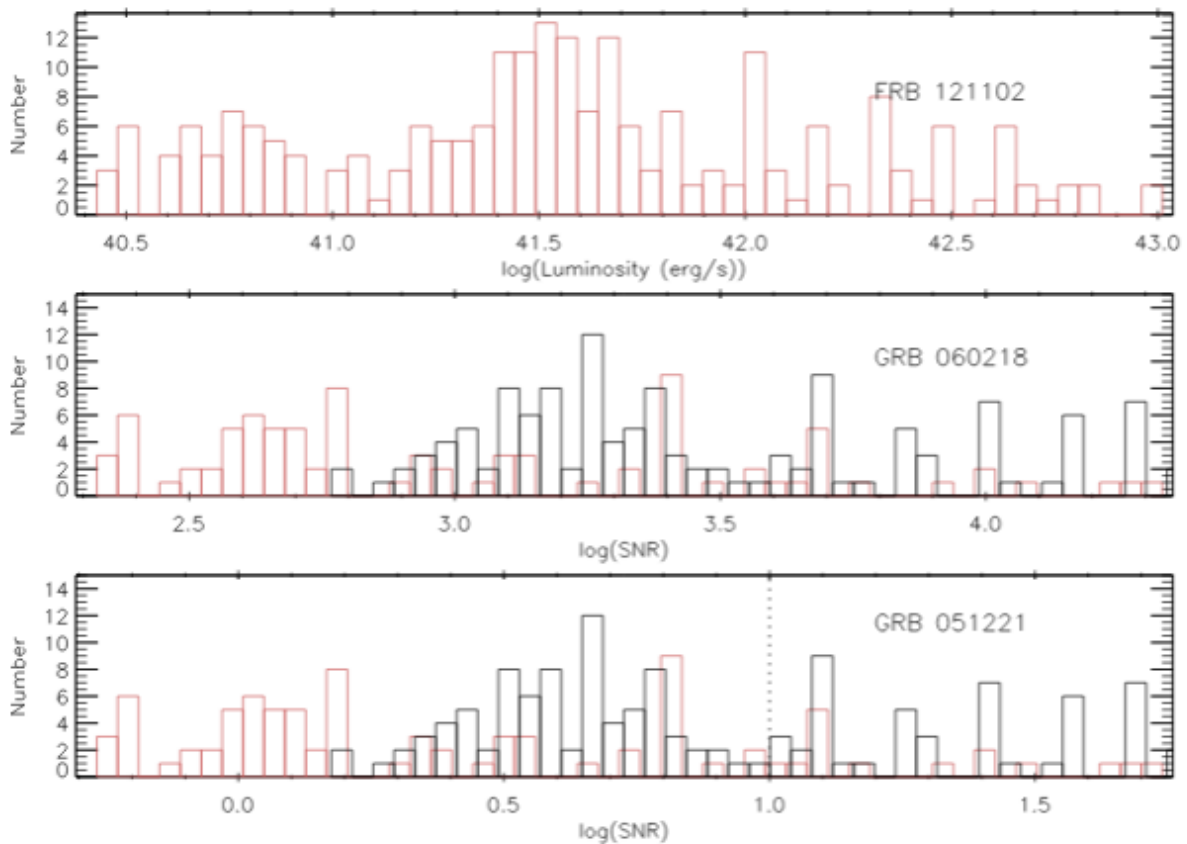


**Figure 3.** Luminosity distribution of FRB 121102 bursts (top), S/N histograms of GRB 060218 (middle) and GRB 051221 (bottom). The S/N histograms show the S/N at which FRB 121102-like bursts would be detected at given GRB distances. The black dotted vertical line corresponds to  $S/N = 10$ . The red and black S/N histograms represent bursts at 1.4 GHz and 4.5 GHz respectively.

- 如果磁星能够发出类似FRB121102的爆发，Arecibo应该有能力在4.8Gpc的距离上探测到 $\sim 9 \times 10^{42} \text{ erg/s}$ 的明亮爆发。
- 如果FRB的光度函数为Schechter function，则以上结果支持函数中应有一个较陡的幂律指数 ( $\alpha \leq -1.0$ ) 以及一个较大的截断光度 ( $L_0 \geq 10^{42} \text{ erg/s}$ )。

The rate of FRBs above a minimum luminosity  $L_{\min,i}$  may be expressed by the Schechter function (Schechter 1976) which gives the event rate density

$$\phi = \phi^* (L_{\min,i}/L_0)^\alpha e^{-L_{\min,i}/L_0}, \quad (4)$$

# The gravitational wave background signal from tidal disruption events

<https://arxiv.org/abs/2007.13225>

type:theory-TDE

comment:本文计算了两种TDE事件——星系核中SMBH瓦解主序星、球状星团中IMBH瓦解白矮星——中的被瓦解天体发出的引力波背景信号，并估计下一代天基引力波探测器是否能探测到这些信号。

## ► abstract

Authors: Martina Toscani (1), Elena M. Rossi (2), Giuseppe Lodato (1) ((1) Dipartimento di Fisica, Università Degli Studi di Milano, Via Celoria, 16, Milano, 20133, Italy, (2) Leiden Observatory, Leiden University, P0 Box 9513, 2300 RA, Leiden, the Netherlands)

Comments: Accepted for Publications in MNRAS. 11 pages, 5 figures

In this paper we derive the gravitational wave stochastic background from tidal disruption events (TDEs). We focus on both the signal emitted by main sequence stars disrupted by super-massive black holes (SMBHs) in galaxy nuclei, and on that from disruptions of white dwarfs by intermediate mass black holes (IMBHs) located in globular clusters. We show that the characteristic strain  $h_c$ 's dependence on frequency is shaped by the pericenter distribution of events within the tidal radius, and under standard assumptions  $h_c \propto f^{-1/2}$ . This is because the TDE signal is a burst of gravitational waves at the orbital frequency of the closest approach. In addition, we compare the background characteristic strains with the sensitivity curves of the upcoming generation of space-based gravitational wave interferometers: the Laser Interferometer Space Antenna (LISA), TianQin, ALIA, the DECIGO-hertz interferometer Gravitational wave Observatory (DECIGO) and the Big Bang Observer (BB0). We find that the background produced by main sequence stars might be just detected by BB0 in its lowest frequency coverage, but it is too weak for all the other instruments. On the other hand, the background signal from TDEs with white dwarfs will be within reach of ALIA, and especially of DECIGO and BB0, while it is below the LISA and TianQin sensitive curves. This background signal detection will not only provide evidence for the existence of

IMBHs up to redshift  $z \sim 3$ , but it will also inform us on the number of globular clusters per galaxy and on the occupation fraction of IMBHs in these environments.

- 本文计算了两种TDE事件——星系核中SMBH瓦解主序星、球状星团中IMBH瓦解白矮星——中的被瓦解天体发出的引力波背景信号，并估计下一代天基引力波探测器—the Laser Interferometer Space Antenna (LISA), TianQin, ALIA, the DECI-hertz interferometer Gravitational wave Observatory (DECIGO) and the Big Bang Observer (BBO)—是否能探测到这些信号。结果发现，对于前一种TDE的引力波信号，只有BBO能够在其最低频率探测到，而对于后一种，ALLA、DECIGO和BBO都可以探测到。
- 这样的探测工作可以为我们提供远距离 ( $z \sim 3$ ) IMBH存在的证据，以及提供关于星系中球状星团的数量，IMBH在球状星团中所占比例等信息。

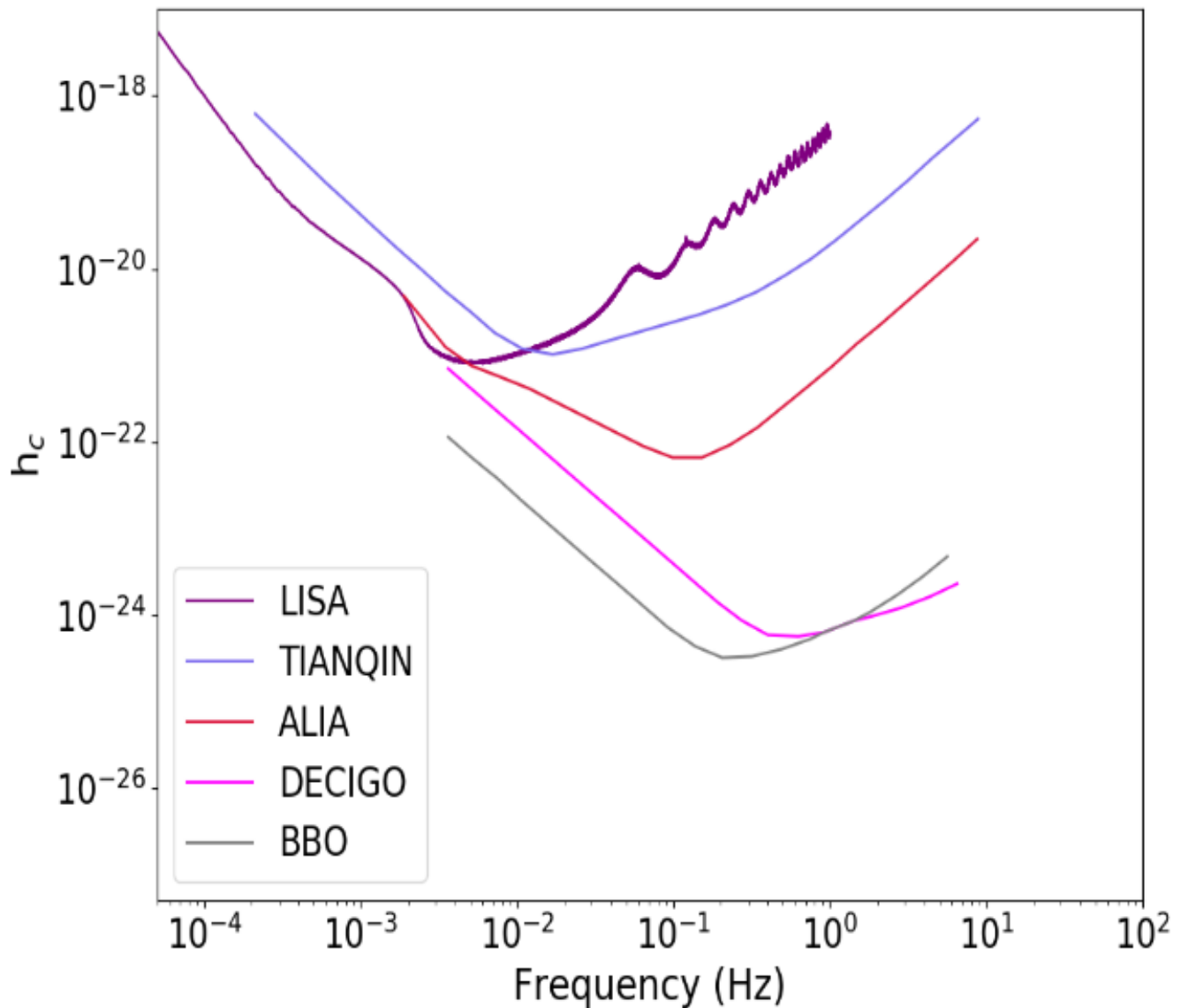


**Figure 2.** Sensitivity curves of LISA (purple), TianQin (light violet), ALIA (red), DECIGO (pink) and BBO (grey).

## Diverse Jet Structures Consistent with the Off-axis Afterglow of GRB 170817A

<https://arxiv.org/abs/2007.13116>

type:theory-GRB\_jet

comment:本文使用一种逆向构建喷流结构的方法，即通过给定的偏轴GRB余辉的光变曲线，不加任何函数形式的限制，反推喷流结构的方法，试图确定GRB 170817A的喷流结构

► abstract

Authors: Kazuya Takahashi, Kunihiro Ioka

Comments: 11 pages, 5 figures, 2 tables, submitted to MNRAS

The jet structure of short gamma-ray bursts (GRBs) has been controversial after the detection of GRB 170817A as the electromagnetic counterparts to the gravitational wave event GW170817. Different authors use different jet structures for calculating the afterglow light curves. We formulated a method to inversely reconstruct the jet structure uniquely from a given off-axis GRB afterglow, without assuming any functional form of the structure. By systematically applying our inversion method, we find that more diverse jet structures are consistent with the observed afterglow of GRB 170817A within errors: such as hollow-cone, spindle, Gaussian, and power-law jet structures. In addition, the total energy of the reconstructed jet is arbitrary, proportional to the ambient density  $n_0$ , with keeping the same jet shape if the parameters satisfy the degeneracy combination

$n_0 \varepsilon_B^{(p+1)/(p+5)} \varepsilon_e^{4(p-1)/(p+5)} = \text{const.}$ . Observational accuracy less than ~6 per cent is necessary to distinguish the different shapes, while the degeneracy of the energy scaling would be broken by observing the spectral breaks. Future events in denser environment with brighter afterglows and observable spectral breaks are ideal for our inversion method to pin down the jet structure, providing the key to the jet formation and propagation.

- 短暴GRB 170817A的结构性喷流一直以来讨论颇多。本文使用一种逆向构建喷流结构的方法，即通过给定的偏轴GRB余辉的光变曲线，不加任何函数形式的限制，反推喷流结构的方法，试图确定GRB 170817A的喷流结构，但发现多种喷流结构都在一定误差允许范围内与GRB 170817A的观测符合，如hollow-cone, spindle, Gaussian, and power-law jet structures。

# Revisiting AGN as the Source of IceCube's Diffuse Neutrino Flux

<https://arxiv.org/abs/2007.12706>

type:observation-neutrino

comment:本文使用IceCube三年的数据来寻找blazars ( 2860 sources in the Fermi 4LAC catalog) 和non-blazar AGN (65个, 63个包含在4LAC 中) 作为中微子源的证据

## ► abstract

Authors: Daniel Smith, Dan Hooper, Abby Vieregg

Comments: 14 pages, 7 figures, to be submitted to JCAP

The origin of the astrophysical neutrino flux reported by the IceCube Collaboration remains an open question. In this study, we use three years of publicly available IceCube data to search for evidence of neutrino emission from the blazars and non-blazar Active Galactic Nuclei (AGN) contained in the Fermi 4LAC catalog. We find no evidence that these sources produce high-energy neutrinos, and conclude that blazars can produce no more than 15% of IceCube's observed flux. The constraint we derive on the contribution from non-blazar AGN, which are less luminous and more numerous than blazars, is significantly less restrictive, and it remains possible that this class of sources could produce the entirety of the diffuse neutrino flux observed by IceCube. We anticipate that it will become possible to definitively test such scenarios as IceCube accumulates and releases more data, and as gamma-ray catalogs of AGN become increasingly complete. We also comment on starburst and other starforming galaxies, and conclude that these sources could contribute substantially to the signal observed by IceCube, in particular at the lowest detected energies.

- 本文使用IceCube三年的数据来寻找blazars ( 2860 sources in the Fermi 4LAC catalog) 和non-blazar AGN (65个, 63个包含在4LAC 中) 作为中微子源的证据。
- 作者没有发现证据表明这些源产生了高能中微子，并给出blazar来源的中微子不超过IceCube观测的15%的结论。
- 至于非blazar的AGN的贡献，作者不能给出严格的限制，并称这类源仍有可能是IceCube

探测到的全部diffuse neutrino flux的来源。

- 另外作者也提到星暴星系和其它starforming星系也能大量贡献观测到的中微子信号。

## On the Energy Sources of the Most Luminous Supernova ASASSN-15lh

<https://arxiv.org/abs/2007.13464>

type:theory-SN

comment:作者考虑了ejecta-circumstellar medium interaction加上伴随gamma-rays/X-rays leakage effect的磁星模型以消除理论光变曲线在晚期的超出，修改后的模型可以重现bolometric光变曲线

### ► abstract

Authors: Long Li, Zi-Gao Dai, Shan-Qin Wang, and Shu-Qing Zhong

In this paper, we investigate the energy-source models for the most luminous supernova ASASSN-15lh. We revisit the ejecta-circumstellar medium (CSM) interaction (CSI) model and the CSI plus magnetar spin-down with full gamma-ray/X-ray trapping which were adopted by Chatzopoulos et al.(2016) and find that the two models cannot fit the bolometric LC of ASASSN-15lh. Therefore, we consider a CSI plus magnetar model with the gamma-rays/X-rays leakage effect to eliminate the late-time excess of the theoretical LC. We find that this revised model can reproduce the bolometric LC of ASASSN-15lh. Moreover, we construct a new hybrid model (i.e., the CSI plus fallback model), and find that it can also reproduce the bolometric LC of ASASSN-15lh. Assuming that the conversion efficiency ( $\eta$ ) of fallback accretion to the outflow is typically  $\sim 10^{-3}$ , we derive that the total mass accreted is  $\sim 3.9 M_{\odot}$ . The inferred CSM mass in the two models is rather large, indicating that the progenitor could have experienced an eruption of hydrogen-poor materials followed by an energetic core-collapse explosion leaving behind a magnetar or a black hole.

- 目前学界存在多种模型解释超亮超新星的能源机制问题，如pair instability SN, 磁星自旋减慢, 喷射物与星周介质相互作用, 回落吸积等模型。本文讨论了超新星ASASSN-

15lh—最明亮的超新星（峰值热光度为 $(2.2 \pm 0.2) \times 10^{45} \text{ erg/s}$ ）—的能量来源模型。

- 文章首先回顾了Chatzopoulos et al. (2016)采用的两种模型：ejecta-circumstellar medium interaction (CSI)模型和CSI加上伴随 full gamma-ray/X-ray trapping的磁星自旋减慢模型，发现这两种模型均不能拟合ASASSN-15lh的bolometric光变曲线。
- 故作者考虑了CSI加上伴随gamma-rays/X-rays leakage effect的磁星模型以消除理论光变曲线在晚期的超出，修改后的模型可以重现bolometric光变曲线。另外作者还考虑了CSI加回落吸积的组合模型，在一定条件下也能重现光变曲线，此情况下假设回落吸积物质到外流的转化效率为典型的 $\sim 10^{-3}$ ，则总吸积质量约为 $3.9 M_{\odot}$ 。
- 两种模型导出的CSM质量都比较大 (SN ejecta + CSM:  $\sim 61 M_{\odot}$ ,  $\sim 47 M_{\odot}$ )，表明前身星可能是经历了一次少氢物质的爆发，随后是一次高能的核塌缩爆炸，留下一个磁星或是黑洞。

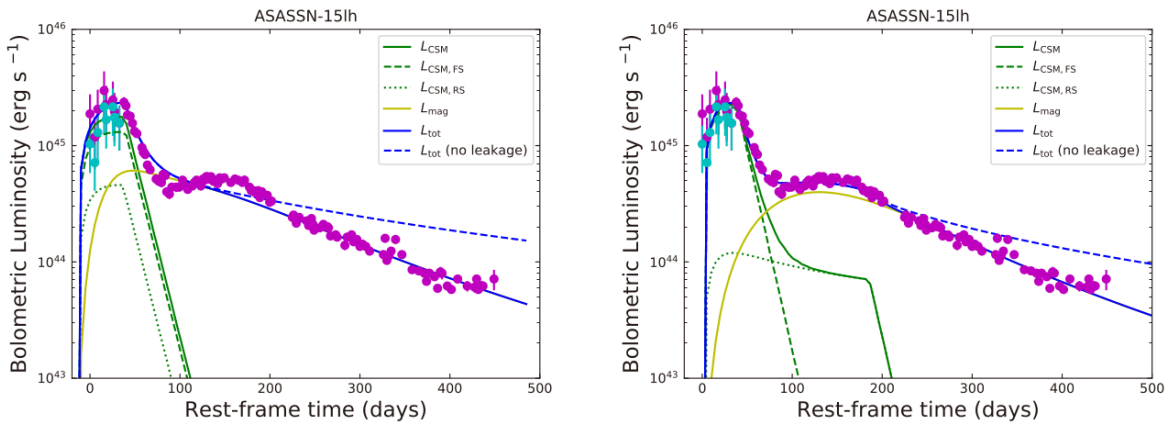


**Figure 2.** The bolometric LCs of ASASSN-15lh reproduced by the CSI plus magnetar model:  $s = 0$  (the left panel) and  $s = 2$  (the right panel). The total luminosity ( $L_{\text{tot}}$ ) are shown by solid blue curves and the contributions from the forward shock ( $L_{\text{CSI,FS}}$ ), the reverse shock ( $L_{\text{CSI,RS}}$ ), and the magnetar spin-down ( $L_{\text{mag}}$ ) are shown in dashed green, dotted green, and solid yellow curves, respectively. The dashed blue curves represent the total luminosity that the leakage effect is not taken into account. Data are taken from Godoy-Rivera et al. (2017).

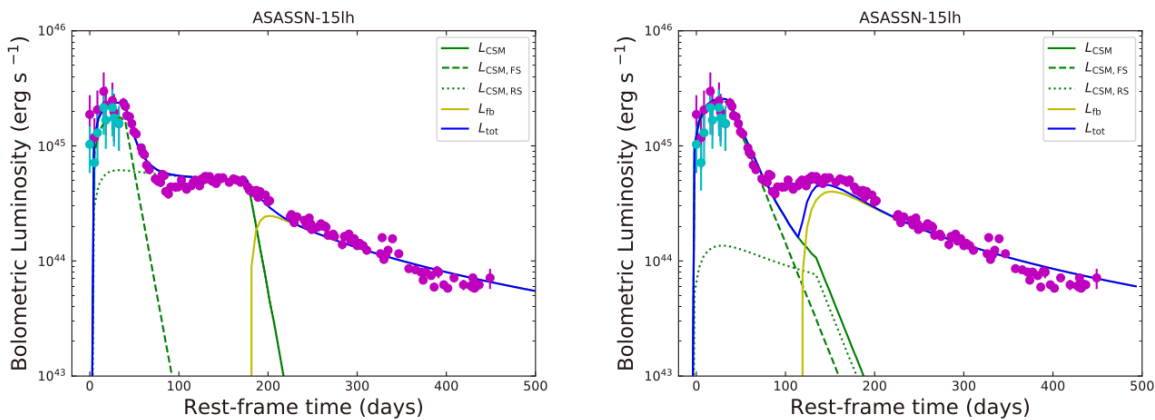


**Figure 4.** The bolometric LCs of ASASSN-15lh reproduced by the CSI plus fallback model:  $s = 0$  (the left panel) and  $s = 2$  (the right panel). The total luminosity ( $L_{\text{tot}}$ ) are shown by solid blue curves. The contributions from the forward shock ( $L_{\text{CSI,FS}}$ ), the reverse shock ( $L_{\text{CSI,RS}}$ ), and the fallback accretion ( $L_{\text{fb}}$ ) are shown by dashed green, dotted green, and solid yellow curves, respectively. Data are taken from Godoy-Rivera et al. (2017).

# PTF11rka: an interacting supernova at the crossroads of stripped-envelope and H-poor superluminous stellar core collapses

<https://arxiv.org/abs/2007.13144>

type:observation-SN

comment:作者对少氢超新星 PTF11rka ( $z=0.074$ )的观测数据，包括光变曲线和光谱，进行了讨论分析

## ► abstract

The hydrogen-poor supernova PTF11rka ( $z = 0.0744$ ), reported by the Palomar Transient Factory, was observed with various telescopes starting a few days after the estimated explosion time of 2011 Dec. 5 UT and up to 432 rest-frame days thereafter. The rising part of the light curve was monitored only in the  $R_{PTF}$  filter band, and maximum in this band was reached  $\sim 30$  rest-frame days after the estimated explosion time. The light curve and spectra of PTF11rka are consistent with the core-collapse explosion of a  $\sim 10 M_\odot$  carbon-oxygen core evolved from a progenitor of main-sequence mass 25–40  $M_\odot$ , that liberated a kinetic energy ( $E_K$ )  $\sim 4 \times 10^{51} erg$ , expelled  $\sim 8 M_\odot$  of ejecta ( $M_{ej}$ ), and synthesised  $\sim 0.5 M_\odot$  of  $^{56}Ni$ . The photospheric spectra of PTF11rka are characterised by narrow absorption lines that point to suppression of the highest ejecta velocities  $>\sim 15,000$  km/s. This would be expected if the ejecta impacted a dense, clumpy circumstellar medium. This in turn caused them to lose a fraction of their energy ( $\sim 5 \times 10^{50} erg$ ), less than 2% of which was converted into radiation that sustained the light curve before maximum brightness. This is reminiscent of the superluminous SN 2007bi, the light-curve shape and spectra of which are very similar to those of PTF11rka, although the latter is a factor of 10 less luminous and evolves faster in time. PTF11rka is in fact more similar to gamma-ray burst supernovae (GRB-SNe) in luminosity, although it has a lower energy and a lower  $E_K/M_{ej}$  ratio.

- 尽管stripped-envelope和更大质量的H-poor超亮超新星在观测上有所不同，但这两类事件间仍存在一些联系，包括内秉性质，CSM起的作用，以及超亮超新星和最高能（the most energetic）的H-poor超新星都有可能是磁星旋转驱动的。通过广域巡天项目（large area sky survey）对超新星的系统准确的调查和研究，会发现一些具有中间性质的目标，把看上去不相关的两类超新星联系起来（This systematic approach makes unbiased detections possible and brings to evidence objects with intermediate properties that bridge seemingly separate groups）。一个关键的例子就是H- 和 He-poor的Ic型 SN PTF11rka。PTF11rka的光变曲线形状和光球阶段的光谱均与超亮的pair-instability（正负电子对的产生导致热核爆发）超新星，SN 2007bi相似，使得PTF11rka成为联系stripped-envelope SNe（窄线和宽线的Ic SNe）与H-poor SLSNe的一个值得监测的目标。
- 作者对少氢超新星 PTF11rka ( $z=0.074$ ) 的观测数据，包括光变曲线和光谱，进行了讨论分析。
- 测光开始于爆后数天（估计爆发时间为2011年12月5日UT），并一直持续，最后一次观测在开始观测的432天后。PTF11rka光变的上升阶段仅有 $R_{PTF}$ 波段（P48）的数据，该波段下大概在爆后30天左右达到峰值。之后P60也参与进来，提供了gri波段的数据。在最后的fully nebular phase，即430天左右，由VLT提供了BVRI的数据。文中提到g波段的峰值至少发生在r波段，i波段的峰值的15天前，表明这个SN的光变有很强的色差行为。根据这些数据，作者构造了pseudebolometric光变曲线（注意在最大亮度达到前只有 $R_{PTF}$ 波段的数据，因此只能基于一定假设构造早期的pseudobolometric光变曲线，导致其的峰值有很大的不确定性。SN 2007bi的情况也类似）。

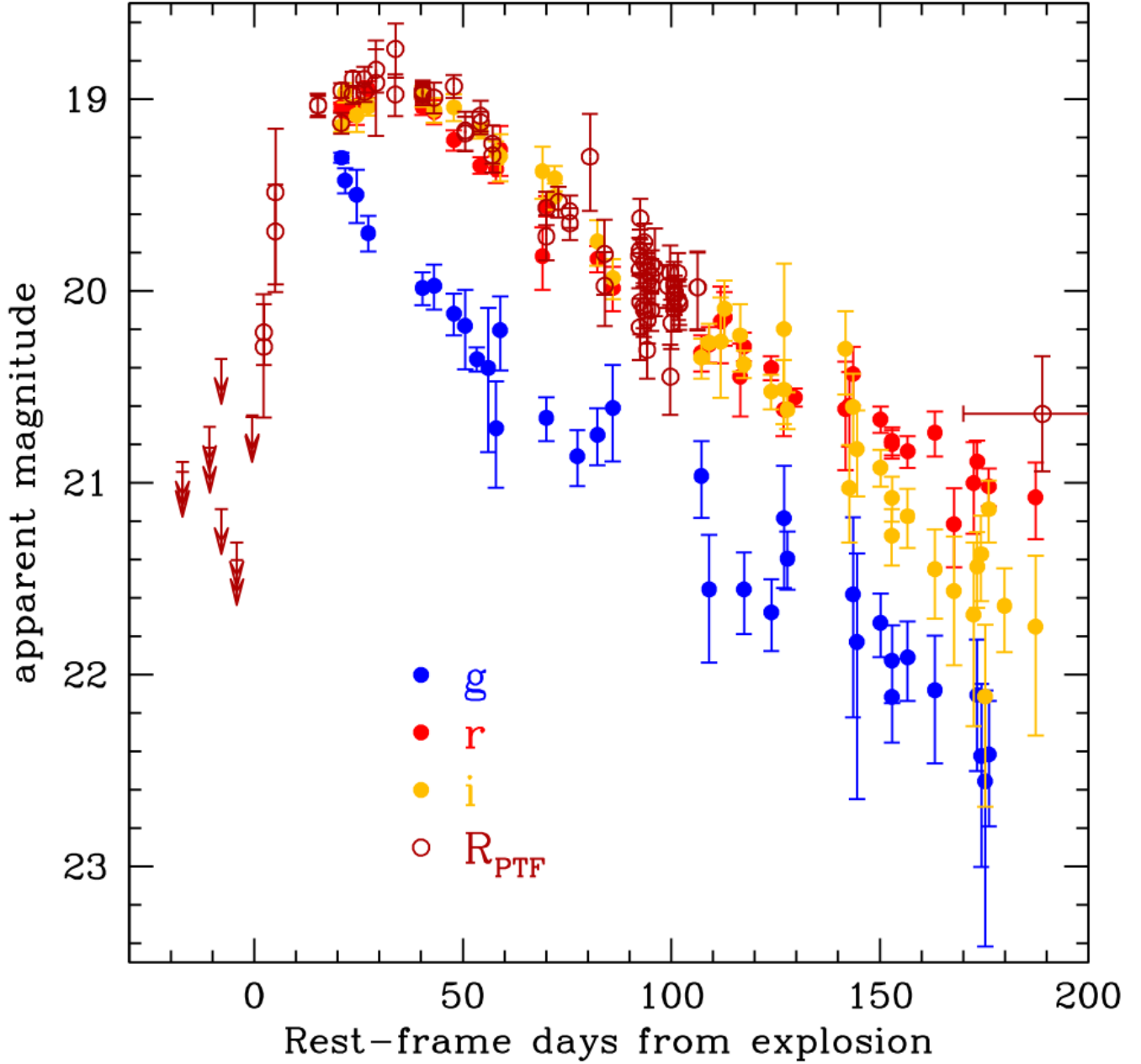


**Figure 1.** Multiband light curves of PTF11rka in the rest frame (the photometry at  $t = 430$  days is not included). The zero point of the abscissa corresponds to the estimated explosion time (2011 Dec. 5). The magnitudes are corrected for Galactic extinction ( $E(B-V) = 0.034$  mag), K-corrected, and host-galaxy-subtracted using a template derived from the VLT spectrum (see Section 3.2 and Fig. 4). The  $R_{\text{PTF}}$  data points between days 170 and 200 have been averaged.

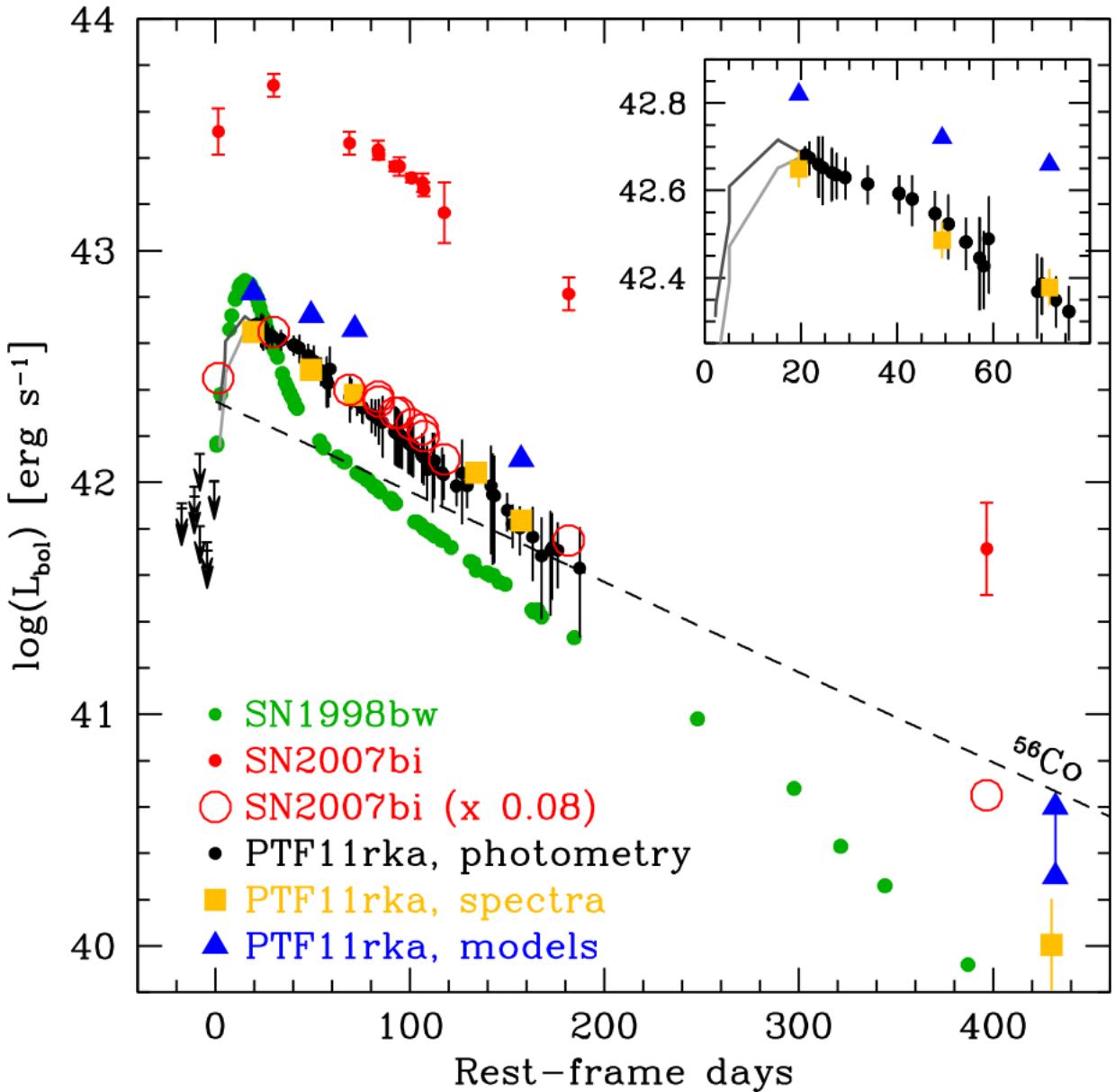


**Figure 2.** Pseudobolometric light curve of PTF11rka (black), compared with those of H-poor energetic SN 1998bw (green) and superluminous SN 2007bi (red) in the rest-frame 3500–9500 Å range. The early portion of the light curve of PTF11rka (see inset), which is based only on  $R_{\text{PTF}}$  measurements, is represented as curves computed under the assumption of constant  $g - r$  colour (light grey) and variable  $g - r$  colour (dark grey). The upper limits were obtained from the  $R_{\text{PTF}}$  upper limits under the assumption of a constant bolometric correction. The yellow squares represent the fluxes from the spectra of PTF11rka, integrated over the same wavelength range. The uncertainties of the SN 1998bw points are equal to, or smaller than, the symbol size. The zero of time corresponds to the explosion epoch for PTF11rka and SN 1998bw. Note that the pseudobolometric light-curve maximum of PTF11rka seems to precede the  $R_{\text{PTF}}$ -band maximum by  $\sim 10$  days (Fig. 1), but this is highly uncertain (see Section 3.1). The phases of SN 2007bi, whose explosion time is very poorly determined, were shifted so that its time of maximum brightness matches the  $R_{\text{PTF}}$ -band maximum time of PTF11rka (30 days after explosion). The first point of the light curve of SN 2007bi was obtained from the  $r$ -band light curve reported by Gal-Yam et al. (2009) by assuming a difference between  $r$ -band and pseudobolometric flux equal to that at peak luminosity (the uncertainty is reflected in the relatively large error bar). The large red open circles represent the pseudobolometric light curve of SN 2007bi scaled down to match the luminosity of PTF11rka. The two light curves are very similar. The blue triangles are the input luminosities of the spectral models (see Section 4.1); for the nebular epoch (day 432), both low- and high-mass solutions are shown. The  $^{56}\text{Co}$  radioactive decay law is shown for reference (dashed line). For all SNe we adopted the concordance cosmology and  $H_0 = 73 \text{ km s}^{-1} \text{ Mpc}^{-1}$  (see Section 1).

- 测光期间一共进行了6次测谱。

**Table 2.** Summary of spectroscopic observations of PTF11rka.

Date (UT)	MJD <sup>a</sup> (days)	Phase <sup>b</sup>	Telescope	Instrument
2011 Dec 26	55921	20	Keck-I	LRIS
2012 Jan 27	55953	49	KPNO 4 m	RC Spectrograph
2012 Feb 20	55977	72	Keck-I	LRIS
2012 Apr 27	56044	134	Keck-I	LRIS
2012 May 22	56069	157	Keck-I	LRIS
2013 Mar 13	56364	432	VLT	FORS2+300V

<sup>a</sup> Observing epoch (= JD – 2,400,000.5).

<sup>b</sup> In rest-frame, computed from the epoch of estimated explosion (2011 Dec. 5).

- PTF11rka在20天时的光谱与SN 2007bi在峰值后50天（爆发后120天）时的光谱非常相似，表明前者演化较快，其光球速度应该也与SN 2007bi50天时测量的结果，~12000 km/s接近。

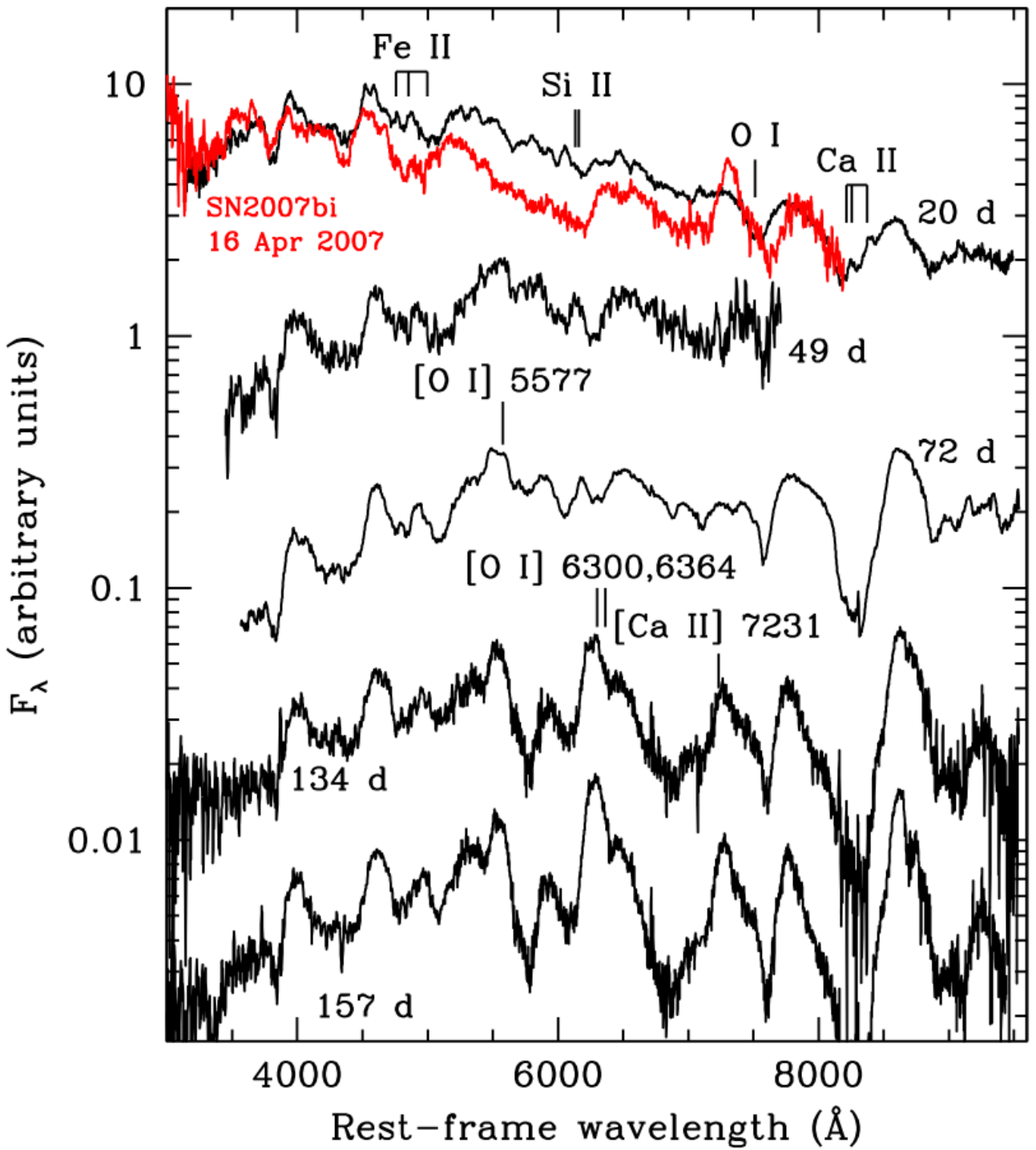


**Figure 3.** First five spectra of PTF11rka, corrected for Galactic extinction ( $E(B-V) = 0.034$  mag), redshift ( $z = 0.0744$ ), and host galaxy contribution (evaluated as detailed in Section 3.2). The phase is indicated close to each spectrum as rest-frame days with respect to explosion. The absorption and emission features that are discussed in Section 4.1 are indicated with vertical bars. The absorption line marks are placed at the wavelengths expected for a blue-shift caused by an expansion velocity of  $10,000 \text{ km s}^{-1}$ . For comparison, the first recorded spectrum of SN 2007bi (corrected for  $z = 0.1279$  and extinction  $E(B-V) = 0.024$  mag) is shown (red) at a rest-frame phase that could be  $\sim 50$  rest-frame days after maximum light or  $\sim 120$  rest-frame days after explosion. All spectra are smoothed with a  $10 \text{ \AA}$  boxcar and arbitrarily scaled in flux density.

- PTF11rka 和 SN 2007bi 的星云阶段光谱存在一些不同，比较显著的一点就是很弱的铁线表明前者较后者只合成了少量的 $^{56}\text{Ni}$ ，这一点从光变曲线独立得出。

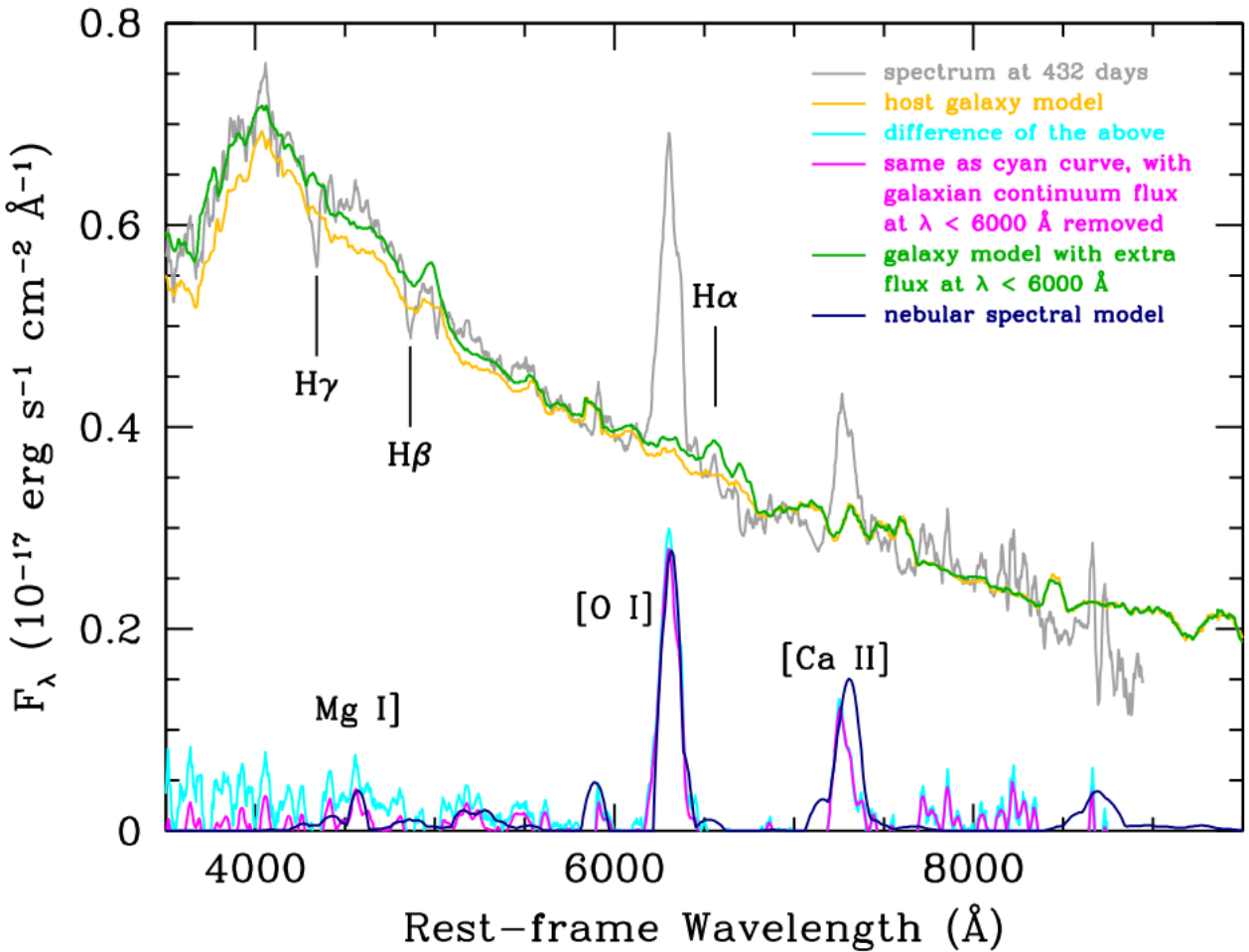


**Figure 4.** Spectrum (grey) taken on 2013 Mar. 13 (432 rest-frame days after the explosion), flux-calibrated against the simultaneous photometry, corrected for Galactic extinction ( $E(B - V) = 0.034$  mag), de-redshifted, and smoothed with a 10 Å boxcar. The adopted host-galaxy template, from Kinney, et al. (1996), is shown in yellow and the difference between the two spectra in cyan. A small residual continuum contribution (perhaps due to the presence of a star-forming region underlying the SN) is still present shortward of 6000 Å and further subtracted to obtain the final decomposed spectrum (magenta). This extra continuum is added to the galaxy template to yield the actual galaxy flux at the SN location (green). The nebular spectral model presented in Section 4.1.5 is shown in dark blue and the strongest emission lines are marked.

- 在模型拟合环节，作者使用最早的20天的光谱来确定爆发外层 (outer layer) 的参数 (如velocity cut,  $E_K$ )，用光变曲线估计喷射物质量  $M_{ej}$ ，以及用光变曲线 (由光谱数据拟合的光变曲线) 和晚期光谱估计 56Ni 的合成质量。
  - 采用与 Moriya et al 2010 用来拟合 SN 2007bi 的模型一样的喷射物密度结构，PTF11rka 给出  $E_K \sim 4 \times 10^{51} \text{ erg}$ ,  $M_{ej} \sim 8M_\odot$ ，这样  $E_K/M_{ej} \approx 0.5$  就相对较低。SN 2007bi 的相关量为  $56\text{Ni} \sim 6M_\odot$ ,  $M_{ej} \sim 40M_\odot$ ,  $E_K \sim 3.6 \times 10^{52}$ ,  $E_K/M_{ej} \approx 1$ ，ejecta velocity cut  $\sim 13000 - 16000 \text{ km/s}$  (Moriya T. J., Mazzali P. A., & Tanaka M. 2019b)。
  - 通过拟合 20 天的光谱，作者将喷射物的分布在 15000 km/s 处截断，并给出  $M_{ej} \approx 7.9M_\odot$ ,  $E_k \approx 3.5 \times 10^{51} \text{ erg}$ 。
  - 这样就给出，质量约为  $0.1M_\odot$  的部分喷射物“撞进”了一个密度较大，比较厚重的星周介质中，损失了  $\sim 5 \times 10^{50} \text{ erg}$  的能量，根据光变曲线的拟合，其中有大概 2% 的能

量被辐射出来。

- 另外根据光变曲线的拟合，估计 $^{56}\text{Ni}$ 的产量为 $0.5 M_{\odot}$ 是必要的，以此匹配接近峰值时的光度  $\sim 10^{43} \text{ erg/s}$ 。这个估计比用晚期星云阶段光谱估计 ( $\sim 0.4 M_{\odot}$ ) 的大，可能是因为部分 $^{56}\text{Ni}$ 由于速度大于星云速度 (4000 kms)，从而没有在晚期星云光谱作出贡献。

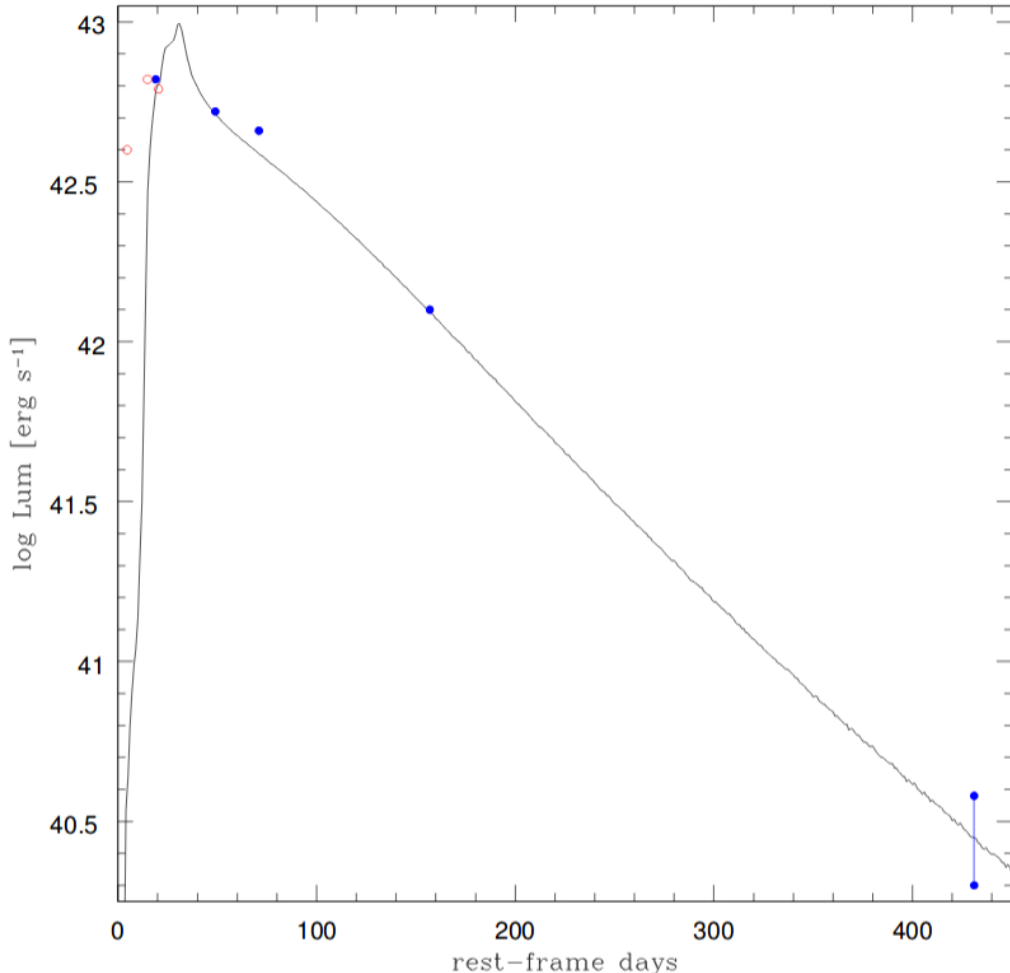


**Figure 9.** Light-curve model (black curve). The blue filled circles represent the input luminosities of the spectral models. The vertical bar at 432 days represents the range of luminosities covered by the two adopted mass solutions for the nebular phase (Section 4.1.5). The open red circles represent the pre-maximum bolometric light-curve points, obtained by multiplying the  $R_{\text{PTF}}$  fluxes by a constant amount equivalent to the ratio between the model luminosity at day 20d and the simultaneous  $R_{\text{PTF}}$  flux.

## • 总结

- 首先，PTF11rka的光谱和大部分的光变曲线在很大程度上都可以在传统框架下去解释，即超新星喷发出大质量的恒星核，且 $^{56}\text{Ni}$ 的放射性衰变支持着观测的光度 (SN ejects a massive stellar core and the luminosity is supported by the radioactive decay of  $^{56}\text{Ni}$ )。所需要的 $^{56}\text{Ni}$ 的质量相当大 $\sim 0.4 - 0.5 M_{\odot}$ ，与GRB-SNe相当。另外，喷射物质量的估计值， $M_{ej} \sim 8 \pm 2 M_{\odot}$ 也是在 stripped-envelope 核塌缩SNe 的 $M_{ej}$ 分布中处于较高的一部分。根据 $M_{ej}$ ，可推断出C0核心的质量在 $8 - 13 M_{\odot}$ 之间，前身主序星为 $25 - 40 M_{\odot}$ 之间。具体取决于残骸是低质量中子星还是黑洞。其动能  $E_K \sim 4 \times 10^{51} \text{ erg}$  虽然高但并不极端，

更像是没有伴随GRB的明亮的 stripped-envelope SNe。

- 然而，PTF11rka的早期光谱与SLSN 2007bi的相似。最近的一些工作表明其爆发的CO核心质量为 $\sim 40M_{\odot}$ （前身星可能有 $60 - 80M_{\odot}$ ）。尽管质量很大，SN 2007bi的爆发也没有特别高能（ $E_K \approx 4 \times 10^{52} erg, E_K/M_{ej} \approx 1$ ）。其光谱的拟合情况表明2007bi和PTF11rka一样，喷射物也是与CSM撞击而被减速。
- PTF11rka的峰值光度与H-poor SNe的峰值光度的对比表明，前者光度大约比SLSNe低一个量级，且正好处在Ib/c型超新星的范围，而在宽线Ic型超新星中处于较低光度水平。特别的， $^{56}\text{Ni}$ 的质量非常接近于SN 1998bw，且其宽光变曲线的形状和峰值光度也与“spectroscopically normal” Type Ic SN 2011bm相似。
- 从光谱的角度来看，尽管PTF11rka在早期与SLSN 2007bi相似，但其后期光谱（爆发后的157和432天）则有H-poor的普通SNe，宽线SNe和SLSNe的影子。（Its late-time spectra are reminiscent of those of H-poor normal SNe, broad-lined SNe, and SLSNe）
- 以上这些性质使得PTF11rka将普通超新星，energetic stripped-envelope超新星（包括GRB-SNe）以及H-poor 超亮超新星联系起来（gap-bridging）。另外，作者提到PTF11rka和SLSN 2007bi之间的相似表明 $^{56}\text{Ni}$ 以及CSM的相互作用在H-poor SLSNe的研究中的作用不能忽略。

## 200729

---

### Spectroscopic properties of the dwarf nova-type cataclysmic variables observed by LAMOST

<https://arxiv.org/abs/2007.14016>

type:observation-dwarf\_nova

comment:作者使用LAMOST对76个已知的矮新星拍摄了131张光谱，讨论了它们的光谱性质

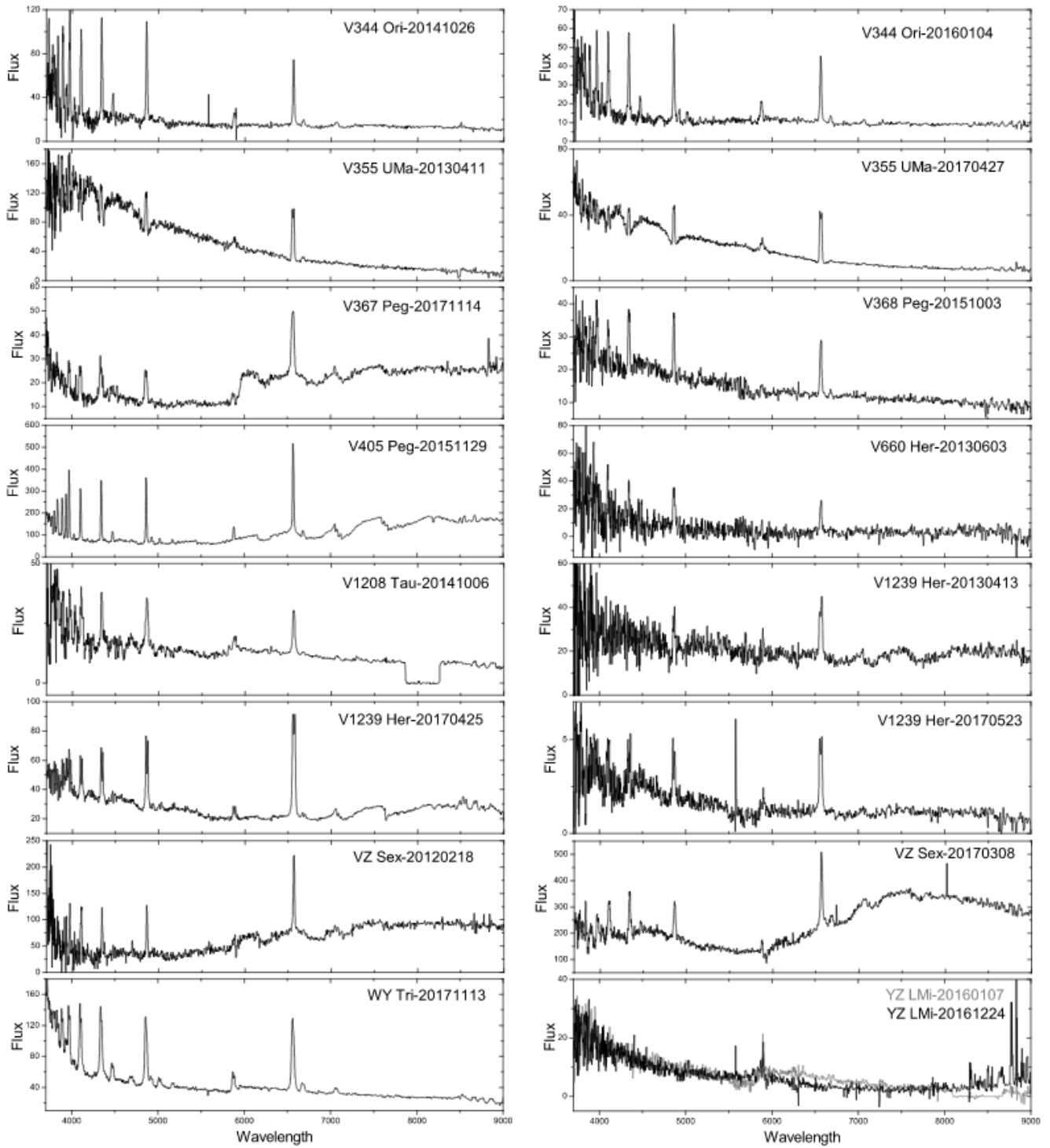
► abstract

Authors: Han Zhongtao, Boonrucksar Soonthornthum, Qian Shengbang, et al.

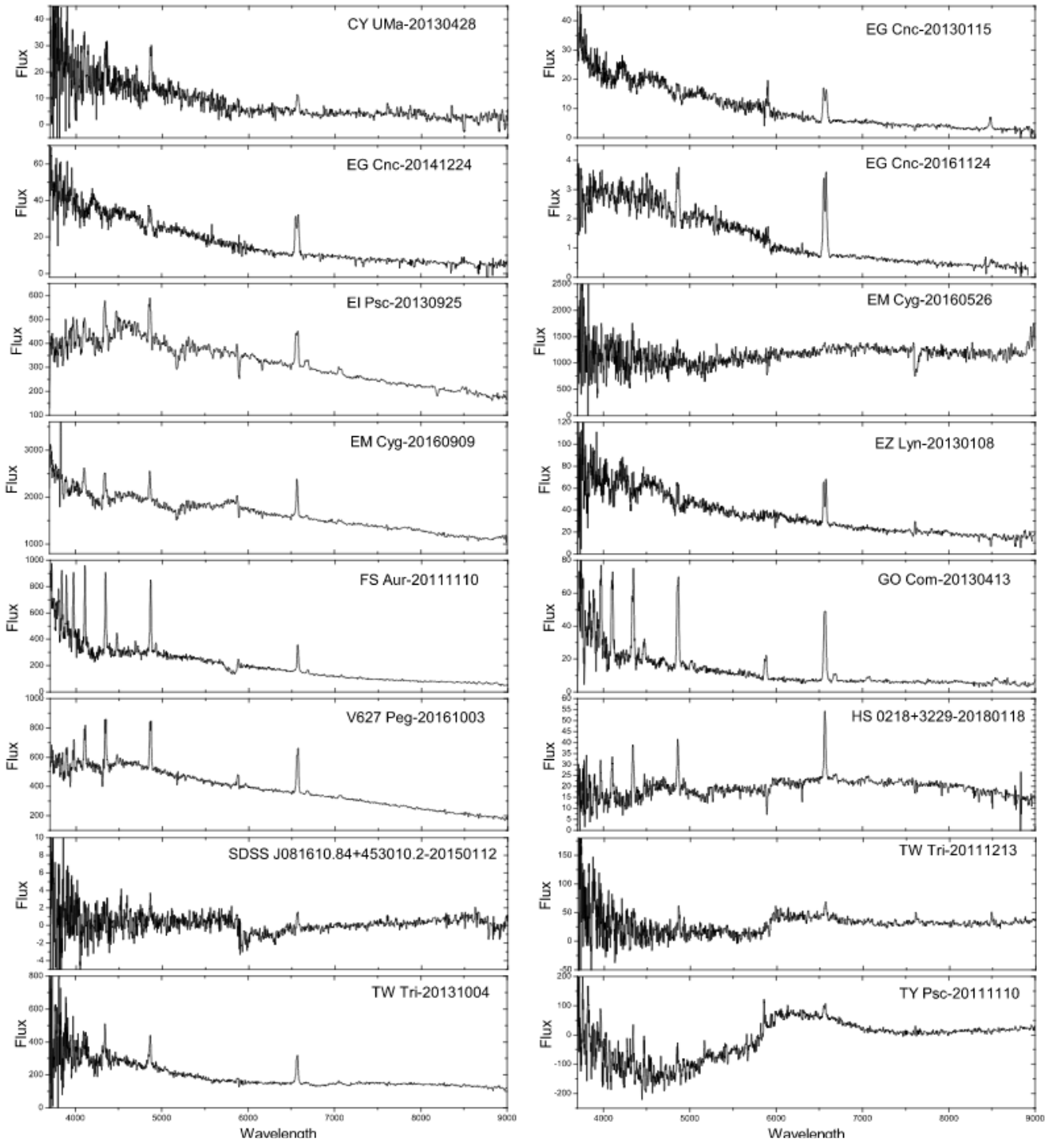
Comments: 29 pages, 11 figures

Spectra of 76 known dwarf novae from the LAMOST survey were presented. Most of the objects were observed in quiescence, and about 16 systems have typical outburst spectra. 36 of these systems were observed by SDSS, and most of their spectra are similar to the SDSS spectra. 2 objects, V367 Peg and V537 Peg, are the first to observe their spectra. The spectrum of V367 Peg shows a contribution from a M-type donor and its spectral type could be estimated as M3–5 by combining its orbital period. The signature of white dwarf spectrum can be seen clearly in four low-accretion-rate WZ Sge stars. Other special spectral features worthy of further observations are also noted and discussed. We present a LAMOST spectral atlas of outbursting dwarf novae. 6 objects have the first outburst spectra, and the others were also compared with the published outburst spectra. We argue that these data will be useful for further investigation of the accretion disc properties. The HeII  $\lambda$ 4686 emission line can be found in the outburst spectra of seven dwarf novae. These objects are excellent candidates for probing the spiral asymmetries of accretion disc.

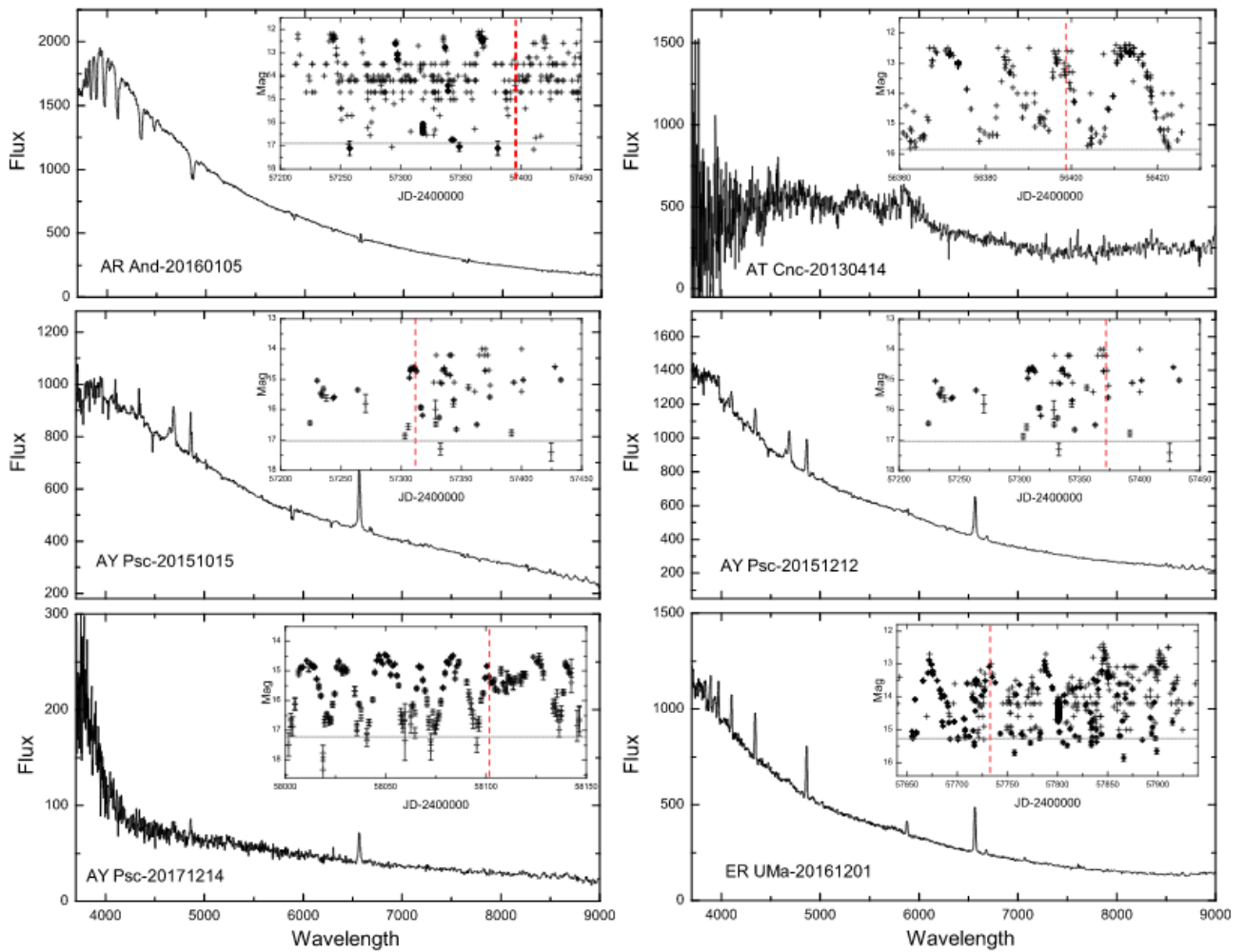
- 作者使用LAMOST对76个已知的矮新星拍摄了131张光谱，讨论了它们的光谱性质
- 大部分光谱是在矮新星的沉默阶段的光谱（光学薄，主要呈现较强的Balmer线和中性氦系列线叠加在较平坦的连续谱上），而有16个系统的光谱是比较典型的爆发时期的光谱（变为光学厚，吸收线变为主要特征，且由于吸积盘温度高，连续谱偏蓝）。



**Fig. 6.** LAMOST quiescence spectra of eleven dwarf novae: V344 Ori, V355 UMa, V367 Peg, V368 Peg, V405 Peg, V660 Her, V1208 Tau, V1239 Her, VZ Sex, WY Tri and YZ LMi (AM CVn star).

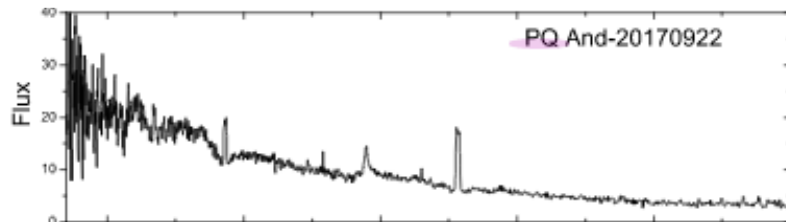


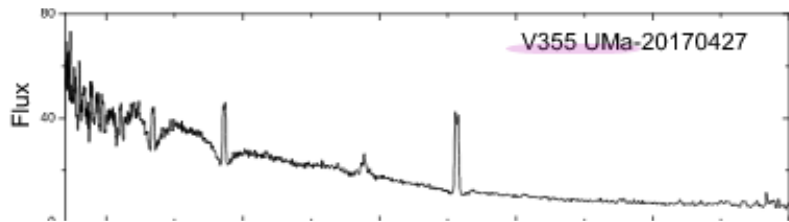
**Fig. 7.** LAMOST spectra obtained near outburst (before and after) of twelve dwarf novae: CY UMa, EG Cnc, EI Psc, EM Cyg, EZ Lyn, FS Aur, GO Com, V627 Peg, HS 0218+3229, SDSS J081610.84+453010.2, TW Tri and TY Psc.



**Fig. 8.** LAMOST outburst spectra of four dwarf novae: AR And, AT Cnc, AY Psc and ER UMa. The AAVSO light curves corresponding to the spectra are plotted in the inset, and a red dashed line denotes the dates for observing the spectrum.

- V367 Peg V537 Peg这两个目标是首次被拍光谱，其中V367 Peg的光谱显示出了伴星（donor）的M型光谱。
- 另外，在4个低吸积率的系统（WZ Sge stars, EG Cnc, EZ Lyn, PQ And and V355 UMa）的光谱中显漏出自矮星的光谱（通常由比较陡的“蓝色”连续谱加上围绕Balmer线的较宽的吸收“翼” → often reveal a steep blue continuum plus broad absorption wings around the Balmer emissions）





- 最后提到outburst时期的光谱可用来研究吸积盘的性质。

## SN 2018zd: An Unusual Stellar Explosion as Part of the Diverse Type II Supernova Landscape

<https://arxiv.org/abs/2007.14348>

type:observation-IIInSN

comment:本文发表了对SN 2018zd的前450天的观测情况。

### ► abstract

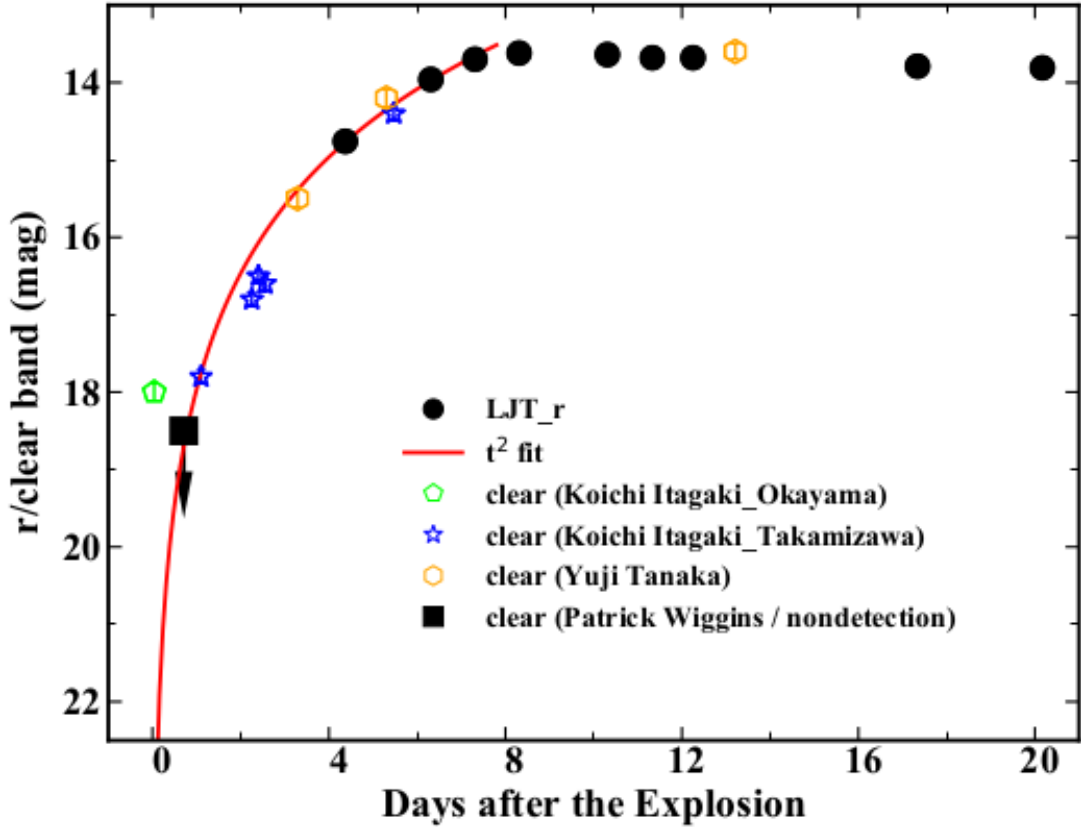
Authors: Jujia Zhang, Xiaofeng Wang, Jozsef Vinko et al.

Comments: Accepted for publication in MNRAS, 20 pages, 11 figures.

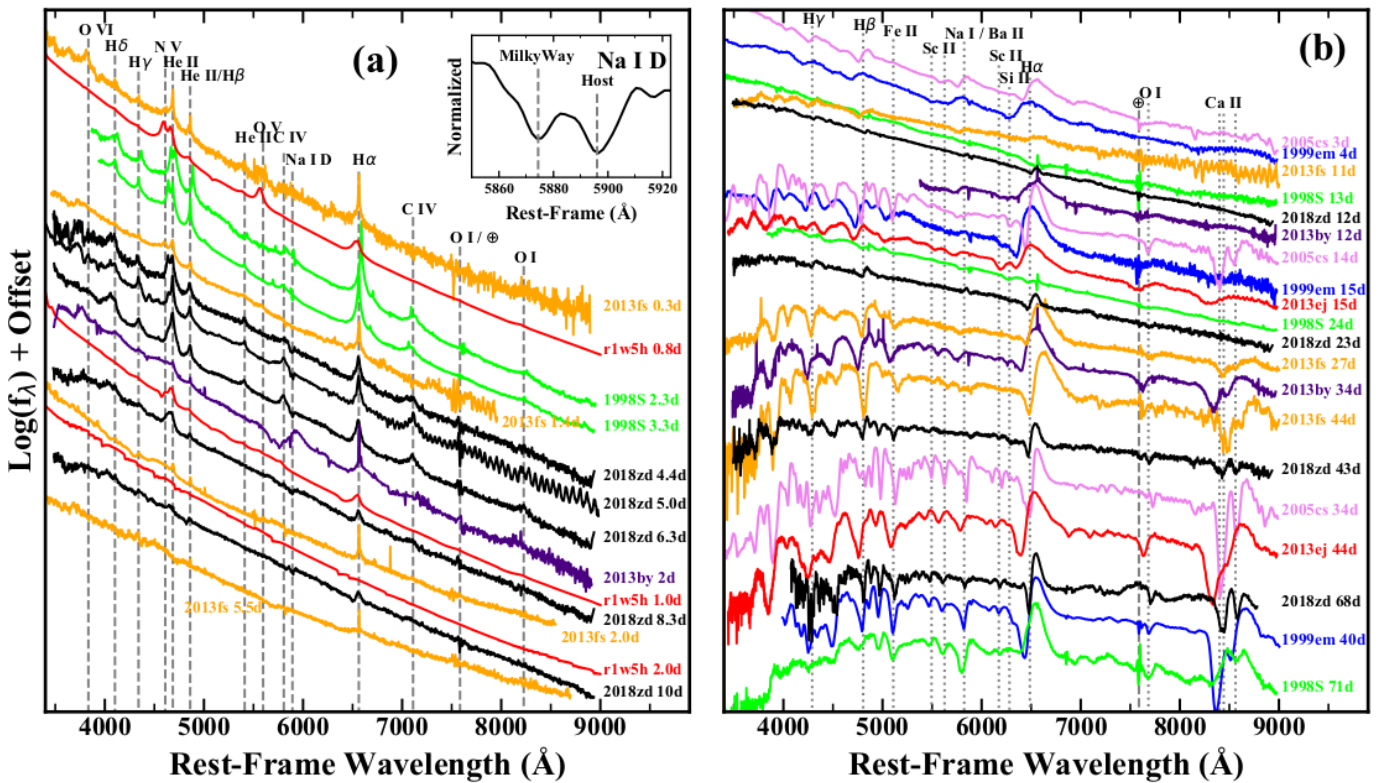
We present extensive observations of SN 2018zd covering the first ~450 d after the explosion. This SN shows a possible shock-breakout signal ~3.6 hr after the explosion in the unfiltered light curve, and prominent flash-ionisation spectral features within the first week. The unusual photospheric temperature rise (rapidly from ~12,000 K to above 18,000 K) within the earliest few days suggests that the ejecta were continuously heated. Both the significant temperature rise and the flash spectral features can be explained with the interaction of the SN ejecta with the massive stellar wind ( $0.18^{+0.05}_{-0.10} M_{\odot}$ ), which accounts for the luminous peak ( $L_{max} = [1.36 \pm 0.63] \times 10^{43} \text{erg/s}$ ) of SN 2018zd. The luminous peak and low expansion velocity ( $v \approx 3300 \text{km/s}$ ) make SN 2018zd to be like a member of the LLEV (luminous SNe II with low expansion velocities) events originated due to circumstellar interaction. The relatively fast post-peak decline allows a classification of SN 2018zd as a transition event morphologically linking SNe IIP and SNe IIL. In the radioactive-decay phase, SN 2018zd experienced a significant flux drop and behaved more like a low-luminosity SN IIP both

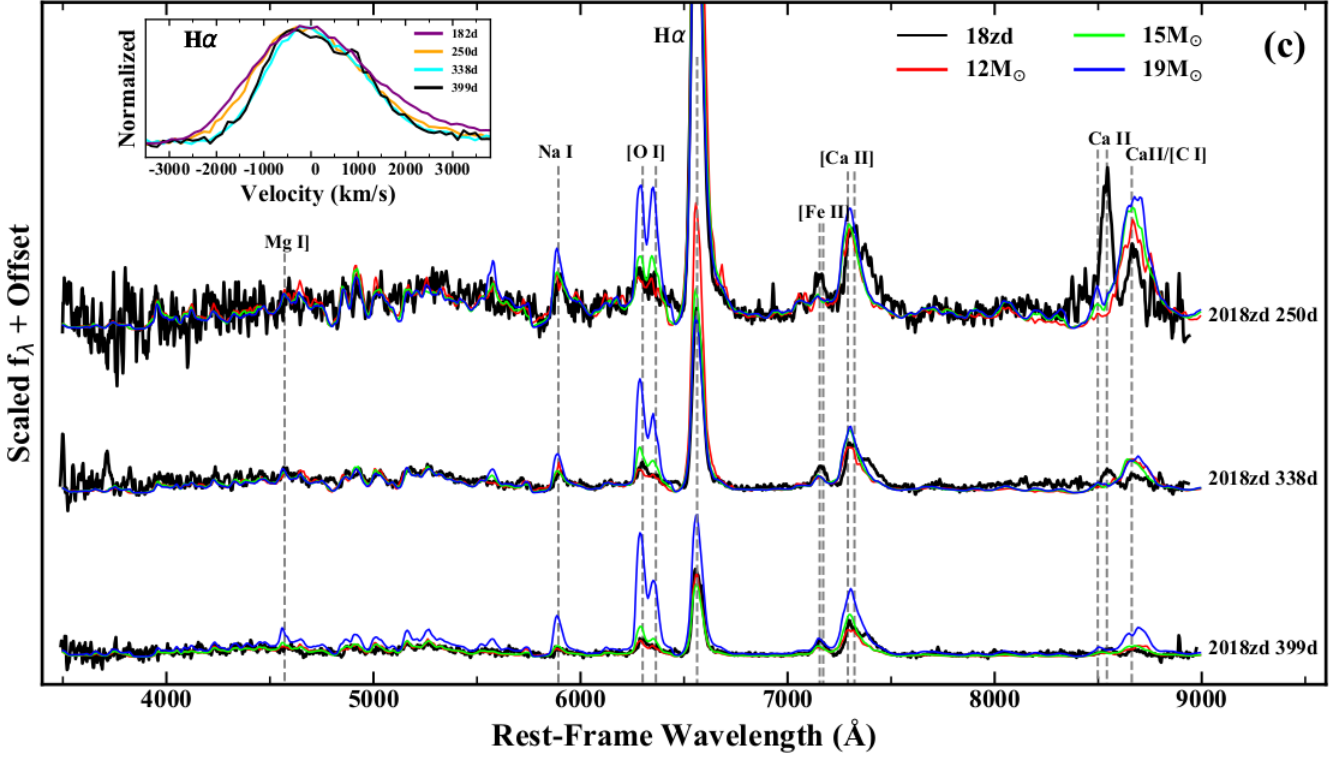
spectroscopically and photometrically. This contrast indicates that circumstellar interaction plays a vital role in modifying the observed light curves of SNe II. Comparing nebular-phase spectra with model predictions suggests that SN 2018zd arose from a star of  $\sim 12 M_{\odot}$ . Given the relatively small amount of  $^{56}\text{Ni}$  ( $0.013 - 0.035 M_{\odot}$ ), the massive stellar wind, and the faint X-ray radiation, the progenitor of SN 2018zd could be a massive asymptotic giant branch star which collapsed owing to electron capture.

- 本文发表了对SN 2018zd的前450天的观测情况。
- SN 2018zd于UT 2018.03.02被报道，随后日本的Takamizawa station的观测给出无滤光波段星等17.8mag。其光谱最早由云南丽江天文台在发现后三小时拍摄。随后的光谱由于具有较窄的谱线被证认为一个IIn型超新星。
- 这个超新星的unfiltered光变曲线在约3.6小时出现了一个可能的shock-breakout（当激波传播到星体表面时会产生明亮的耀发，持续时标通常小于1小时。Garnavich et al. 2016）信号，并在第一周出现了明显的flash-ionisation光谱特征（如氢， $\text{N v } \lambda\lambda 4334, 4641$ ,  $\text{He ii } \lambda 4686$ ,  $\text{He ii } \lambda 4860$ ,  $\text{C iv } \lambda\lambda 5801, 5812$ , 以及  $\text{C iv } \lambda 7110$ 的窄发射线。这些发射线由周围经X射线电离的星风物质发出）。



**Figure 4.** Expanding fireball fit of the early detections of SN 2018zd in the clear band and the  $r$  band, where the first detection by Itagaki cannot be fitted.

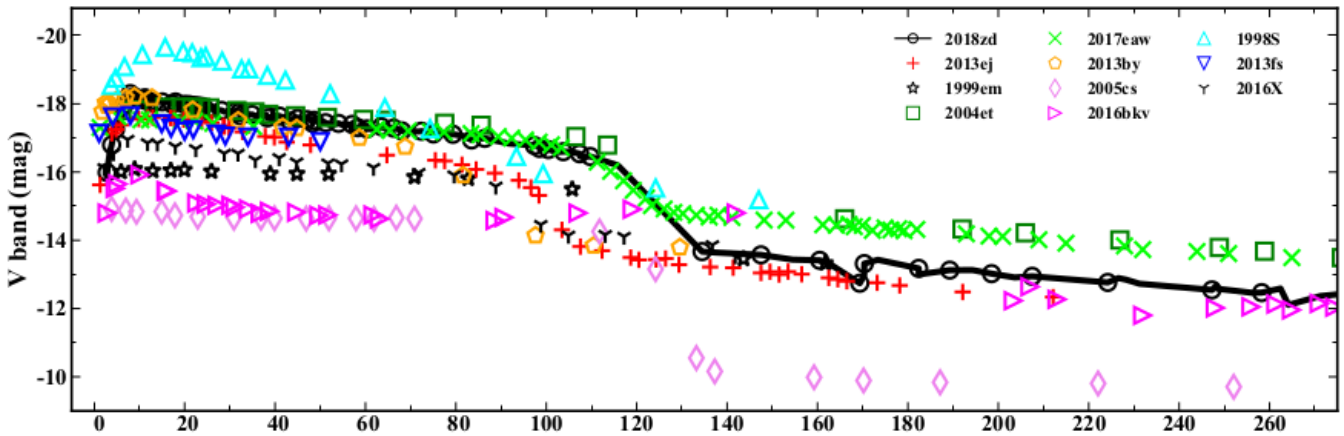
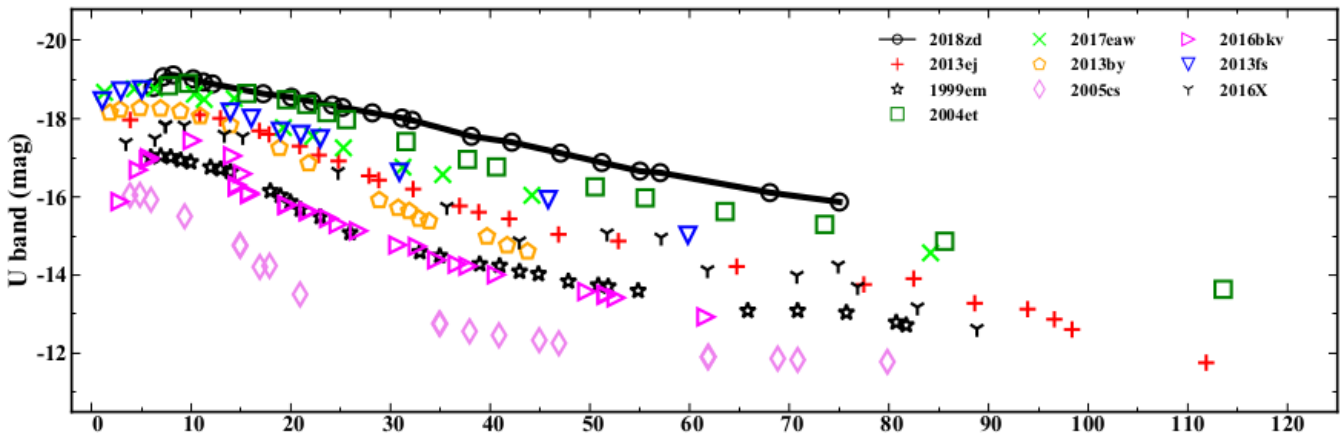
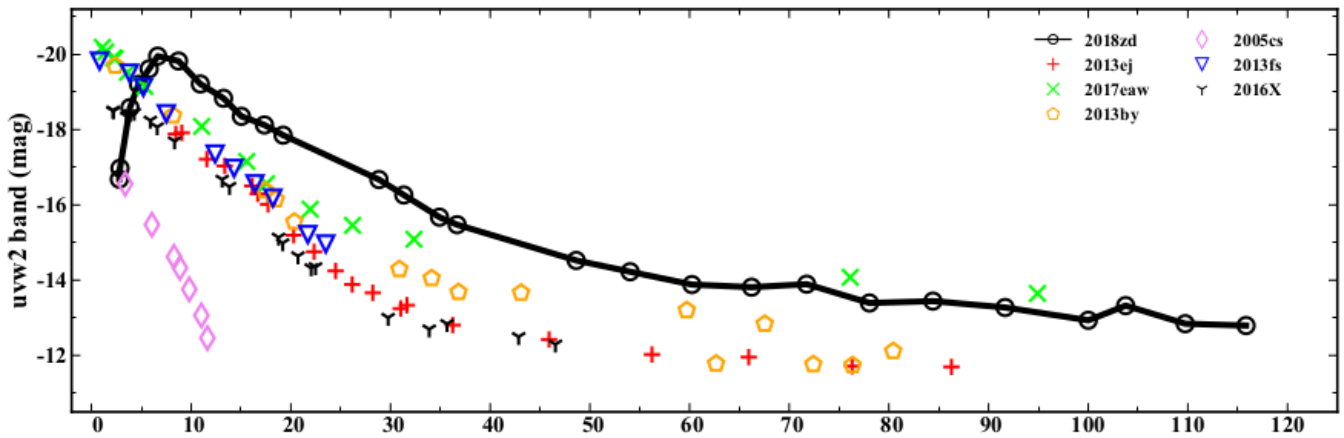




**Figure 8.** Spectral comparison at three phases. (a) Flash-ionisation-phase spectra of SN 2018zd compared with spectra of SN 1998S (Leonard et al. 2000; Fassia et al. 2001; Shivvers et al. 2015), SN 2013by (Valenti et al. 2015), SN 2013fs (Yaron et al. 2017), and model spectra r1w5h of (Dessart, Hillier, & Audit 2017). The inset shows a close-up of the region of Na I D absorption in the spectrum of SN 2018zd at  $t \approx 5$  d. (b) Photospheric-phase spectra of SN 2018zd along with those of SN 1998S, SN 1999em (Hamuy et al. 2001; Leonard et al. 2002), SN 2005cs (Pastorello et al. 2006), SN 2013by, SN 2013ej (Dhungana et al. 2016), and 2013 SN 2013fs. (c) Three nebular-phase spectra of SN 2018zd (at 250 d, 338 d, and 399 d) compared with model spectra corresponding to different progenitor masses (Jerkstrand et al. 2012;  $12 M_{\odot}$  at 250 d, 306 d, and 400 d;  $15 M_{\odot}$  at 250 d, 332 d, and 400 d; and  $19 M_{\odot}$  at 250 d, 332 d, and 369 d). The model spectra are scaled to the distance of SN 2018zd and its  $^{56}\text{Ni}$  mass. The inset shows the velocity distribution of the H $\alpha$  emission of SN 2018zd at  $t = 182$  d, 250 d, 338 d, and 399 d; the instrumental resolution was removed via  $\text{FWHM}_{\text{corr}} = (\text{FWHM}_{\text{obs}}^2 - \text{FWHM}_{\text{inst}}^2)^{1/2}$ , where the instrumental FWHM was measured from the night-sky emission lines. In panels (a) and (c), dashed lines mark spectral features at rest; in panel (b), dotted lines indicate spectral features at  $v = -3500 \text{ km s}^{-1}$ . In panels (a) and (b), residuals from incomplete removal of telluric absorption are marked with an Earth symbol. The host-galaxy redshift and the extinction from the host galaxy and the Milky Way have been removed.

MNRAS **000**, 1–17 (xxxx)

- 其光球层温度在最初的几天里迅速从约12000K 升至约18000K, 显示喷射物被不间断持续地加热。
- 显著的温度上升和flash-ionisation光谱特征都可以用SN 喷射物与大质量星风 ( $0.18^{+0.05}_{-0.10} M_{\odot}$ ) 相互作用来解释, 这也同样能解释其较亮的峰值光度  $L_{max} = [1.36 \pm 0.63] \times 10^{43} \text{ erg/s}$ 。较亮的峰值光度和较低的扩散速度 (expansion velocity  $\sim v \approx 3300 \text{ km/s}$ ) 显示SN 2018zd像是 LLEV (luminous SNe II with low expansion velocities; 起源于星周相互作用 circumstellar interaction) 事件中的一员。
- 根据其相对较快的峰值后衰减, 也可以从形态上把它分类为一个连接IIP (Plateau, 最常见) 型和IIL (Linear) 型超新星的过渡性事件。



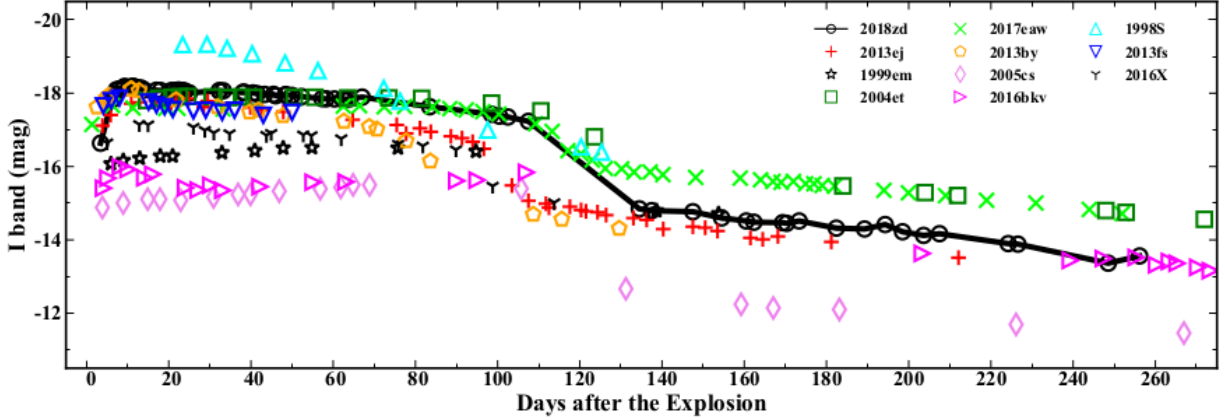


**Figure 5.** Light-curve comparisons (in absolute magnitude) between SN 2018zd with some well-studied SNe II, including the standard SNe IIP 1999em (Hamuy et al. 2001; Leonard et al. 2002; Elmhamdi et al. 2003) and 2004et (Sahu et al. 2006; Misra et al. 2007), the normal SNe IIP 2017ew (Rui et al. 2019; Szalai et al. 2019, and unpublished data collected with LJT and TNT), the fast-declining SNe II 2013ej (Huang et al. 2015; Dhungana et al. 2016; Yuan et al. 2016) and 2013by (Valenti et al. 2015), the low-velocity and low-luminosity SNe IIP 2005cs (Pastorello et al. 2006, 2009), and SNe II showing interaction signatures in their spectra such as SNe 2013fs (Yaron et al. 2017; Bullivant et al. 2018), 2016bkv (Hosseinzadeh et al. 2018; Nakaoka et al. 2018), and 1998S (Leonard et al. 2000; Fassia et al. 2000; Poon et al. 2011).

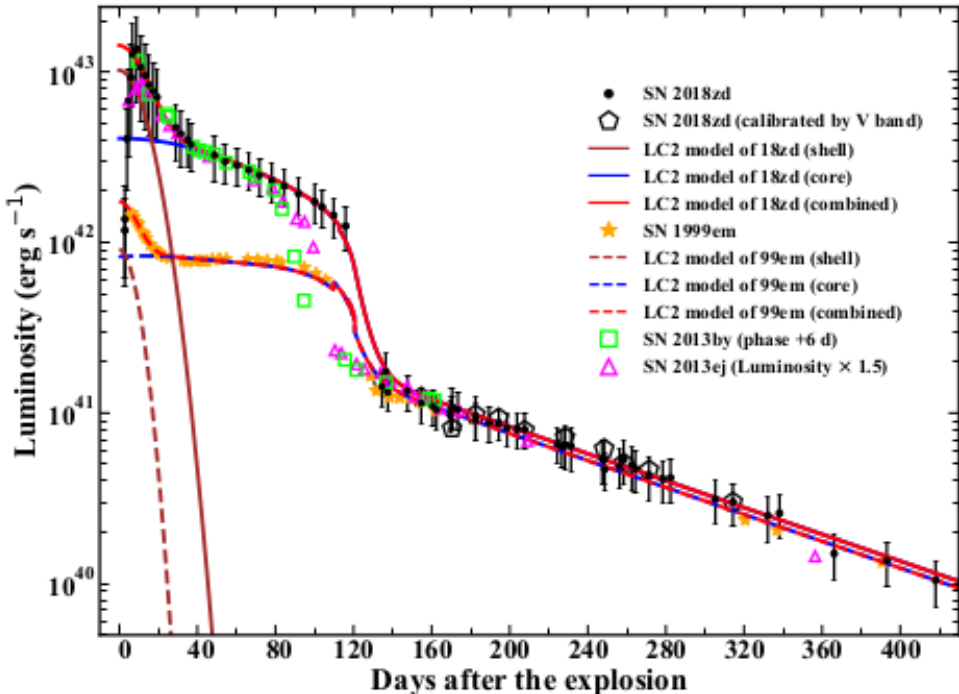


**Figure 10.** Bolometric light curve of SN 2018zd compared with that of SN 1999em, SN 2013by, SN 2013ej and the results of the LC2 model. The error bars include uncertainties in the photometry, extinction, and distance, the last two of which greatly dominate. The LC2 model contains the contribution of the core and the shell. The phase of SN 2013by has been shifted by +6 d corresponding to the archival explosion date (MJD = 56403.5; Valenti et al. 2015). The luminosity of SN 2013ej has been multiplied by 1.5.

- 在radioactively decay的阶段，它出现了显著的流量下降，并且在测光和测谱上均与低光度IIP型SN更类似（如SN 2018zd 68天的光谱与 SN 1999em 43天的光谱相似）。
- 将星云阶段的光谱与模型预测进行比较，说明SN 2018zd前身星质量约为 $12M_{\odot}$ 。考虑到 $^{56}\text{Ni}$ 的量相对较少（ $0.013 - 0.035 M_{\odot}$ ），以及较大质量的星风和较弱的X射线辐射，SN 2018zd的前身星可能是一个因为电子俘获而塌缩的massive asymptotic giant branch star.

## 200730

---

### **Detection of 15 bursts from FRB 180916.J0158+65 with the uGMRT**

type:observation-FRB

comment:作者使用uGMRT对周期为16.35天重复快速射电爆FRB 180916.J0158+65的观测情况，有两次爆发比较明亮，足够进行亚角秒定位

<https://arxiv.org/abs/2007.14404>

#### ► abstract

Authors: Visweshwar Ram Marthi, Tasha Gautam, Dongzi Li et al.

Comments: 5 pages, 4 figures, submitted to MNRAS Letters

We report the findings of a uGMRT observing campaign on FRB 180916.J0158+65, discovered recently to show a 16.35-day periodicity of its active cycle. We observed the source at 550–750 MHz for  $\sim$ 2 hours each during three successive cycles at the peak of its expected active period. We find 0, 12, and 3 bursts respectively, implying a highly variable bursting rate even within the active phase. We consistently detect faint bursts with spectral energies only an order of magnitude higher than the Galactic burst source SGR~1935+2154. The times of arrival of the detected bursts rule out many possible aliased solutions, strengthening the findings of the 16.35-day periodicity. A short-timescale periodicity search returned no highly significant candidates. Two of the beamformer-detected

bursts were bright enough to be clearly detected in the imaging data, achieving sub-arcsecond localization, and proving as a proof-of-concept for FRB imaging with the GMRT. We provide a  $3\sigma$  upper limit of the persistent radio flux density at 650 MHz of 66  $\mu\text{Jy}$  which, combined with the EVN and VLA limits at 1.6~GHz, further constrains any potential radio counterpart. These results demonstrate the power of uGMRT for targeted observations to detect and localize known repeating FRBs.

- 本文报道了作者使用uGMRT对周期为16.35天（活跃期集中在5天的窗口内，CHIME/FRB Collaboration et al., 2020, Nature, 582, 351）重复快速射电爆FRB 180916.J0158+65的观测情况。
- 观测分别在预期活跃阶段的 2020 March 09, 2020 March 24, 以及 2020 June 30进行，观测频段为550–750 MHz，每次时长两小时。这三次分别探测到了0, 12, 3次爆发，表明此FRB在活跃期也具有相当高的变化性。
- 有两次爆发 (beamformer-detected bursts) 比较明亮，足够进行亚角秒定位。

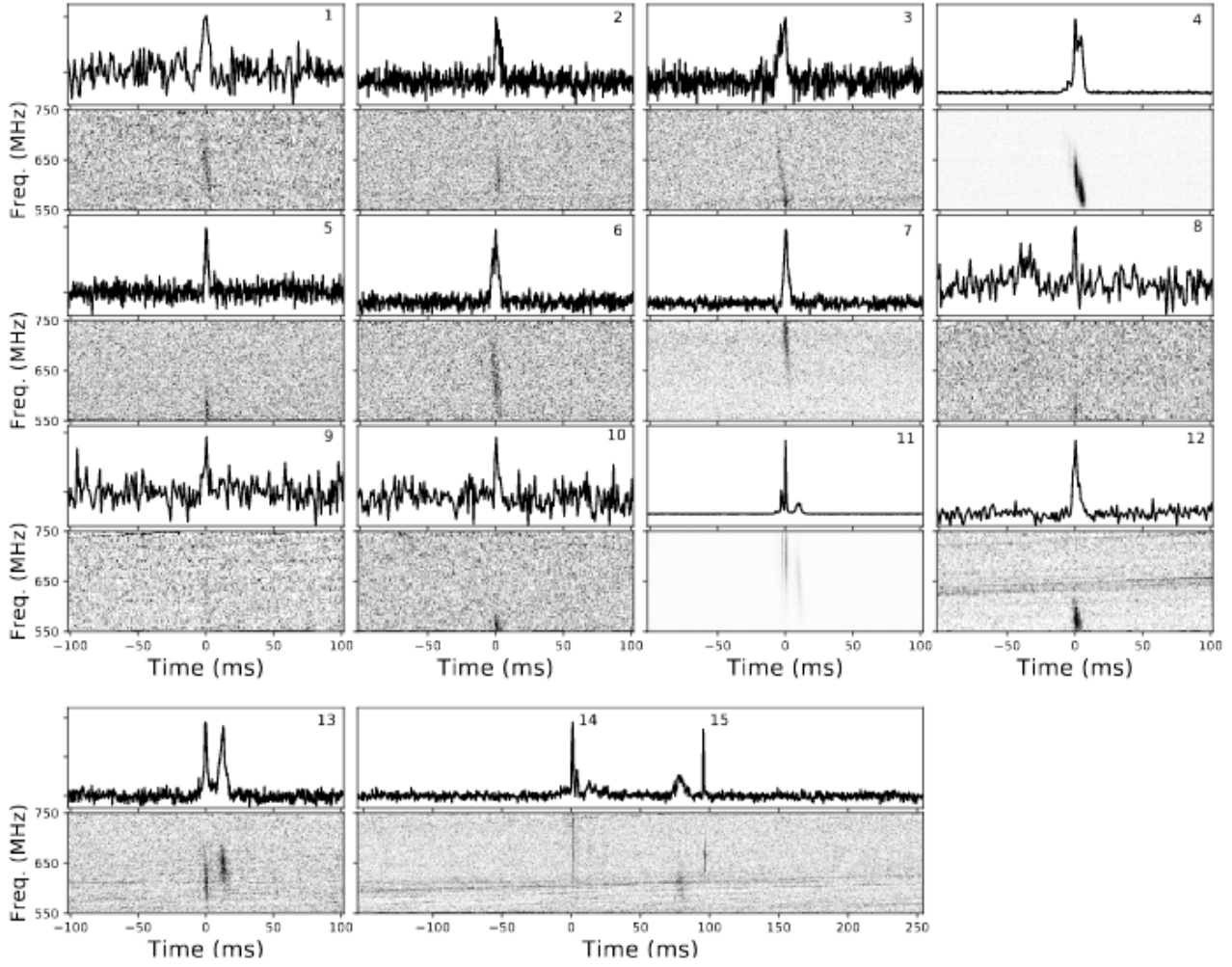


**Figure 1.** Dynamic spectra of all detected bursts, in sequential order. For plotting purposes, frequency was binned by a factor of 16. In low S/N bursts, frequency was binned by an additional factor of two, and the time was binned by a factor of 3 to  $983.04\mu\text{s}$ . The top panels show our detections from March 24, while the bottom row are from June 30, where the final panel is interpreted as at least two separate bursts.

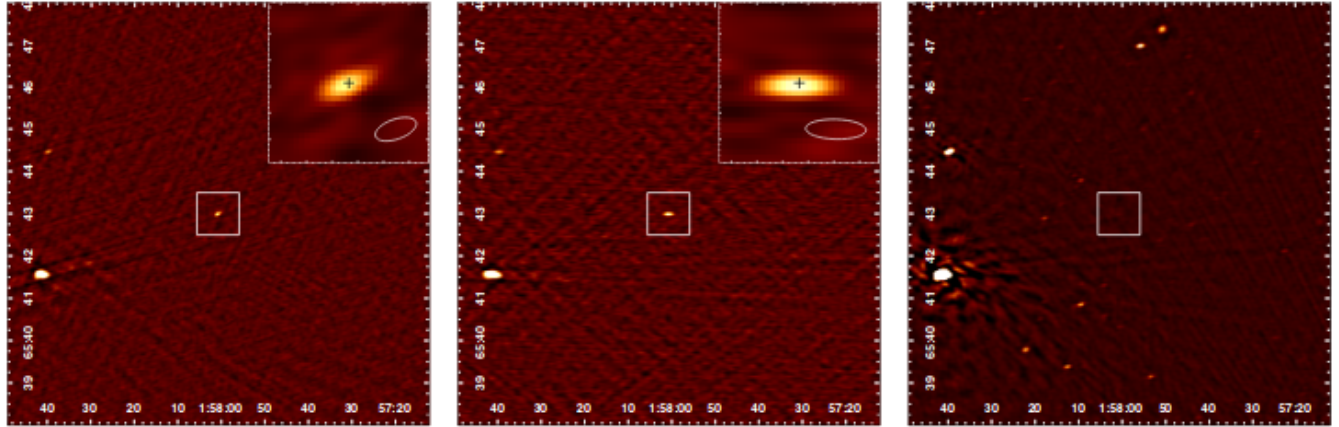


**Figure 4.** Images of  $10' \times 10'$  region centered on the position of FRB 180916J0158+65, which is indicated by  $1' \times 1'$  box. The left (Burst 04) and middle (Burst 11) plots show the detection of single bursts using visibilities from only two (Burst 04) or one (Burst 11) 2.68 sec time samples. The inset of each plot shows the  $1' \times 1'$  region around the burst. The CLEAN beam is shown in the bottom right of each inset and the EVN position is indicated by a black cross. The right plot shows a deep image made using data from the full  $\approx 2$  hr observation of 2020 Mar 24.

# Dust-scattering halo and giant hard X-ray flare from the Supergiant Fast X-ray Transient IGR J16479–4514 investigated with XMM–Newton and INTEGRAL

<https://arxiv.org/abs/2007.15329>

type:observation-Supergiant\_Fast\_Xray\_Transient

comment:本文对IGRJ 16479–4514这个源的XMM–Newton和INTEGRAL观测数据做了分析

## ► abstract

Authors: V. Sguera, A. Tiengo, L. Sidoli, A. J. Bird

Comments: Accepted for publication on The Astrophysical Journal  
(received 20-Apr-2020, accepted 27-Jul-2020)

We report results from the analysis of XMM–Newton and INTEGRAL data of IGR J16479–4514. The unpublished XMM–Newton observation, performed in 2012, occurred during the source eclipse. No point-like X-ray emission was detected from the source, conversely extended X-ray emission was clearly detected up to a size distance compatible with a dust scattering halo produced by the source X-ray emission before being eclipsed by its companion donor star. The diffuse emission of the dust-scattering halo could be observed without any contamination from the central point X-ray source, compared to a previous XMM–Newton observation published in 2008. Our comprehensive analysis of the 2012 unpublished spectrum of the diffuse emission as well as of the 2008 re-analysed spectra extracted from three adjacent time intervals and different extraction regions (optimized for point-like and extended emission) allowed us to clearly disentangle the scattering halo spectrum from the residual point-like emission during the 2008 eclipse. Moreover, the point-like emission detected in 2008 could be separated into two components attributed to the direct emission from the source and to scattering in the stellar wind, respectively. From archival unpublished INTEGRAL data, we identified a very strong ( $3 \times 10^{-8} \text{ erg cm}^{-2} \text{s}^{-1}$ ) and fast (25 minutes duration) flare which was classified as giant hard X-ray flare since the measured peak-luminosity is  $7 \times 10^{37} \text{ erg s}^{-1}$ . Giant X-ray flares from SFXTs are very rare, to date only one has

been reported from a different source. We propose a physical scenario to explain the origin in the case of IGR J16479–4514.

- 本文对IGRJ 16479–4514 (Supergiant Fast X-ray Transient, 是INTEGRAL上天后发现的一种新类别的Supergaint High-Mass X-ray Binaries, 通常是中子星围绕一个早期超巨星旋转的系统。特点之一是具有明亮 $\sim 10^{36} ergs^{-1}$ 且快速—几小时到几天—的X射线暂现行为。这个源最早在2003年由INTEGRAL 发现) 这个源的XMM-Newton 和INTEGRAL观测数据做了分析。
- XMM-Newton在2012年的观测 (unpublished) 发生在这个源的“蚀变”期, 当时的观测没有呈现X射线点源, 相反是一个延展的X射线辐射源 (extended X-ray emission), 尺度上看比较像是在这颗源在被伴星掩盖前发出的X射线辐射被灰尘散射形成的灰尘散射晕 (dust scattering halo) 。

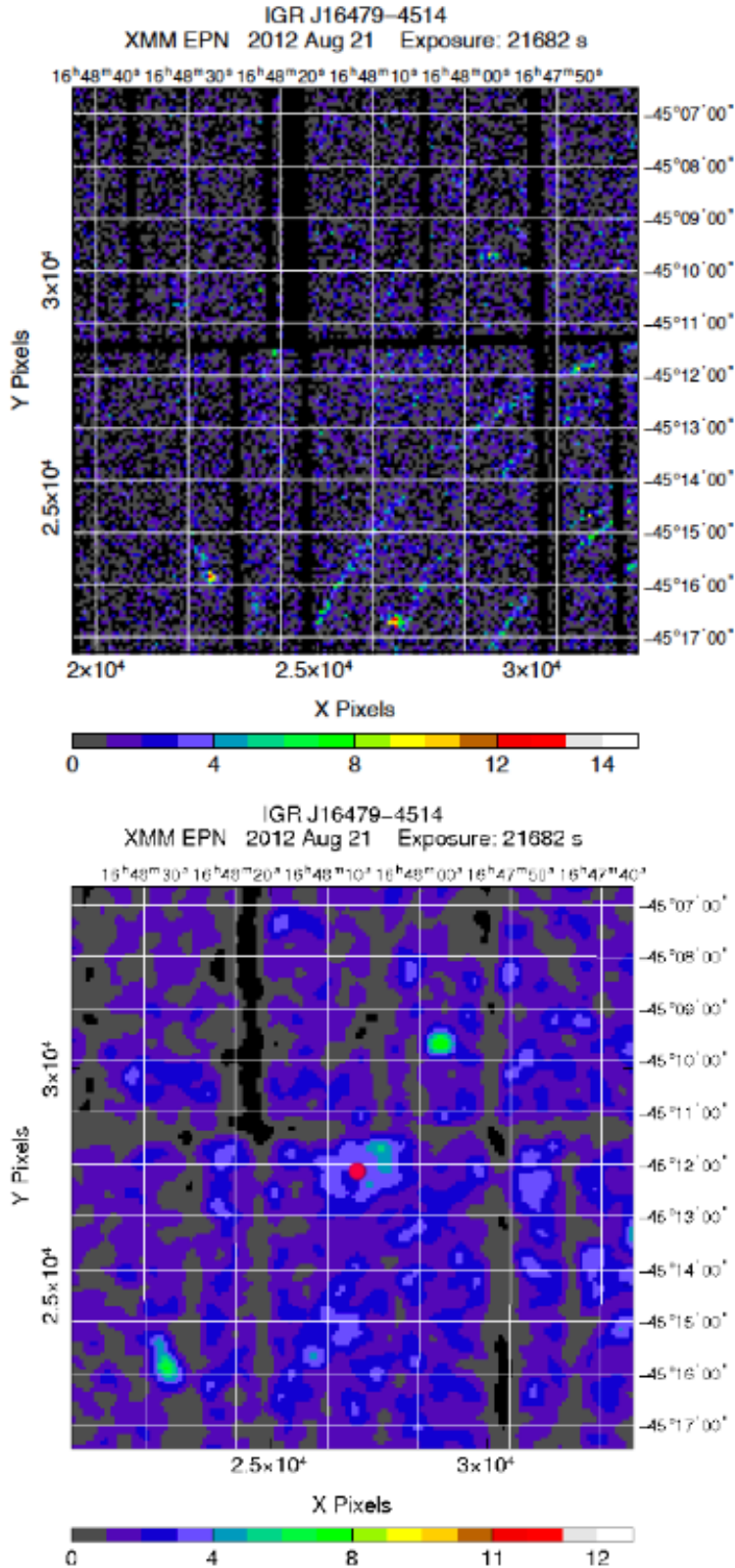


FIG. 1.— IGR J16479–4514 sky position observed by *XMM-Newton*/EPIC pn, in the energy ranges 0.5–10 keV (top panel, close-up view around the target position) and 1–3 keV (bottom panel, where the image was smoothed with a Gaussian with a width  $\sigma=2$  pixels). The small red circle marks the IGR J16479–4514 infrared position (2MASS).

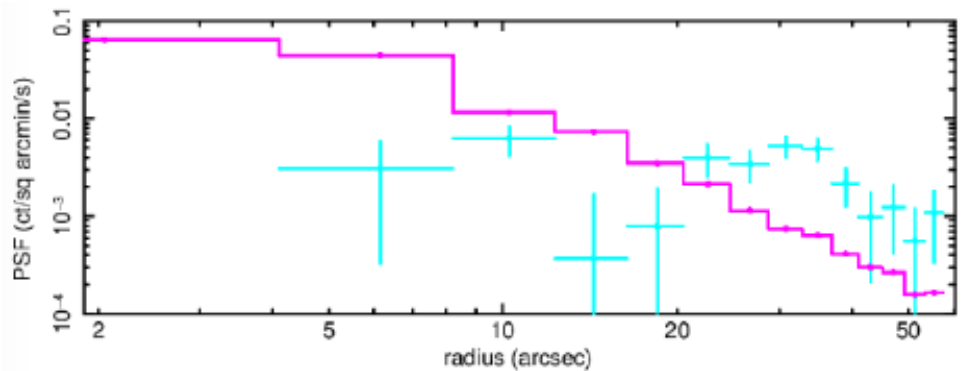


FIG. 2.— Surface brightness profiles of the X-ray emission within  $1'$  from the source 2MASS position, in the energy range 1–3 keV, compared with the EPIC pn point spread function in the same energy range (solid line).

- 对比XMM-Newton 2008年的观测（处于“蚀变”开始期 *eclipse ingress*, 且看到了源），2012年观测到的散射晕的漫发射（*diffuse emission*）基本上没有被X射线源污染。通过详细分析2012年的漫发射光谱和2008年的光谱，可以比较清楚的把散射晕的光谱与2008年“蚀变”期的残留点源辐射区分开来。进一步的，2008年的点源辐射可视作两个成分的组合，一个是来自源的直接辐射，另一个是星风中的散射。

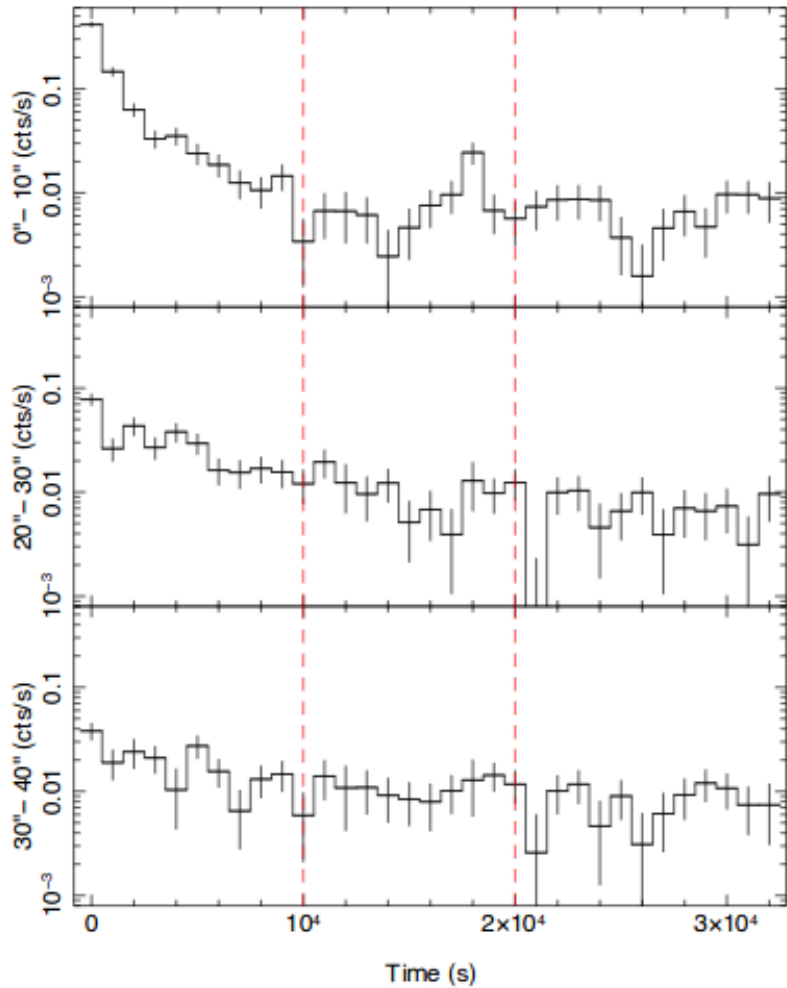


FIG. 3.— EPIC pn background-subtracted light curve of the 2008 observation extracted in the 1.5–5 keV energy band from a circle of 10 arcsec radius (top panel) and two annuli of inner and outer radii of 20 and 30 arcsec (middle panel) and 30 and 40 arcsec (bottom panel), centered at the IGR J16479–4514 position. The bin time is 1000 s and the vertical lines indicate the three time intervals used for spectral analysis (interval 1, 2, 3 as reported in Table 1).

TABLE 1

BEST-FIT PARAMETERS OF *XMM-Newton* SPECTRA WITH THE MODEL REPORTED IN EQUATION 1 ( $\chi^2=164.7$  FOR 176 DEGREES OF FREEDOM). INTERVAL 1, 2 AND 3 CORRESPOND TO THE PN SPECTRA OF THE TIME INTERVALS OF THE 2008 OBSERVATION, AS DEFINED IN FIG. 3, AND OBSERVATION 2 TO THE MOS AND PN SPECTRA OF THE FULL 2012 OBSERVATION.

	POINT SOURCE (10 arcsec)			DIFFUSE EMISSION (20–40 arcsec)			
	Interval 1	Interval 2	Interval 3	Interval 1	Interval 2	Interval 3	Observation 2
$N_{\text{H}}$ ( $10^{22} \text{ cm}^{-2}$ )	$6.6^{+2.5}_{-2.4}{}^{(a)}$	$6.6^{(a)}$	$6.6^{(a)}$	$6.6^{(a)}$	$6.6^{(a)}$	$6.6^{(a)}$	$6.6^{(a)}$
$N_{\text{H1}}$ ( $10^{22} \text{ cm}^{-2}$ )	$33 \pm 5 {}^{(a)}$	—	—	$33 {}^{(a)}$	—	—	—
$\alpha$	$1.2^{+0.2}_{-0.1} {}^{(a)}$	$1.2 {}^{(a)}$	$1.2 {}^{(a)}$	$1.2 {}^{(a)}$	$1.2 {}^{(a)}$	$1.2 {}^{(a)}$	—
$I_1^{(b)}$ ( $10^{-12} \text{ erg cm}^{-2} \text{ s}^{-1}$ )	$39^{+7}_{-6}$	—	—	$3.8^{+1.3}_{-1.2}$	—	—	—
$I_2^{(b)}$ ( $10^{-12} \text{ erg cm}^{-2} \text{ s}^{-1}$ )	$2.8^{+1.5}_{-1.1}$	$0.65^{+0.16}_{-0.14}$	$0.51 \pm 0.12$	$1.2^{+0.5}_{-0.6}$	$0.32^{+0.12}_{-0.14}$	$0.13^{+0.10}_{-0.12}$	—
$\beta$	—	—	—	$4.8^{+1.5}_{-1.3} {}^{(a)}$	$4.8 {}^{(a)}$	$4.8 {}^{(a)}$	$4.8 {}^{(a)}$
$I_{\text{halo}}^{(b)}$ ( $10^{-12} \text{ erg cm}^{-2} \text{ s}^{-1}$ )	—	—	—	$0.37^{+0.50}_{-0.31}$	$0.32^{+0.31}_{-0.17}$	$0.33^{+0.29}_{-0.16}$	$0.10^{+0.08}_{-0.04}$
$E_{\ln 1}$ (keV)	$6.36^{+0.06}_{-0.04} {}^{(a)}$	$6.36 {}^{(a)}$	$6.36 {}^{(a)}$	—	—	—	—
$I_{\ln 1}^{(c)}$ ( $10^{-6} \text{ photons cm}^{-2} \text{ s}^{-1}$ )	$10 \pm 3 {}^{(a)}$	$10 {}^{(a)}$	$10 {}^{(a)}$	—	—	—	—
$E_{\ln 2}$ (keV)	$6.94 \pm 0.09 {}^{(a)}$	$6.94 {}^{(a)}$	$6.94 {}^{(a)}$	—	—	—	—
$I_{\ln 2}^{(c)}$ ( $10^{-6} \text{ photons cm}^{-2} \text{ s}^{-1}$ )	$8 \pm 3 {}^{(a)}$	$8 {}^{(a)}$	$8 {}^{(a)}$	—	—	—	—

(a) Linked parameters

(b) Unabsorbed flux in the 2–10 keV energy band.

(c) Total photon flux in the line.

- 从2008年3月19日INTEGRAL的数据 (archival unpublished) 中, 作者发现有个强烈 ( $3 \times 10^{-8} \text{ erg cm}^{-2} \text{ s}^{-1}$ ) 且快速 (25分钟持续时间) 的耀发, 峰值光度达到  $7 \times 10^{37} \text{ erg s}^{-1}$ , 可归类为giant hard X-ray flare。历史上来自SFXT的giant hard X-ray flare非常罕见, 仅被报道过一次。
- 最后提出了一中物理情景来解释 IGR J16479–4514中的giant hard X-ray flare起源 (较大的吸积质量, 处于具有特殊条件的轨道阶段) 。

## Confirmed width-Eiso and width-Liso relations in GRB: comparison with the Amati and Yonetoku relations

type:theory-GRB

comment:本文主要调查了GRB光谱宽度 (作者按不同的最大流量比值定义了六个光谱宽度) 与 isotropic energy,  $E_{iso}$  和 isotropic peak luminosity,  $L_{iso}$  之间的相关性

<https://arxiv.org/abs/2007.15443>

► abstract

Comments: 25 pages, 25 figures, 8 tables, accepted for publication in The Astrophysical Journal. arXiv admin note: text overlap with [arXiv:1908.04663](https://arxiv.org/abs/1908.04663) by other authors

The well-known Amati and Yonetoku relations in gamma-ray bursts (GRBs) show the strong correlations between the rest-frame  $\nu f_\nu$  spectrum peak energy,  $E_{p,i}$  and the isotropic energy,  $E_{iso}$  as well as isotropic peak luminosity,  $L_{iso}$ . Recently, Peng et al. (2019) showed that the cosmological rest-frame spectral width are also correlated with  $E_{iso}$  as well as  $L_{iso}$ . In this paper, we select a sample including 141 BEST time-integrated F spectra and 145 BEST peak flux P spectra observed by the Konus-Windwith known redshift to recheck the connection between the spectral width and  $E_{iso}$  as well as  $L_{iso}$ . We define six types of absolute spectral widths as the differences between the upper (E2) and lower energy bounds (E1) of the full width at 50%, 75%, 85%, 90%, 95%, 99% maximum of the  $EF_E$  versus  $E$  spectra. It is found that all of the rest-frame absolute spectral widths are strongly positive correlated with  $E_{iso}$  as well as  $L_{iso}$  for the long burst for both the F and P spectra. All of the short bursts are the outliers for width- $E_{iso}$  relation and most of the short bursts are consistent with the long bursts for the width- $L_{iso}$  relation for both F and P spectra. Moreover, all of the location energy,  $E_2$  and  $E_1$ , corresponding to various spectral widths are also positive correlated with  $E_{iso}$  as well as  $L_{iso}$ . We compare all of the relations with the Amati and Yonetoku relations and find the width- $E_{iso}$  and width- $L_{iso}$  relations when the widths are at about 90% maximum of the  $EF_E$  spectra almost overlap with Amati relation and Yonetoku relation, respectively. The correlations of  $E_2 - E_{iso}$ ,  $E_1 - E_{iso}$  and  $E_2 - L_{iso}$ ,  $E_1 - L_{iso}$  when the location energies are at 99% maximum of the  $EF_E$  spectra are very close to the Amati and Yonetoku relations, respectively. Therefore, we confirm the existence of tight width- $E_{iso}$  and width- $L_{iso}$  relations for long bursts. We further show that the spectral shape is indeed related to  $E_{iso}$  and  $L_{iso}$ . The Amati and Yonetoku relations are not necessarily the best relationships to relate the energy to the  $E_{iso}$  and  $L_{iso}$ . They may be the special cases of the width- $E_{iso}$  and width- $L_{iso}$  relations or the energy- $E_{iso}$  and energy- $L_{iso}$  relations.

- 本文主要调查了GRB光谱宽度（作者按不同的最大流量比值定义了六个光谱宽度）与

isotropic energy,  $E_{iso}$  和 isotropic peak luminosity,  $L_{iso}$  之间的相关性。

- 光谱样本包含141个time-integrated光谱 (F光谱) 和145个峰值流量时的光谱 (P光谱)。
- 发现对于长爆，两种光谱都表现出width- $E_{iso}$  和width- $L_{iso}$  较强的相关性，而短爆则大多只表现出width- $L_{iso}$  的相关性。

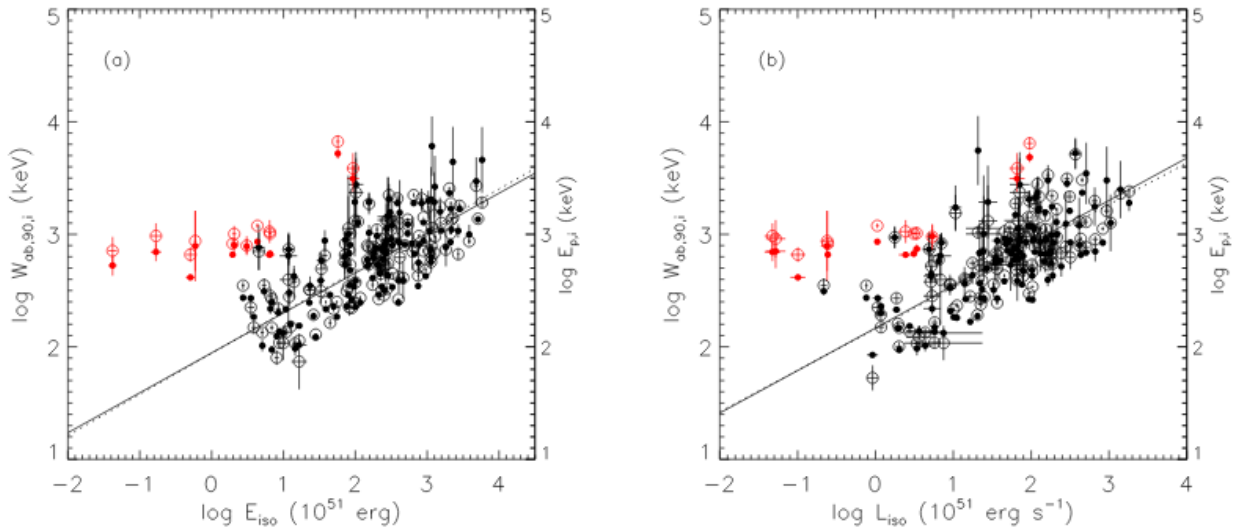


**Figure 10.**  $W_{ab,90,i}$  vs.  $E_{iso}$  for the F spectra (a) and  $W_{ab,90,i}$  vs.  $L_{iso}$  for the P spectra (b), along with the Amati and Yonetoku relations. All the symbols are same as Figure 7.

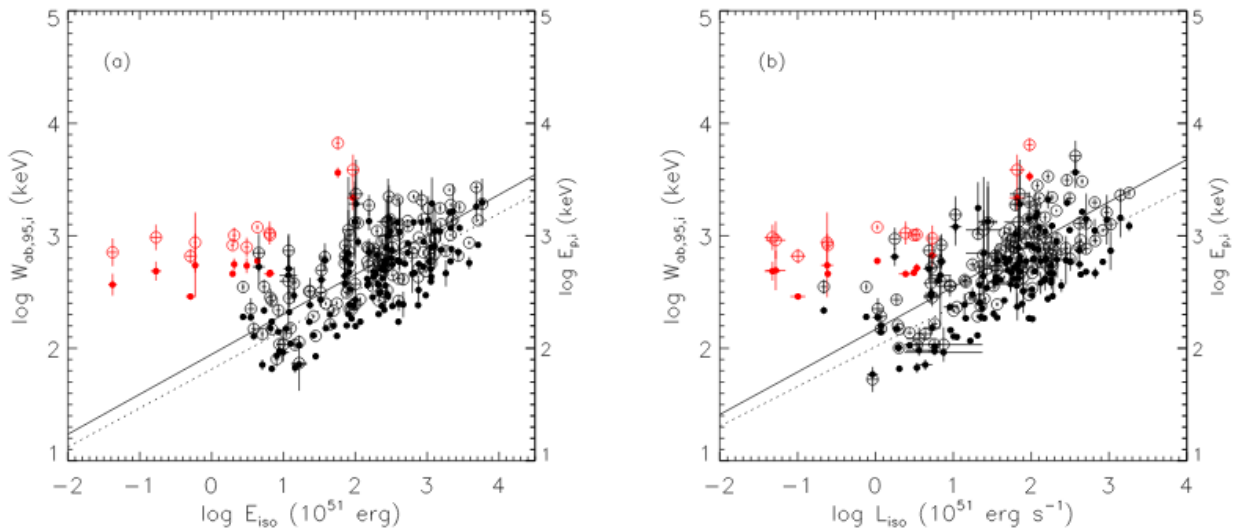


**Figure 11.**  $W_{ab,95,i}$  vs.  $E_{iso}$  for the F spectra (a) and  $W_{ab,95,i}$  vs.  $L_{iso}$  for the P spectra (b), along with the Amati and Yonetoku relations. All the symbols are same as Figure 7.

**Table 4.** Correlation analysis results of six absolute spectral widths in the rest frame and  $E_{iso}$  as well as  $L_{iso}$ .

Correlation	number	$\rho$	$P$	a	b	$\sigma$
-------------	--------	--------	-----	---	---	----------

*Table 4 continued on next page*

**Table 4 (continued)**

Correlation	number	$\rho$	$P$	a	b	$\sigma$
$W_{ab,50,i,F} - E_{iso}$	129	0.80	<0.0001	$0.57 \pm 0.04$	$2.07 \pm 0.09$	$0.30 \pm 0.02$
$W_{ab,75,i,F} - E_{iso}$	129	0.75	<0.0001	$0.42 \pm 0.03$	$2.08 \pm 0.07$	$0.240 \pm 0.02$
$W_{ab,85,i,F} - E_{iso}$	129	0.72	<0.0001	$0.38 \pm 0.03$	$2.02 \pm 0.07$	$0.23 \pm 0.02$
$W_{ab,90,i,F} - E_{iso}$	129	0.71	<0.0001	$0.37 \pm 0.03$	$1.94 \pm 0.07$	$0.23 \pm 0.02$
$W_{ab,95,i,F} - E_{iso}$	129	0.69	<0.0001	$0.35 \pm 0.03$	$1.81 \pm 0.06$	$0.23 \pm 0.02$
$W_{ab,99,i,F} - E_{iso}$	129	0.66	<0.0001	$0.33 \pm 0.03$	$1.48 \pm 0.06$	$0.23 \pm 0.02$
$E_{p,i,F} - E_{iso}$	129	0.69	<0.0001	$0.36 \pm 0.03$	$1.95 \pm 0.07$	$0.23 \pm 0.02$
$W_{ab,50,i,P} - L_{iso}$	133	0.71	<0.0001	$0.55 \pm 0.05$	$2.44 \pm 0.08$	$0.35 \pm 0.03$
$W_{ab,75,i,P} - L_{iso}$	133	0.69	<0.0001	$0.41 \pm 0.04$	$2.35 \pm 0.06$	$0.26 \pm 0.02$
$W_{ab,85,i,P} - L_{iso}$	133	0.68	<0.0001	$0.39 \pm 0.03$	$2.24 \pm 0.06$	$0.25 \pm 0.02$
$W_{ab,90,i,P} - L_{iso}$	133	0.67	<0.0001	$0.37 \pm 0.03$	$2.16 \pm 0.06$	$0.25 \pm 0.02$
$W_{ab,95,i,P} - L_{iso}$	133	0.65	<0.0001	$0.35 \pm 0.03$	$2.01 \pm 0.06$	$0.25 \pm 0.02$
$W_{ab,99,i,P} - L_{iso}$	133	0.64	<0.0001	$0.34 \pm 0.03$	$1.67 \pm 0.05$	$0.25 \pm 0.02$
$E_{p,i,P} - L_{iso}$	133	0.69	<0.0001	$0.38 \pm 0.03$	$2.17 \pm 0.05$	$0.24 \pm 0.02$

NOTE—The F and P correspond to the F spectra and P spectra, respectively.

- 另外还讨论了作为宽度上下界的 $E_2, E_1$ 与分别与 $E_{iso}$ 和 $L_{iso}$ 的相关性，发现宽度为最大值99%时，这些关系与Amati and Yonetoku relations比较接近。

# Searching for Electromagnetic Counterparts to Gravitational-wave Merger Events with the Prototype Gravitational-wave Optical Transient Observer (GOTO-4)

<https://arxiv.org/abs/2004.00025v2>

type:observation-GW

comment:本文报道了使用GOTO-4（4指的是4个望远镜，GOTO计划会建造更多望远镜）对LVC 03上半期中的29个引力波事件进行的光学跟踪观测结果，这些观测没有发现靠谱的电磁对应体

## ► abstract

We report the results of optical follow-up observations of 29 gravitational-wave triggers during the first half of the LIGO-Virgo Collaboration (LVC) 03 run with the Gravitational-wave Optical Transient Observer (GOTO) in its prototype 4-telescope configuration (GOTO-4). While no viable electromagnetic counterpart candidate was identified, we estimate our 3D (volumetric) coverage using test light curves of on- and off-axis gamma-ray bursts and kilonovae. In cases where the source region was observable immediately, GOTO-4 was able to respond to a GW alert in less than a minute. The average time of first observation was 8.79 hours after receiving an alert (9.90 hours after trigger). A mean of 732.3 square degrees were tiled per event, representing on average 45.3 per cent of the LVC probability map, or 70.3 per cent of the observable probability. This coverage will further improve as the facility scales up alongside the localisation performance of the evolving gravitational-wave detector network. Even in its 4-telescope prototype configuration, GOTO is capable of detecting AT2017gfo-like kilonovae beyond 200Mpc in favourable observing conditions. We cannot currently place meaningful electromagnetic limits on the population of distant ( $\hat{D}_L=1.3$  Gpc) binary black hole mergers because our test models are too faint to recover at this distance. However, as GOTO is upgraded towards its full 32-telescope, 2 node (La Palma & Australia) configuration, it is expected to be sufficiently sensitive to cover the predicted 04 binary neutron star merger volume, and will be able to respond to both northern and

southern triggers.

- 本文报道了使用GOTO-4（4指的是4个望远镜，GOTO计划会建造更多望远镜）对LVC 03上半期中的29个引力波事件进行的光学跟踪观测结果。

Event	Distance Mpc	$\sigma_{\text{dist}}$ $\pm \text{Mpc}$	Classification Probability				FAR (year $^{-1}$ )	Announcement GCN
			PBBH %	PNSBH %	PBNS %	PMassGap %		
S190408an	1473	358	>99	0	0	0	$8.86 \times 10^{-11}$	24096
S190412m	812	194	100	0	0	0	$5.30 \times 10^{-20}$	24098
S190421ar	1628	535	97	0	0	0	0.47	24141
S190425z	156	41	0	0	>99	0	$1.43 \times 10^{-5}$	24168
S190426c*	377	100	0	6	24	12	0.61	24237
S190510g	227	92	0	0	42	0	0.28	24442
S190512at	1388	322	99	0	0	0	0.06	24503
S190513bm	1987	501	94	<1	0	5	$1.18 \times 10^{-5}$	24522
S190517h	2950	1038	98	<1	<1	2	0.07	24570
S190519bj	3154	791	96	0	0	0	0.18	24598
S190521g	3931	953	97	0	0	0	0.12	24621
S190521r	1136	279	>99	0	0	0	0.01	24632
S190630ag	1059	307	94	<1	0	5	$4.54 \times 10^{-6}$	24922
S190706ai	5263	1402	99	0	0	0	0.06	24998
S190707q	781	211	>99	0	0	0	$1.66 \times 10^{-4}$	25012
S190718y	227	165	0	0	2	0	1.15	25087
S190720a	869	283	99	0	0	0	0.12	25115
S190727h	2839	655	92	<1	0	3	$4.35 \times 10^{-3}$	25164
S190728q	874	171	34	14	0	52	$7.98 \times 10^{-16}$	25187
S190814bv	267	52	0	>99	0	>1	$6.40 \times 10^{-26}$	25324
S190828j	1803	423	>99	0	0	0	$2.67 \times 10^{-14}$	25497
S190828l	1609	426	99	0	0	0	$1.46 \times 10^{-3}$	25503
S190901ap	242	81	0	0	86	14	0.22	25606
S190910d	632	186	0	98	0	0	0.12	25695
S190915ak	1584	381	>99	0	0	0	0.03	25753
S190923y	438	113	0	68	0	0	1.51	25814
S190924h	548	112	0	0	0	99	$2.82 \times 10^{-11}$	25829
S190930s	709	191	0	0	0	95	0.09	25871
S190930t	108	38	0	74	0	0	0.49	25876

**Table 1.** The sample of LVC superevents that were followed up by GOTO. The distance and  $\sigma_{\text{dist}}$  columns represent the posterior mean and standard deviation of the distance to the source, marginalised over the whole sky (Singer et al. 2016). The classification probabilities and False Alarm Rates (FAR) are taken from GraceDB. Note that “missing” probability (i.e. cases where the given probabilities do not sum to 100 per cent) will have been assigned to the “terrestrial” (noise) category. \*Under the assumption that this source is astrophysical in origin, the classification probability becomes NSBH 12 per cent: MassGap 5 per cent: BNS 3 per cent (Ligo Scientific Collaboration & VIRGO Collaboration 2019f).

- 这些观测没有发现靠谱的电磁对应体，作者使用正轴/偏轴的GRB以及千新星的测试光变曲线 (test light curve) 对他们的体积覆盖 (3D/volumetric coverage) 情况进行了估计。（即用模拟的光变曲线来检测GOTO-4的覆盖能力，but how? ?）
- 情况允许的条件 (in cases of well-timed events that fell in unconstrained tiles, 就是在晚间并且能看见) 下，GOTO-4可以在小于1分钟内对GW警报作出反应。平均下来是在GW警报后8.79小时 (trigger后9.90小时) 开始进行第一次反应观测。
- 平均每次事件会对732.3平方度 (单个最高可达2667平方度) 的天区进行划分观测，对应LVC 45.3%的概率天区，或者70.3%的可观测概率天区。随着引力波探测器定位本领的进步，这些覆盖率将会进一步提高。
- 即使目前GOTO只部署了4架望远镜 (组合视场约19平方度，位于La Palma, Spain)，理想条件下也有能力在200Mpc以上的距离观测到AT2017gfo类似的千新星 (理论预期，实际上在这29个事件中的测试得到的平均距离是126Mpc)。不过现在还不能给~1.3Gpc

的双黑洞并合事件定一个电磁上限 (electromagnetic limits ) , 因为测试用的模型不够亮, 不足以覆盖如此远的距离 (正文: However, we find that due to their distance, it is not possible to place model-constraining limits on EM emission from the distant ( $> 250$  Mpc) population of BBH mergers detected by the LVC unless they house on-axis gamma-ray bursts) 。

- 尽管如此, 等将来GOTO部署了全部2个节点 (La Palma & Australia, 每个节点的视场约75平方度) 的32架望远镜, 理论上就有足够的灵敏度去覆盖04的双中子星并合事件 (binary neutron star volume) , 并且对南半球和北半球的触发均能作出反应。

- DATA SAMPLE

- Data Collection with GOTO

- GOTO sentinel (Dyer et al. 2018)自动获取LVC的probability map 后会根据地图给出观测曝光计划;
    - 观测天区的划分是固定的, 拍摄后的图像将与天区以前的模板图像进行对比来找暂现源;
    - 观测计划会随LVC发布的天区图更新;
    - 对于首次反应干测, GOTO使用其较宽的L波段 (3750 – 7000 Å) 激光片, 大约相当于其B, G, R波段的综合, 也相当于SDSS g 和 r 波段的综合;
    - 默认策略是每个tile至少观测两次, 每次3 x 60s曝光。这些图像经过median 叠加形成science图像;
    - 对于BNS事件, 观测会在数天内重复进行。

- Image Processing and Data Mining

- 自动下载图像到处理队列, 将处理后结果录入PostgreSQL数据库
    - 处理过程包括bias subtraction, dark subtraction. flat-field correction, overscan correction and trimming。接着使用 Astrometry.net加载wcs等信息 (astrometric solution) , 使用APASS V波段或者PS1 g波段的大量参考星stars作为对比来确定测光0点。
    - 将图像median叠加后, 如果有模板图像, 则是用HOTPANTS进行图像相减。
    - 通过一套算法去证认相减图像上的features, 得分低的再经过人工筛选; 得分高的就将源及相应的信息放到浏览器上供人检查。这一整套流程大概需要10到20分钟完成。
    - 对一个引力波事件跟踪结束后 (after a campaign) , 会用脚本把所有与此事件的观测数据信息提取出来, 评估跟踪观测的表现。 (For the purpose of this paper, the data are mined after a campaign has been completed using a script which pulls all observations

linked to each event. The observations are analysed and their meta-data is taken to assess follow-up performance.)

- Test Sources

- 正轴GRB余辉
- 偏轴GRB余辉
- 代表类千新星演化的Bazin function (Bazin et al. 2011), 以AT2017gfo的数据为基础得到的拟合光变曲线
- Constant source  $m_L = 19$ , 用于检查GOT0-4对于相对亮且稳定的源的观测能力

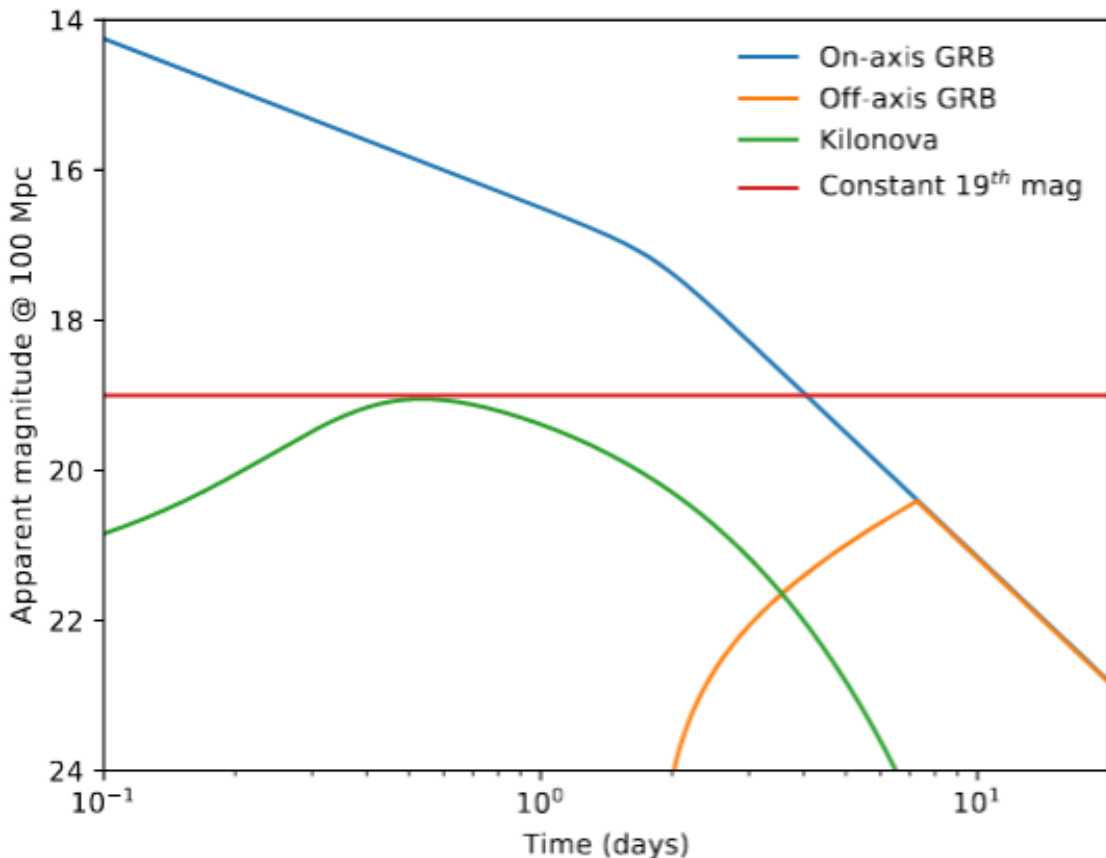


**Figure 1.** Light curves of our test sources at an assumed distance of 100 Mpc.

- METHOD

- 拍摄的时候，每个单位望远镜和每个tile之间都存在一定的重叠，以更完整的覆盖目标天区。
- 平均来说，在一次GW事件跟踪观测中，GOT0-4会对每个LVC skymap pixel重复观测4.8次（计划上的重复故观测加上重叠部分）。

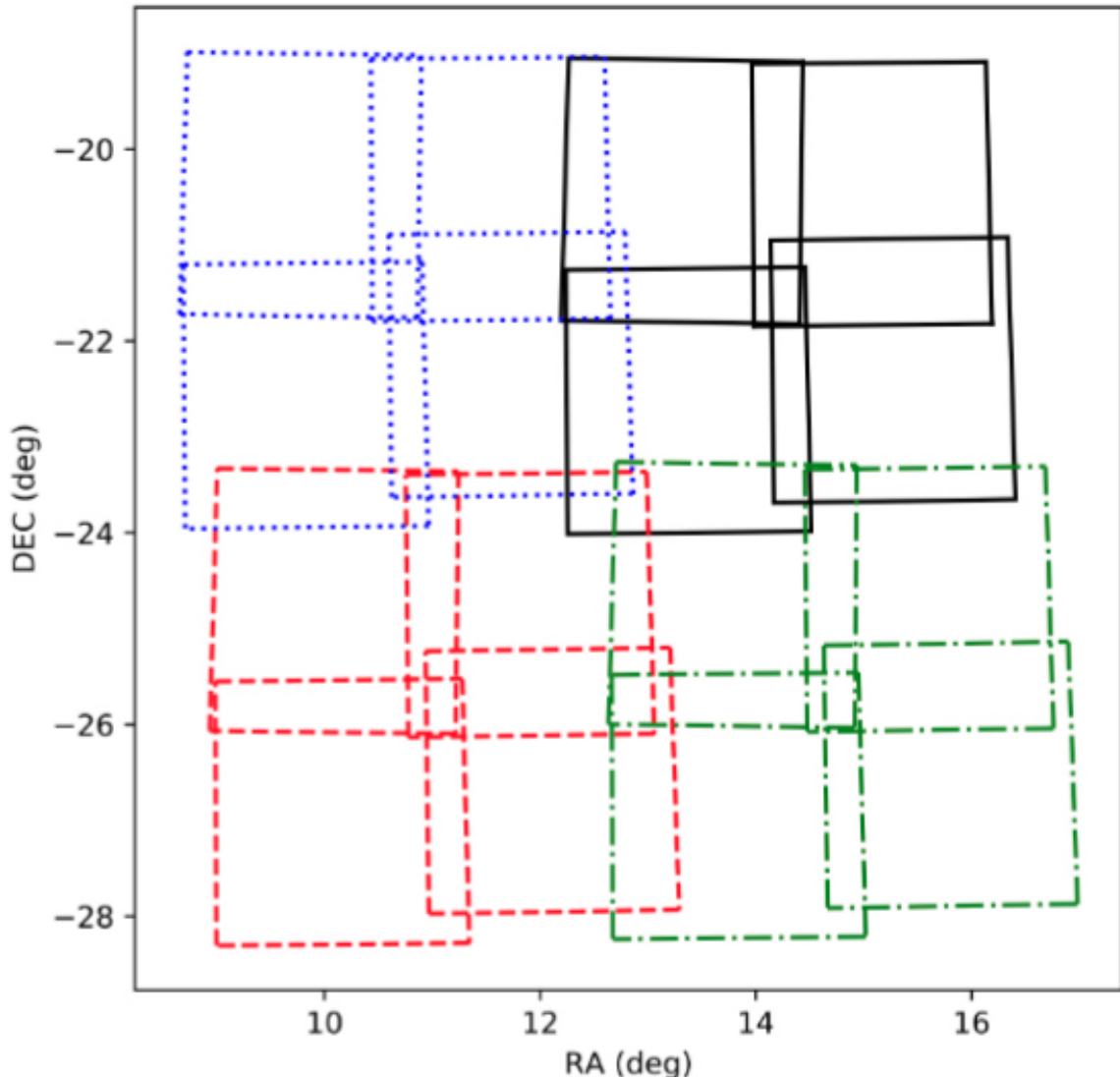


**Figure 2.** Four example GOTO-4 tiles (blue, black, green, red), each of which is comprised of 4 UT snapshots. There is significant overlap in observation both from overlapping tiles and from overlapping UT fields within a given tile. These effects must be accounted for to avoid “double-counting” the covered probability.

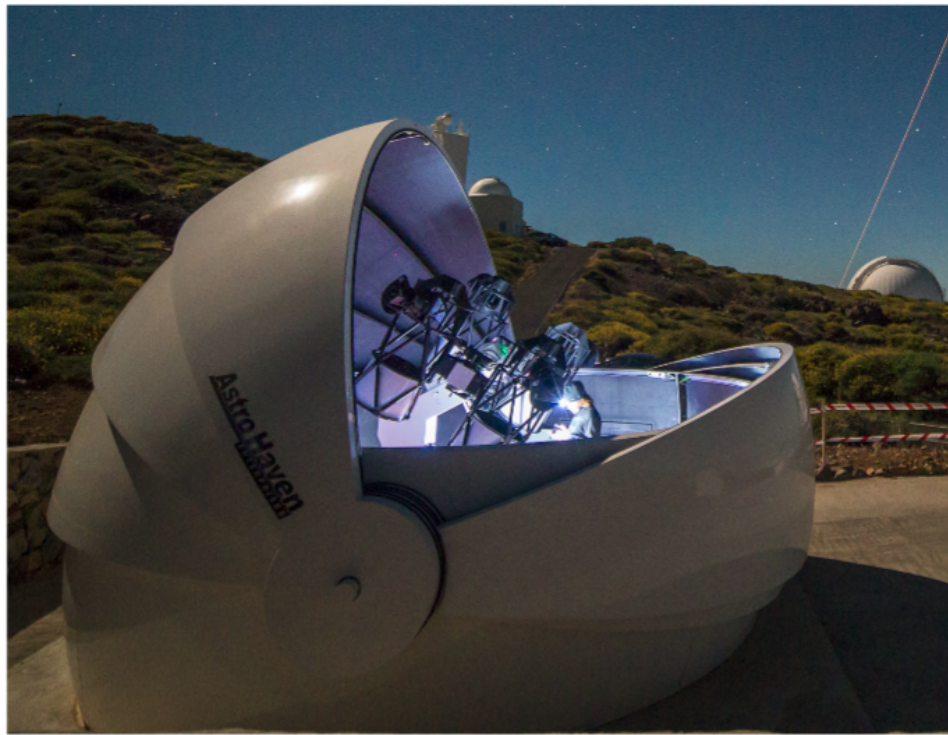


Figure 1. The GOTO prototype instrument on La Palma, with four of the eventual eight unit telescopes.

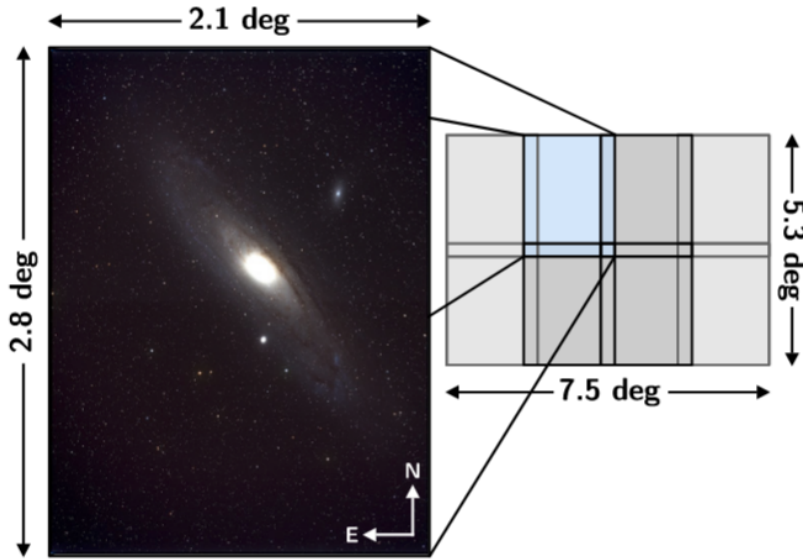


Figure 2. A single commissioning image of M31, showing the wide field of view of each unit telescope. The full 8 unit telescope array will cover an area of approximately 40 square degrees, which forms a single survey tile.

### ◦ Volumetric Coverage

- 将测试模型的实际观测对应时间段的星等（经过银河系消光修正）与观测图像的极限星等相比，来估计最远能观测的距离（即在此距离上，修正的模型星等等于对应真实观测图像的 $5\sigma$ 极限星等）。
- Finally, LVC probability map pixels are sorted into groups of equal observable horizon, where their probability density functions are summed (cf. Singer et al. 2016), and the combined probability density function of each

group is integrated out to their shared horizon. Our full volumetric probability coverage is then the sum of all of the groups.

## • RESULTS & DISCUSSION

- 平均每次事件会对732.3平方度（单个最高可达2667平方度）的天区进行划分观测，对应LVC 45.3%的概率天区，或者70.3%的可观测概率天区。29次测中，有15次覆盖面积在500平方度以上，6次覆盖面积在1000平方度以上。
- 对于双黑洞事件，目前的仪器还无法去探测平均距离1.3Gpc的BBH事件。为了给BBH事件一个大约的辐射上限，作者选取那些反应时间在1天之内且观测条件良好的BBH跟踪观测各自上限的平均，结果大约是 $5\sigma M_L > \sim 19$ 。
- 对于正轴GRB，GOTO-4可以覆盖平均约10%的总概率体积。
- 目前GOTO-4的观测策略并不适合于搜寻偏轴GRB，不仅因为它们亮度偏低，还因为它们到达峰值光度通常在比较晚之后，而GOTO的观测更多集中于trigger后的2到3天。所以可以调整策略，在5到10天后重新搜寻候选天区，以更好限制观测偏轴GRB的可能性。

Event	Response Time		2D Coverage			3D Coverage				KN Range		
	$\delta t_{\text{trig}}$ (hours)	$\delta t_{\text{alert}}$ (hours)	Area (deg $^2$ )	pA (%)	pA <sub>vis</sub> (%)	pV <sub>basin</sub> (%)	pV <sub>GRB</sub> (%)	pV <sub>off-axis</sub> (%)	pV <sub>c19</sub> (%)	D <sub>90</sub> (Mpc)	D <sub>50</sub> (Mpc)	D <sub>0</sub> (Mpc)
S190408an <sup>†</sup>	11.4	10.8	156.1	20.2	23.8	$1.20 \times 10^{-5}$	$1.47 \times 10^{-2}$	$2.82 \times 10^{-7}$	$3.22 \times 10^{-5}$	31	70	135
S190412m <sup>†</sup>	15.0	14.0	295.2	94.4	94.7	$8.68 \times 10^{-3}$	3.48	0	$1.07 \times 10^{-2}$	107	117	151
S190421ar	48.3	29.1	114.3	8.88	36.6	$4.92 \times 10^{-5}$	$3.97 \times 10^{-3}$	$3.89 \times 10^{-7}$	$3.49 \times 10^{-4}$	57	61	66
S190425z	12.4	9.50	2667.1	22.0	38.1	5.90	20.6	$2.57 \times 10^{-3}$	8.10	46	134	227
S190426c	5.30	5.00	772.7	54.1	70.2	$1.10 \times 10^{-2}$	8.98	0	$1.42 \times 10^{-2}$	4	44	136
S190510g	1.42	0.40	116.1	0.21	0.55	$2.06 \times 10^{-3}$	0.21	0	$3.60 \times 10^{-2}$	48	55	57
S190512at	2.78	2.50	315.1	87.1	92.4	$8.52 \times 10^{-5}$	0.37	0	$1.26 \times 10^{-4}$	22	60	154
S190513bm <sup>†</sup>	0.55	0.05	116.2	28.5	76.3	$1.35 \times 10^{-5}$	0.59	0	$2.51 \times 10^{-5}$	56	83	120
S190517h <sup>†</sup>	15.9	15.2	112.7	14.8	51.6	$1.40 \times 10^{-6}$	$1.25 \times 10^{-4}$	0	$1.62 \times 10^{-6}$	49	67	84
S190519bj <sup>†</sup>	5.35	4.35	664.8	84.7	85.3	$2.41 \times 10^{-6}$	$9.55 \times 10^{-4}$	0	$3.64 \times 10^{-6}$	43	69	161
S190521g	0.13	0.05	393.2	43.7	86.7	$8.30 \times 10^{-6}$	$7.57 \times 10^{-2}$	0	$1.11 \times 10^{-5}$	94	107	126
S190521lr <sup>†</sup>	15.2	15.1	720.7	91.9	92.9	$3.85 \times 10^{-6}$	$1.17 \times 10^{-3}$	0	$7.32 \times 10^{-6}$	9	51	93
S190630ag	2.40	2.40	1170.3	60.9	79.5	$1.33 \times 10^{-3}$	19.0	$1.66 \times 10^{-7}$	$3.09 \times 10^{-3}$	71	112	150
S190706ai	0.33	0.03	543.9	36.7	48.5	$8.03 \times 10^{-6}$	1.07	$1.67 \times 10^{-8}$	$2.86 \times 10^{-5}$	55	94	168
S190707q	12.4	11.7	722.9	34.4	59.3	$2.06 \times 10^{-5}$	$2.77 \times 10^{-2}$	0	$2.54 \times 10^{-5}$	18	53	122
S190718y <sup>†</sup>	6.58	6.10	242.5	61.2	72.9	1.12	28.9	$1.54 \times 10^{-2}$	2.45	10	27	90
S190720a	0.08	0.04	1358.3	62.1	73.3	$1.89 \times 10^{-4}$	9.51	$7.67 \times 10^{-7}$	$5.45 \times 10^{-4}$	42	54	163
S190727h	15.0	14.9	714.7	42.3	93.5	$5.72 \times 10^{-7}$	$6.03 \times 10^{-5}$	0	$1.43 \times 10^{-6}$	52	66	140
S190728q	14.8	14.5	146.9	89.5	94.0	$5.55 \times 10^{-4}$	1.03	0	$8.62 \times 10^{-4}$	114	124	139
S190814bv	1.83	1.50	717.9	94.1	99.1	$1.23 \times 10^{-2}$	89.6	$2.33 \times 10^{-6}$	$2.12 \times 10^{-2}$	55	61	81
S190828j	16.1	15.8	442.2	9.11	81.6	$1.01 \times 10^{-5}$	$2.30 \times 10^{-3}$	$6.45 \times 10^{-8}$	$1.27 \times 10^{-5}$	34	105	149
S190828l	16.9	16.5	453.6	1.94	50.5	$5.60 \times 10^{-5}$	$9.20 \times 10^{-3}$	$4.66 \times 10^{-7}$	$7.34 \times 10^{-5}$	127	138	154
S190901ap	0.12	0.04	2523.5	38.3	45.3	0.34	30.2	$8.40 \times 10^{-4}$	1.16	62	88	144
S190910d	0.13	0.03	1675.0	41.2	85.1	$5.43 \times 10^{-3}$	17.6	0	$1.87 \times 10^{-2}$	28	69	148
S190915ak	29.9	29.8	18.2	0.08	0.08	$3.63 \times 10^{-11}$	$2.39 \times 10^{-9}$	0	$8.42 \times 10^{-11}$	10	10	15
S190923y <sup>†</sup>	13.8	13.7	723.7	39.4	59.7	$1.91 \times 10^{-2}$	8.95	0	$2.29 \times 10^{-2}$	46	95	120
S190924h	2.97	2.90	281.3	70.2	73.1	$4.52 \times 10^{-5}$	26.4	$5.05 \times 10^{-8}$	$3.59 \times 10^{-4}$	61	75	101
S190930s	6.28	6.20	2139.9	92.2	92.2	$2.20 \times 10^{-3}$	14.2	$1.06 \times 10^{-6}$	$4.48 \times 10^{-3}$	13	89	142
S190930t <sup>†</sup>	12.8	12.7	918.2	6.84	9.91	1.24	6.55	$1.06 \times 10^{-3}$	2.01	48	109	130
Mean	9.90	8.79	732.3	45.3	64.4	0.30	9.91	$6.87 \times 10^{-4}$	0.48	48	79	126
Median	6.58	6.20	543.9	41.2	73.1	$8.52 \times 10^{-5}$	1.03	0	$3.59 \times 10^{-4}$	48	70	136

**Table 2.** GOTO-4 coverage of the LVC probability maps.  $\delta t_{\text{trig}}$  is the time between the GW trigger and the first GOTO-4 observation.  $\delta t_{\text{alert}}$  is the time between receiving the LVC preliminary notification and the first GOTO-4 observation. pA is the percentage of the total probability that was tiled by GOTO-4. pA<sub>vis</sub> represents the percentage of the total probability that was visible to GOTO-4 from its site in La Palma, accounting for Sun constraints and altitude limits. The 3D Coverage columns indicate the volumetric coverage for each of the test sources defined in Section 3. The KN Range columns indicate the horizon out to which 90, 50 and zero per cent of the 2D probability coverage is retained in a search for an AT2017gfo-like event.<sup>†</sup> denotes that a BAYESTAR map was used; no LALInference map was available.

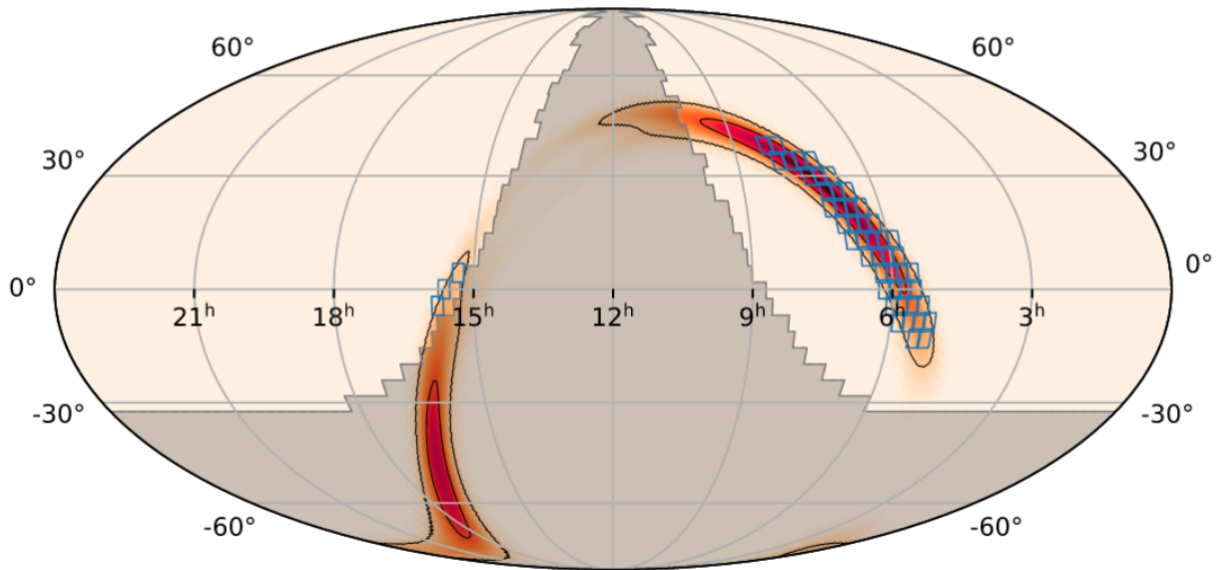


**Figure 4.** GOTO-4 follow-up of S190923y (25814). Each blue box represents one GOTO-4 tile, with the observing strategy prioritising the highest probability tiles first (darker shaded regions are higher probability). The Area Covered and  $pA$  values in Table 2 comprise the sum of the physical area and probability contained within these tiles respectively, after accounting for overlap. The shaded area indicates unobservable regions, either from altitude limits or Sun constraints.  $pA_{\text{vis}}$  (Table 2) indicates the total fraction of probability that is observable (i.e. that lies within the non-grey region). Axes are in RA/Dec.

- 下表展示了在不同的样本区间内，各种类型的源的探测期望个数。对于偏轴GRB，千新星以及19mag源来说，加上距离限制和不加距离限制的期望探测是一样的，说明250Mpc (nearby) 以上的这三种类型的源基本上不会被观测到。相反，正轴GRB由于其亮度，可以在更远的距离被探测到。250Mpc以内的事件是GOTO的主要关注对象。可以看出，可能需要在数十个250Mpc以内的GW才能发现一个KN。

	Events	GRB	Off-axis GRB	KN	19 <sup>th</sup> mag
Whole map	29	2.87	$10^{-4}$	0.09	0.14
Obs	29	7.04	$3 \times 10^{-4}$	0.49	0.90
Nearby	5	0.86	$10^{-4}$	0.09	0.14
Nearby, obs	5	4.15	$3 \times 10^{-4}$	0.49	0.90
BBH	17	0.34	$10^{-8}$	$10^{-4}$	$2 \times 10^{-4}$
BNS	5	0.89	$10^{-4}$	0.07	0.12
All non-BBH	12	2.53	$10^{-4}$	0.09	0.14

**Table 3.** The number of detections of each type of signal we would expect to have seen in our sample and highlighted subsamples if all LVC superevents contained our test sources. “Whole map” assumes that the test source could be anywhere in the map, whether the region was observed or not. “Obs” assumes that the test source occurred within the region covered by GOTO-4. “Nearby” refers to events that occurred within 250 Mpc. “BBH”, “BNS” and “All non-BBH” are given for the “Whole map” scenario, but are limited to events where the given classification was assigned the highest probability by the LVC, excluding terrestrial.

- 注意到，表2最后3列，作者计算了如果对应体是AT2017gfo型事件，深度分别足够保留90%，50%和0%（损失的部分因为深度不够）的2D可观测概率天区覆盖率对应的距离。可以看出，对GW170817这样的事件，GOTO-4期望可以探测到AT2017gfo（平均 $D_{90} = 48\text{Mpc}$ ，即在90%的视线方向上由足够的深度覆盖48Mpc的AT2017gfo）。这种保留率和距离的关系也可见下图。GOTO-4可以在100Mpc以上搜寻AT2017gfo类型的事情。200Mpc也有一定的可能性（and is capable of achieving 200 Mpc in a favourable line of sight.）

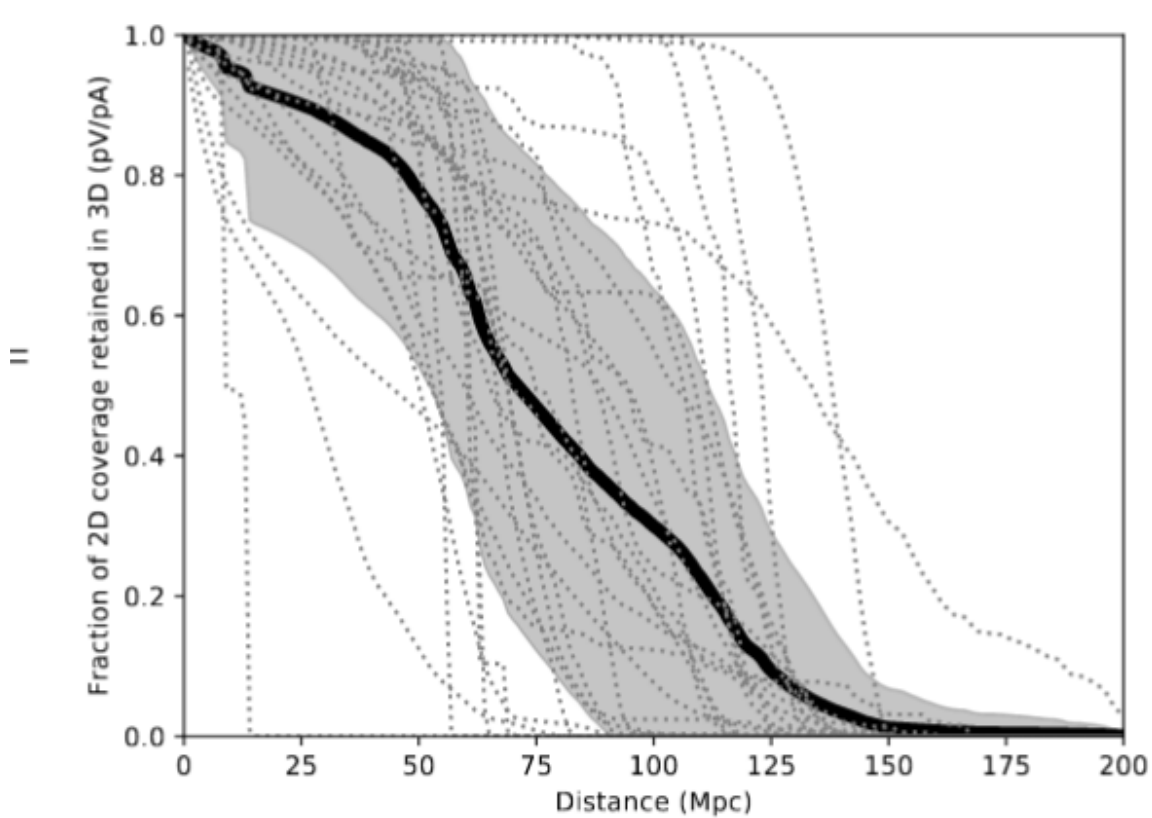


**Figure 5.** The fraction of the 2D probability coverage that is retained with increasing distance. Each dotted line represents an LVC follow-up campaign with GOTO-4. The thick black line is the mean of the 29 events, and the grey area is the  $1\sigma$  standard deviation.

- 下图显示了LVC分类为BNS事件的事件距离分布（包括 $1/\sigma_{dist}^2$ 加权的分布和没加权且包括GW170817的分布）以及GOTO-4可观测的事件距离分布。由此估计GOTO-4的深度可以覆盖到加权分布中18%的事件或不加权且包括GW170817分布中22.5%的事件。

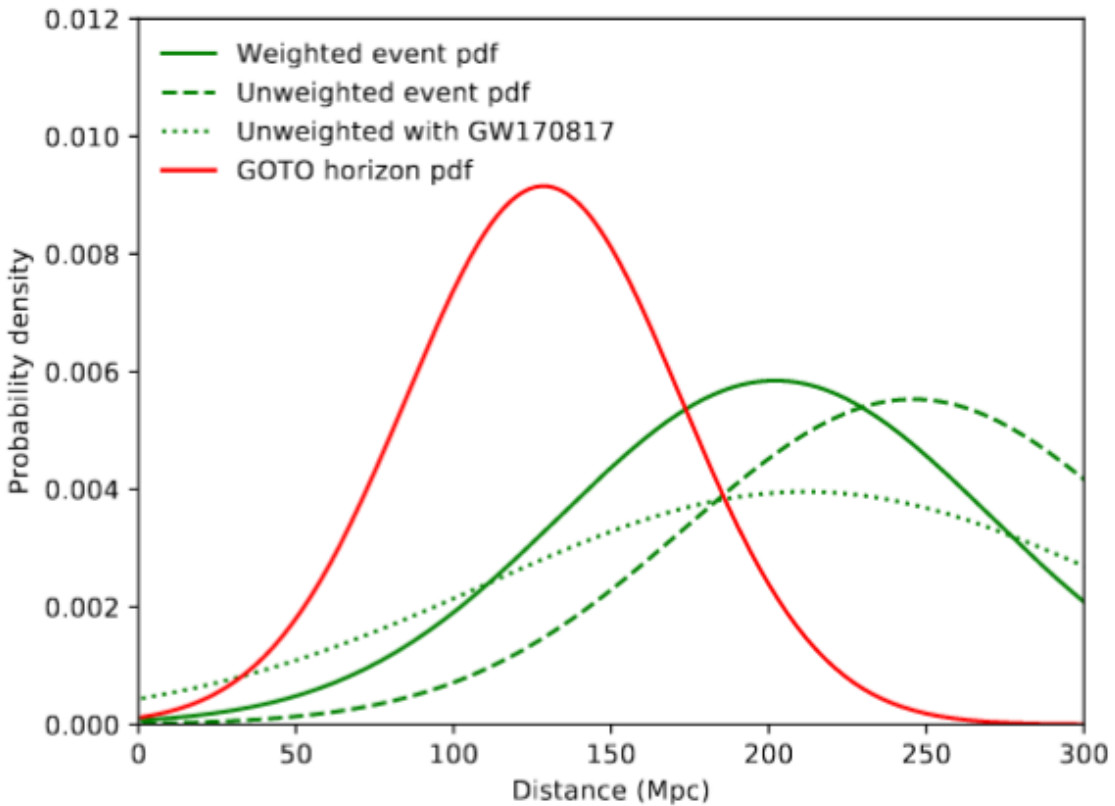


**Figure 6.** The probability density function (PDF) of the horizons achieved for a Bazin model during the 29 GOTO-4 LVC follow-up campaigns (red). These are compared to the weighted PDF (weights =  $1/\sigma_{\text{dist}}^2$ ) of the 5 BNS merger events during this time (green, solid), their unweighted PDF (dashed), and the unweighted PDF when the distance to GW170817 (41 Mpc; Hjorth et al. 2017) is included (dotted). The weighted PDF including GW170817 is not shown because the distance errors for this event are far smaller than the other 5 due to its EM detection.

- 表2中有少数源的KN最大观测深度非常小，如S190915ak, S190510g和S190421ar。
  - S190915ak的KN最大观测深度只有15Mpc，主要原因是大气质量高（2），亮月影响大（91.5% illumination），以及观测时间几乎是在峰值后一天，此时光度已经相对最大值下降了接近一个星等。
  - S190510g的KN最大观测深度为57Mpc，大气质量为1.78。尽管月光影响不大（30%），但最大的问题是观测时间太早，所有的观测都在0.1天内进行，而此时亮度还没有达到最大，比最大值低了近2个星等。
  - S190421ar的KN最大深度为66Mpc，大气质量为1.88，月亮也比较亮（77%），并且观测时风速较大（平均21 km/s）。除此之外，此事件的观测方向上又相对其它事件较大的消光，中值大约 $A_V \approx 0.2 \text{mag}$ 。而且观测时间也比较晚，在

trigger后两天，此时星等也比峰值要小2个星等。

- 也有少数源的KN最大观测深度比较高，如S190425z和S190706ai。
  - S190425z的KN最大深度达到了227Mpc，大气质量为1.27，月亮为51%。观测条件比前面三个要好，但最主要原因是观测正好是在模型中的峰值时段进行。
  - S190706ai的KN最大深度为168Mpc，大气质量为1.79，月亮为34%，观测条件接近上面的S190510g，主要区别还是S190706ai的观测时间更接近峰值。
- 可以看出尽管观测条件（天气，风，大气质量，月亮亮度和telescope optics）会影响观测深度（极限星等），但影响到我们能在多远距离上探测到KN的主要因素是观测时间。根据模型，在trigger后的0.5天是有必要进行观测的。

- 展望

- 引力波探测器的精度提升和灵敏度提升。
  - O4将加入Kamioka Gravitational-wave Detector (KAGRA, 神冈引力波探测器，在日本岐阜县)，估计那时的BNS(BBH)定位精度将从O3的中值 $270^{+34}_{-30}$ ( $280^{+30}_{-23}$ )平方度的90%置信区间到O4的对应定位精度中值为 $33^{+5}_{-5}$ ( $41^{+7}_{-6}$ )平方度。
  - 关于所需的灵敏度，O4期间预期的BNS范围为160 – 190 Mpc (aLIGO)，90 – 120 Mpc (AdV) 和25 – 130 Mpc (KAGRA)。
- 增加深度（极限星等）：增加曝光时间，叠加更多图像。这两点都可以得益于引力波探测器定位精度的提高。如果极限星等能够达到22等，则可以覆盖O4几乎所有的BNS事件。

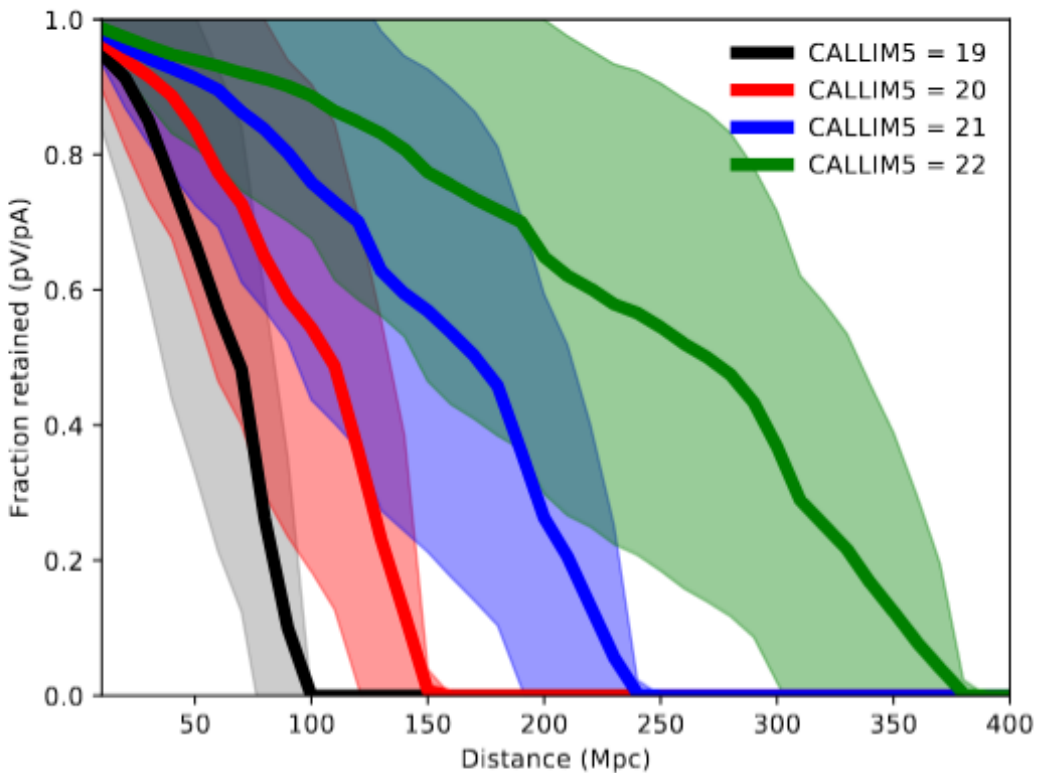


**Figure 7.** The mean fraction of 2D probability coverage that is retained with distance for our sample using an assumed  $m_{\text{lim}}$  for all tiles. "CALLIM5" is the GOTO fits header keyword for  $m_{\text{lim}}$ . In addition to greater depth overall, we expect more visits to produce a more "box-like" plot, with flatter sections out to greater distances, followed by faster drop offs. This is because more repeats along a given line of sight will provide deeper alternatives to poor observing epochs with shallow horizons, which create the sloping curvature seen here.

- 在加入在澳大利亚的南半球观测点后，可以增加观测时间窗口，反应速度和观测天区范围。